

**SYNTHESIS, COMPUTATIONS AND CHARACTERIZATIONS OF LOW
DIMENSIONAL RARE-EARTH COMPOUNDS**

A Dissertation

by

CHUN-YU CHEN

Submitted to the Office of Graduate and Professional Studies of
Texas A&M University
in partial fulfillment of the requirements for the degree of

DOCTOR OF PHILOSOPHY

Chair of Committee,	Timothy R. Hughbanks
Committee Members,	Marcetta Y. Darensbourg
	François P. Gabbaï
	Winfried Teizer
Head of Department,	David H. Russell

May 2014

Major Subject: Chemistry

Copyright 2014 Chun-Yu Chen

ABSTRACT

Reduced rare-earth (Ln, lanthanide elements) compounds with low-dimensional Ln-Ln-bonded structures are promising candidates for magnetic materials because Ln-Ln-bonded molecules and solids have delocalized $5d$ electrons that make strong magnetic coupling possible. Four new rare-earth compounds were synthesized in this work, I. $\text{Gd}_9\text{Br}_{16}\text{O}_4$, II. $\text{Gd}_6\text{Br}_7\text{Si}_2$, III. Pr_3Si and IV. $\text{Pr}_2\text{I}_2\text{Ge}$. The first two gadolinium bromide compounds exhibit 1-dimensional Ln-Ln-bonded motifs imbedded within layered structures. Pr_3Si is a new binary phase with a structure that can be more easily visualized by focusing on the interpenetrating (10, 3)-a silicon network. $\text{Pr}_2\text{I}_2\text{Ge}$ has a double-layered structure. The results of EHTB band structure calculations indicate that the bottom the $\text{Gd}_9\text{Br}_{16}\text{O}_4$ d bands and those of a hypothetical analogous yttrium compound ($\text{Y}_9\text{Br}_{16}\text{O}_4$) are half filled; the Fermi levels of those two compounds cut through two d bands. $\text{Gd}_6\text{Br}_7\text{Si}_2$ and Pr_3Si are predicted to be metallic, as expected. The results of magnetic measurements on $\text{Gd}_6\text{Br}_7\text{Si}_2$ show that it behaves like a soft magnet at 2 K and undergoes phase transitions at 27 K and 70 K.

DEDICATION

This dissertation is dedicated to my older brother, Ken-Li Chen who inspired me to be a scientist. He has been an excellent mentor throughout my life.

ACKNOWLEDGEMENTS

I am very grateful to my advisor, Dr. Timothy Hughbanks for his patience, scientific guidance and encouragement throughout my graduate career. It is difficult to study at graduate school with the duty of taking care of a child alone. I truly appreciate his understanding and trust in my time management. I would like to thank my committee members, Dr. Marcetta Y. Darensbourg, Dr. Gabbai and Dr. Teizer, for their time to this project. I also thank the members of Hughbanks' group, including Luke Sweet, Scott Dempsey, Jose Delgado, Francisco Escobedo, and especially Robby Davis who helped me a lot in the laboratory when I joined the group. I want to thank Dr. Joe Reibenspies and especially Dr. Nattami Bhuvanesh for the valuable discussion and the time on teaching me how to deal with the data of twined crystals. I am appreciative to Dr. Kim Dunbar and Dr. Andrey Prosvirin for helping me with SQUID measurements. I also want to thank Dr. Renald Guillemette for the EDX measurements. Moreover, the DFT calculation would not be complete without the technical assistant of Dr. Lisa Pérez. Specially thanks to my friends, especially the Taiwanese students from chemistry department for making my time at Texas A&M University more memorable. Thanks to my parents, my brothers, Myong and Sandy Manning for their encouragement.

Finally, I want to express my utmost gratitude to my husband, Hung-Yi Liao, for driving 400 miles every weekend in order to see our baby. I could not finish this work without his financial support and patience.

NOMENCLATURE

BLYP	Becke-Lee-Yang-Parr function
BSE	Backscattered Electrons
BZ	Brillouin Zone
CCD	Charge-couple Device
CELL_NOW	A program for analyzing orientation matrix of twin domains.
COOP	Crystal Orbital Overlap Population
DFT	Density Functional Theory
DMol ³	The models can be applied to calculate solid state structures.
DND	Double Numerical Plus <i>d</i> -functions
DOS	Density of States
ECF	Effective Core Potential
EDS	Energy Dispersive Spectrometry
E_F	Fermi Level
EHT	Extended Hückel Theory
EHTB	Extended Hückel-Tight Binding
Gd	Gadolinium
LDA	Local Density Approximation
Ln	Lanthanides
LSDA	Local Spin Density Approximation
MATLAB	A language for computing and programming.

MCE	Magnetocaloric Effect
MS	Material Studio
MPMS	Magnetic Property Measurement System
PDOS	Partial Density of States
Pr	Praseodymium
PXRD	Powder X-ray Diffraction
RKKY	Ruderman-Kittel-Kasuya-Yosida
RM	Remanent Magnetization
SADABS	Bruker AXS detector scaling and absorption correction program
SCF	Self-Consistent Field
SE	Secondary Electrons
SHELXTL	Bruker AXS program for refining crystal structures
SQUID	Superconducting Quantum Interference Device
STO	Slater-type Orbital
TOPAS	A new generation of profile and structure analysis software
TWINABS	Bruker AXS scaling program for twinned crystals
WDS	Wavelength-dispersive Spectrometry
YAeHMOP	Yet Another Extended Hückel Molecular Orbital Program

TABLE OF CONTENTS

	Page
ABSTRACT	ii
DEDICATION	iii
ACKNOWLEDGEMENTS	iv
NOMENCLATURE	v
TABLE OF CONTENTS	vii
LIST OF FIGURES	ix
LIST OF TABLES	xii
1. INTRODUCTION.....	1
1.1 The Characteristics of Lanthanide Elements	2
1.2 The Structures of Low-Dimensional Lanthanide-Halide Compounds	4
1.3 The Magnetic Application of Low-Dimensional Rare-Earth Compounds	5
2. EXPERIMENTAL AND THEORETICAL METHODS.....	8
2.1 Experimental Methods	8
2.1.1 Solid State Synthesis	8
2.1.2 Single-Crystal and Powder X-ray Diffractometer	9
2.1.3 Quantum Design MPMS-XL SQUID Magnetometer	10
2.1.4 Energy-Dispersive and Wavelength-Dispersive Spectrometry Systems....	11
2.2 Theoretical Method	12
2.2.1 Extended Hückel/Tight Binding Method	12
2.2.2 Density Functional Method.....	14
3. GADOLINIUM LAYER COMPOUNDS	17
3.1 Synthesis.....	17
3.2 Single-Crystal X-ray Diffraction.....	18
3.3 Powder X-ray Diffraction.....	22
3.4 Microprobe Analyses	22
3.5 Magnetic Measurements	25

	Page
3.6 Crystal Structures	31
3.6.1 Gd ₉ Br ₁₆ O ₄ : A 3-D Structure with a Reduced Metal Layer.	31
3.6.2 Gd ₆ Br ₇ Si ₂ : Two Types of Interstitial Atoms with a Layer Structure	34
3.7 Calculated Electronic Structure.....	38
3.7.1 The Electronic Structure of Gd ₉ Br ₁₆ O ₄	38
3.7.2 The Electronic Structure of Gd ₆ Br ₇ Si ₂	50
3.8 Result and Discussion	53
3.8.1 Compound I: Gd ₉ Br ₁₆ O ₄	53
3.8.2 Compound II: Gd ₆ Br ₇ Si ₂	54
 4. PRASEODYMIUM LAYER COMPOUNDS	 55
4.1 Synthesis.....	55
4.2 Single-Crystal X-ray Diffraction.....	56
4.3 Powder X-ray Diffraction.....	60
4.3.1. The X-ray Powder Pattern of Pr ₃ Si	60
4.3.2 The X-ray Powder Pattern of Pr ₂ I ₂ Ge	62
4.4 Crystal Structures	64
4.4.1 The Structure of Pr ₃ Si.....	64
4.4.2 The Structure of Pr ₂ I ₂ Ge.....	69
4.5 Calculated Electronic Structure.....	72
4.5 Result and Discussion	80
4.5.1 Compound III: Pr ₃ Si.....	80
4.5.2 Compound IV: Pr ₂ I ₂ Ge.....	82
 5. CONCLUSIONS	 83
 REFERENCES	 89
 APPENDIX	 96

LIST OF FIGURES

	Page
Figure 1.1. Orbital radial distribution in gadolinium metal.	3
Figure 1.2. Electronic splitting of the Gd atom as a function of $4f$ - $5d$ exchange perturbation.	4
Figure 1.3. Different types of connections via <i>cis</i> - and <i>trans</i> - positioned of octahedral edges.....	5
Figure 1.4. Different structure types in RE_5Tt_4 . Black circles are Tt. Blue circles are RE.	6
Figure 3.1. The result of characterizing $Gd_6Br_7Si_2$ phase from TOPAS	21
Figure 3.2. Energy-dispersive spectrometry of $Gd_6Br_7Si_2$	24
Figure 3.3. Energy-dispersive spectrometry of $Gd_9Br_{16}O_4$	24
Figure 3.4(a). Left and (b) Right are the SE image and BSE images of $Gd_9Br_{16}O_4$	25
Figure 3.5(a). (Left Axis): The plot of χT vs T for $Gd_6Br_7Si_2$ at an applied field (0.1T) is labeled by blue dotted-line.....	26
Figure 3.5(b). The result of magnetic hysteresis measurement for $Gd_6Br_7Si_2$	29
Figure 3.5(c). A plot shows the result of zero field cooling and field cooling measurements.....	30
Figure 3.6. The 2-D metal layer of $Gd_9Br_{16}O_4$	31
Figure 3.7. The structure of $Gd_9Br_{16}O_4$	32
Figure 3.8. A single chain structure within the layer of $Gd_9Br_{16}O_4$	33
Figure 3.9(a). The structure of $Gd_6Br_7Si_2$ is a layer. Green dashed line is drawn to show a unit.	34
Figure 3.9(b). There are two types of interstitial chains in every layer	35
Figure 3.10. Each chain is connected via sharing the edge of Gd_6 octahedra.....	36

	Page
Figure 3.11(a). The partial density of states (PDOS) of $Y_9Br_{16}O_4$ from EHTB calculation.....	40
Figure 3.11(b). EHTB calculation. The band structure of $Y_9Br_{16}O_4$ from -2 to -8 eV is displayed.	42
Figure 3.11(c). The band structure from -2eV to -8eV and the DOS of $Y_9Br_{16}O_4$ are presented.	44
Figure 3.12. The EHTB band calculations of $Gd_9Br_{16}O_4$ with spins that are aligned antiparallel with the local spin direction of the 4f electrons.	45
Figure 3.13. The EHTB band calculations of $Gd_9Br_{16}O_4$ with spins that are aligned parallel with the local spin direction of the 4f electrons.	45
Figure 3.14. The band structure and density of state (DOS) of $Y_9Br_{16}O_4$ from DFT calculation are shown.....	46
Figure 3.15(a). The calculated dispersion curves for the bands along Γ -Y of the BZ are shown.	48
Figure 3.15(b). The calculated dispersion curves for the bands along X-A ₁ of the BZ are shown.	48
Figure 3.15(c). The calculated dispersion curves for the bands along Y-T of the BZ are shown.	49
Figure 3.16. (Left) The plot of partial density of state of $Gd_6Br_7Si_2$	51
Figure 3.17. (Left) The band structure of $Y_6Br_7Si_2$	52
Figure 4.1(a). The result of characterizing Pr_3Si phase from TOPAS program.....	61
Figure 4.1(b). The result of characterizing Pr_2I_2Ge phase from TOPAS program.	63
Figure 4.2. View a 3-D structure of Pr_3Si along [111].....	64
Figure 4.3(a). Tilt the structure to view the stacking of polyhedra and the helix chains of red silicon networks.	65
Figure 4.3(b). A single octahedron shows the connections between the interstitial silicon atom and Pr atoms.....	66
Figure 4.4(a) Two symmetry relative (10, 3)-a nets are labelled red and green.	67

	Page
Figure 4.4(b). Select the unit cell to see the direction of two helices	67
Figure 4.4(c). Zoom in the rectangular box to recognize.....	67
Figure 4.4(d). (10, 3)-a nets are shown in a [010] projection.....	68
Figure 4.5. The closed packed layers are separated by iodine atoms. Black dash line is presented a unit cell.	69
Figure 4.6. The layer of $\text{Pr}_2\text{I}_2\text{Ge}$ without showing iodine atoms.	70
Figure 4.7. The layer of $\text{Pr}_2\text{I}_2\text{Ge}$ is shown. Each tetrahedral site is filled by an iodine atom.	71
Figure 4.8. The building block of $\text{Pr}_2\text{I}_2\text{Ge}$ is shown.	72
Figure 4.9(a). DOS of Pr_3Si	73
Figure 4.9(b). The band structure of Pr_3Si	74
Figure 4.9(c). The band structure with the plot of DOS of Pr_3Si at the same energy range are presented.....	75
Figure 4.10. A mesh of 285 k-points throughout the first Brillouin zone.....	76
Figure 4.11. COOP (Crystal Orbital Overlap Population) of Pr_3Si	79

LIST OF TABLES

	Page
Table 3.1. Selected bond lengths [\AA] for $\text{Gd}_6\text{Br}_7\text{Si}_2$	19
Table 3.2(a). Atomic coordinates and equivalent isotropic displacement parameters ($\text{\AA}^2 \times 10^3$) for $\text{Gd}_6\text{Br}_7\text{Si}_2$	20
Table 3.2(b). Atomic coordinates and equivalent isotropic displacement parameters ($\text{\AA}^2 \times 10^3$) for $\text{Gd}_9\text{Br}_{16}\text{O}_4$	20
Table 3.3. Crystal data and structure refinements for $\text{Gd}_9\text{Br}_{16}\text{O}_4$ (I) and $\text{Gd}_6\text{Br}_7\text{Si}_2$ (II)	21
Table 3.4. Extended Hückel Exponents(ξ), valence shell ionization potential (H_{ii} in eV) and coefficients are listed.	39
Table 4.1. Selected bond lengths [\AA] for Pr_3Si and $\text{Pr}_2\text{I}_2\text{Ge}$	57
Table 4.2(a). Atomic coordinates and equivalent isotropic displacement parameters ($\text{\AA}^2 \times 10^3$) for Pr_3Si	58
Table 4.2(b). Atomic coordinates and equivalent isotropic displacement parameters ($\text{\AA}^2 \times 10^3$) for $\text{Pr}_2\text{I}_2\text{Ge}$	58
Table 4.3. Crystal data and structure refinement for Pr_3Si (III) and $\text{Pr}_2\text{I}_2\text{Ge}$ (IV).....	59
Table 4.4. The weighting values of each K point in the first Brillouin zone of body center cubic.....	77
Table 4.5. Extended Hückel Exponents(ξ), valence shell ionization potential (H_{ii} in eV) and coefficients are listed.	77
Table 4.6. Crystal structures and lattice parameters of intermediate phases in Pr-Si system.	80
Table 5.1. The comparisons of four crystal structures in this work.	85
Table 5.2. The comparisons of bond lengths in different interstitial polyhedra.	87

1. INTRODUCTION

Our interest in lanthanide chemistry arises from the magnetic properties, coordination chemistry, luminescence of lanthanide compounds and the variety of reduce phase from the rare-earth metal halides. Outstanding examples of lanthanide magnetic material are Nd-Fe-B alloys that are notable permanent magnets¹ and $\text{Gd}_5\text{Ge}_2\text{Si}_2$ ^{2, 3} that exhibits a giant magnetocaloric effect³(MCE effect) at 276 K that make it a prototypical candidate for application to magnetic refrigeration². Earlier research in the Gd/Si/Ge system^{2, 4-6} motivated our study of low dimensional structures constructed by rare-earth metal halides and Ge/Si or other main group components. Magnetic property of $\text{REXGe}(\text{Si})$ (RE= rare earth metal. X= halogen) compounds has not been reported until now. Seeking the development of the crystallography, magnetic property, and electronic structure in the $\text{REXGe}(\text{Si})$ system will be promising.

This work mainly focuses on the synthesis, characterizations and computations of low-dimensional rare-earth metal-halide compounds with Si/Ge/O elements as an interstitial atom. Four new compounds, I. $\text{Gd}_9\text{Br}_{16}\text{O}_4$, II. $\text{Gd}_6\text{Br}_7\text{Si}_2$, III. Pr_3Si , and IV. $\text{Pr}_2\text{I}_2\text{Ge}$ were synthesized and discussed herein. Computational results applied to $\text{Gd}_9\text{Br}_{16}\text{O}_4$ reveal the property of semilocalized bonding in the extended Gd-Gd bonded systems. The results of EHTB band structure calculations indicate that the bottom the $\text{Gd}_9\text{Br}_{16}\text{O}_4$ *d* bands and those of a hypothetical analogous yttrium compound ($\text{Y}_9\text{Br}_{16}\text{O}_4$) are half filled; the Fermi levels of those two compounds cut through two *d* bands. $\text{Gd}_6\text{Br}_7\text{Si}_2$ and Pr_3Si are predicted to be metallic, as expected. The magnetic data of

Gd₆Br₇Si₂ show interesting phase transitions at 27 K and 70 K. The structure of Pr₃Si displays an interpenetrating (10, 3)-a silicon network. Pr₂I₂Ge has closed-packed doubled layers structure. This section will present an overview on the characteristics, structures and magnetic applications in the field of low dimensional rare-earth compounds.

1.1 The Characteristics of Lanthanide Elements

Rare earth metals have a greater extent than the *d* orbitals on transition metal atoms. The *4f* orbitals on lanthanide atoms are highly contracted, so the direct participation in magnetic exchange coupling which is mediated by the *4f*-overlap with ligand orbitals is precluded. (Figure 1.1) Instead, an indirect pathway related the localized *4f* electrons and the *5d* conduction electrons will cause the magnetic ordering.⁷
⁸ For instance, elemental gadolinium exhibits ferromagnetic ordering near the room temperature (293 K). The origin of strong exchange coupling that underlies ferromagnetism in gadolinium is the *5d* conduction electrons which mediate the *4f*-*4f* coupling via an indirect mechanism. When the conducted electrons are spin polarized will enhance the exchange coupling.⁹

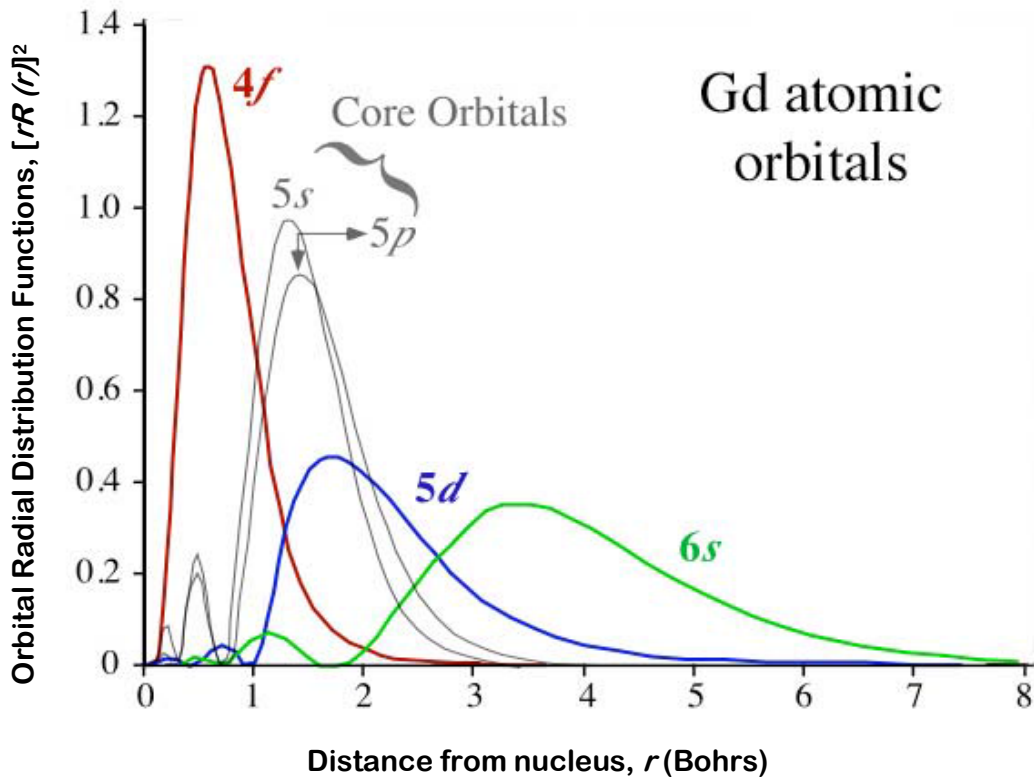


Figure 1.1. Orbital radial distribution in gadolinium metal.

About this process, how the potential from $4f^7$ influences the electrons which locate at $5d$ and $6s$ orbitals is illustrated in Figure 1.2.⁹ The left side is an “unperturbed” system where the valence d electron experiences an average exchange potential from the half-filled $4f$ shell, so the d electron has no preferred spin orientations. After applying the exchange field, the spin aligned with (against) the $4f$ spins is stabilized (destabilized) by an energy δ . For a Gd atom, 2δ is the difference between the ground state ($9D$) and the first excited state ($7D$). These intraatomic exchange interactions are intrinsically “ferromagnetic”, favoring parallel alignment of the $4f$ and $5d$ spins.

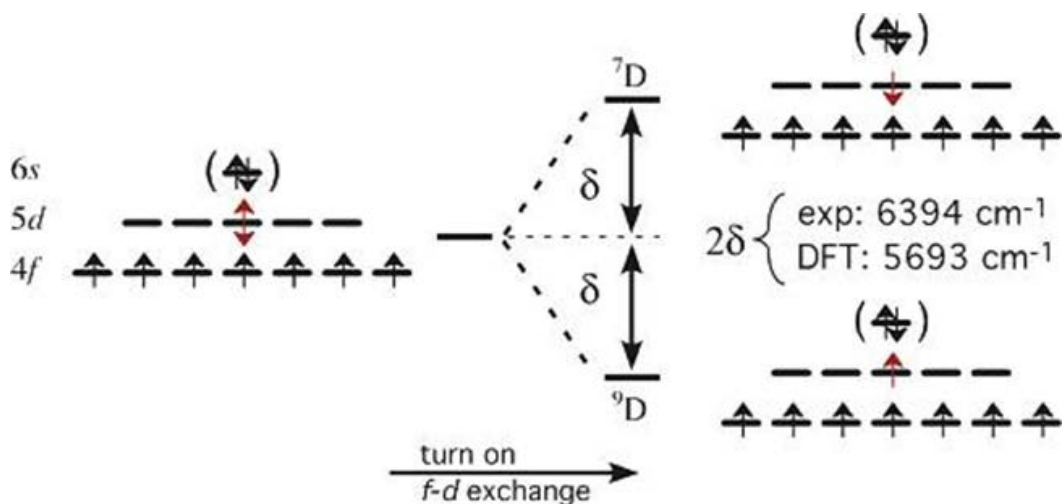


Figure 1.2. Electronic splitting of the Gd atom as a function of $4f$ - $5d$ exchange perturbation.

1.2 The Structures of Low-Dimensional Lanthanide-Halide Compounds

Rare-earth metal halides can form extensive variety of Ln-Ln bonded reduced phases (Ln: Lanthanide metals).¹⁰ Many of them, the structures are derived from Ln_6 octahedra as building units and contain interstitial species Z in the center of octahedra. The structures can be a cluster or condensed to be chains, layers and three-dimensional frameworks¹¹. Based on the sequence of connection via *cis*- and *trans*- positioned of the octahedral edges, three distinct configurations of 1-D chains are listed in Figure 1.3. The structures of ternary phases Ln_4ZX_5 ¹²⁻¹⁶ ($Z = \text{C}, \text{C}_2, \text{B}, \text{B}_4, \text{X} = \text{halides}$), Ln_4ZX_6 ^{17, 18} ($Z = \text{Si}$) and $\text{Ln}_6\text{X}_7\text{Z}$ ¹⁹ ($Z = \text{C}_2$) are classified by a t-t-t sequence. (Figure 1.3.a) Interestingly, Ln_4ZX_6 ($Z = \text{B}$)²⁰ with different interstitial entries will construct a configuration of t-c-t sequence (Figure 1.3.b) and $\text{Ln}_{12}\text{Z}_3\text{I}_{17}$ ²¹ ($Z = \text{C}_2$) can form t-c-c chains. (Figure 1.3.c)

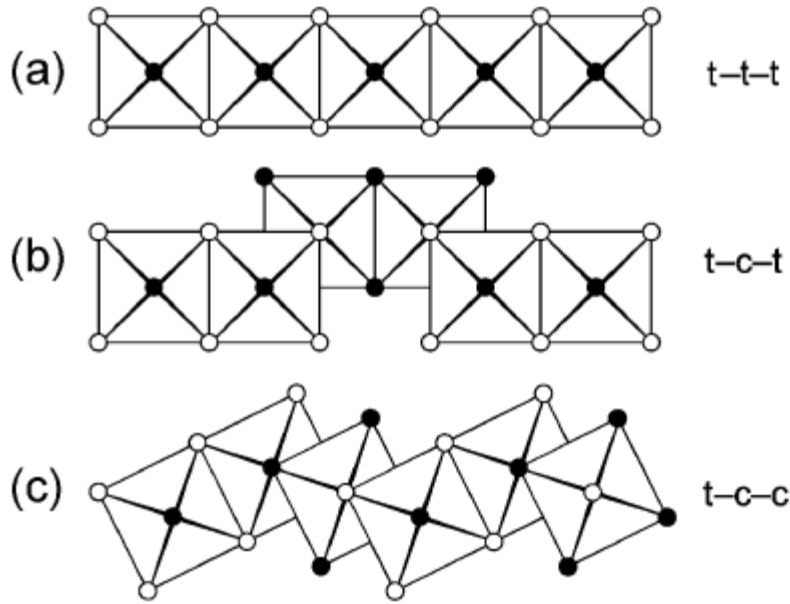


Figure 1.3. Different types of connections via *cis*- and *trans*- positioned of octahedral edges

1.3 The Magnetic Application of Low-Dimensional Rare-Earth Compounds

In 1997, Pecharsky and Gschneidner discovered that $\text{Gd}_5\text{Ge}_2\text{Si}_2$ ³ exhibits a giant magnetocaloric effect (MCE)^{5, 22} at 276 K and the effect of $\text{Gd}_5\text{Ge}_2\text{Si}_2$ almost doubled than previously observed gadolinium element at 294 K^{5, 23}. The magnetocaloric properties of this compounds makes it a prototypical material candidate for magnetic refrigeration. The magnetocaloric effect is a temperature change caused by the material under an applied magnetic field and adiabatic cooling process. The famous system which has giant MCE is the $\text{Gd}_5(\text{Si}_x\text{Ge}_{1-x})_4$ system^{3, 5} ($0 \leq x \leq 1$). In the RE_5Tt_4 (RE= rare earth

metal, Tt = Ge,Si) system, the physics of $Gd_5(Si_xGe_{1-x})_4$, was considered due to the unique 2-D crystal structure.

There are three different structure types that play a part in RE_5Tt_4 giant MCE materials, which are depicted in Figure 1.4: (i) Gd_5Si_4 -type, the layers are connected by the Tt-Tt single bonds, $d(Tt-Tt)= 2.6 \text{ \AA}$. (ii) $Gd_5Ge_2Si_2$ -type, the Tt-Tt interatomic distances between layers alternate between bonding and nonbonding. (iii) Sm_5Ge_4 -type, the Tt-Tt interatomic distances between layers are all longer than 3.5 \AA (non-bonding).

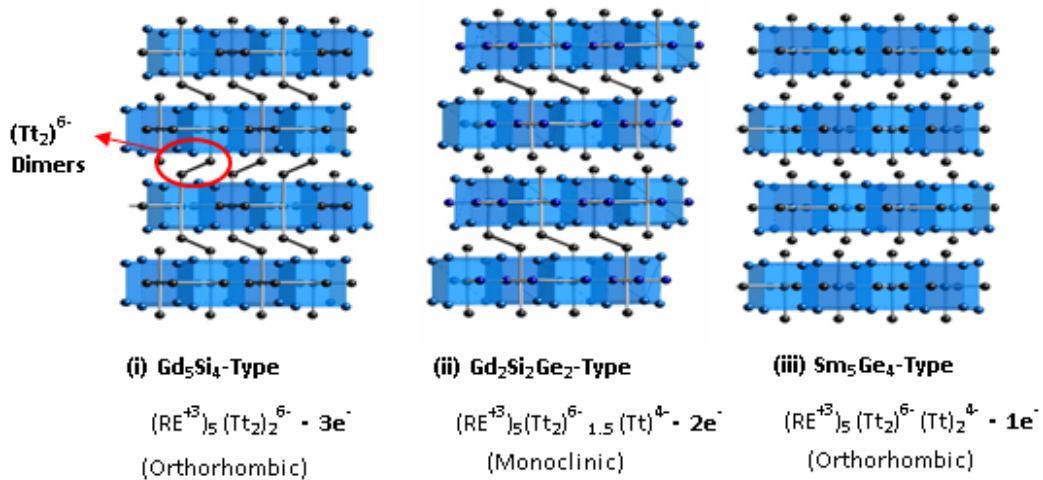


Figure 1.4. Different structure types in RE_5Tt_4 . Black circles are Tt. Blue circles are RE.

The interplay between crystal structure, electronic structure and physical behavior is illuminated by counting electrons. If we assume that the rare-earth metal is formally trivalent (RE^{+3}), single bonded Tt-Tt dimers, $(Tt_2)^{6-}$, are 14 valence electron-units (Octet rule); nonbonded Tt...Tt dimers are similar as two 8 valence electrons Tt^4 -units and two electrons would fill into the anti-bonding to break the Tt-Tt bonds.

Therefore, according to their structures, the formulas for three structure types will be: (i) $(RE^{+3})_5 (Tt_2)^{6-}_2 \cdot 3e^-$ (ii) $(RE^{+3})_5 (Tt_2)^{6-}_{1.5} (Tt)^{4-} \cdot 2e^-$ (iii) $(RE^{+3})_5 (Tt_2)^{6-} (Tt)^{4-}_2 \cdot 1e^-$ (RE= rare earth metal. Tt= Ge, Si. In the structure of Sm_5Ge_4 type, there are 50% of Tt atoms are nonbonded; 50% are single bonded dimers). The formulas above show that an internal reduction-oxidation process occurs in the solid state as the structural phase transition occurs.

This example demonstrates how structural phase transitions can have an important effect on the electronic structure and physical behavior. Because structure phase transitions are relative to forming bonds or breaking bonds, and change electron concentration in the structures, they also influence the magnetic properties. In the Re_5Tt_4 (Re= rare earth metal, Tt= Ge,Si) system, The 2-D structure is built by the Gd-Si/Ge-Si/Ge-Gd networks and covalent like Si-Si, Ge-Si or Ge-Ge bonds which are believed to be the reason why the interlayer coupling can be enhanced²³. Changing in the composition of Si and Ge makes this system to present fantastic variation in crystal lattices and magnetic properties. Besides, paramagnetic rare earth compounds usually have large effective magnetic moment at lower temperature, so they may be ideal magnetic materials. For example, Gd^{+3} salt, $-\Delta Sm = 78.8 \text{ Jmol}^{-1}K^{-1}$ at 5 K under a field that ranges from 0 to 5T. (Comparing to $Gd_2Si_2Ge_2$, $-\Delta Sm = 15.8 \text{ Jmol}^{-1}K^{-1}$ at 276 K, H= 2 T).² Those explanations above illuminate why $Gd_5(Si_xGe_{1-x})_4$ is an interesting system.

2. EXPERIMENTAL AND THEORETICAL METHODS

In this section I will briefly describe the experimental methods that were used to synthesize new products and discuss methods used to characterize the physical properties of the products. Also, theoretical methods will be discussed in this section to explain the computational methods models which I chose for calculating the electronic structures, and to thereby study bonding in certain compounds.

2.1 Experimental Method

2.1.1 *Solid State Synthesis*

There are several different solid state synthetic methods²⁴, (i) conventional ceramic method, (ii) hydrothermal synthesis, (iii) molten salt fluxes synthesizes, and (iv) chemical vapor route synthesis. Molten salt fluxes synthesis is to dissolve reactants in a solvent. Chemical transport-route synthesis is to use gas as a transport to carry out the reactant into the gas phase. For most of the compounds reported here, the conventional ceramic method was used for their synthesis. Some other syntheses employed chemical vapor transport. In the conventional approach, one must first choose appropriate starting materials and try to get maximize surface area of reactants via grinding or cutting metal strips into several pieces. Secondly, weigh one out reactants, after choosing the target compound composition. Thirdly, starting materials are well mixed by grinding or

pulverizing a ball mill which helps minimizing a contact with the crucible, if a crucible is chose as a container. Selection of an appropriate reaction container is important; we use ceramic refractories (crucibles) or an Nb tube and then, seal them in a Quartz jacket under vacuum. Finally, a specific temperature cycle into a controller governs the heat supplied by a furnace. The selection of the reaction temperature and the rate of temperature gradient are very important in reactions discussed here, because the sensitivity of these solid state reactions to the effect of diffusion. The diffusion coefficient increases with temperature and increase rapidly as the reactant reaches the melt points according to the Fick's law. Fick's law²⁵ describes the relations between diffusive flux and the concentration. The law is " $J = -D \left(\frac{d\alpha}{dx} \right)$ ". In the equation, 'J' is the diffusion flux. D is the diffusion coefficient (m^2/second). 'α' is denoted the amount of substances per unit volume (mol/m^3). 'x' is the position (m). Therefore, the length of an Nb tube is a factor in those reactions as well. In addition, the other fundamental concept on selecting the reaction temperature is based on the Tamman's Rule²⁶. Tamman's Rule suggests a temperature which reaches at least two-thirds of the melting points of the main reactants and reactions are impractically slow below that temperature.

2.1.2 Single-Crystal and Powder X-ray Diffractometer

Bruker single-crystal APEXII CCD diffractometers and Bruker powder diffractometers were used to collect data used to determine crystal structures and characterize the purity of samples. The SMART APEXII in the department of chemistry

at Texas A&M University is equipped with a 3-circle goniometer, APEXII-CCD area detector, plus low temperature device and molybdenum-radiation. It provides high resolution data for normal crystals and produces high quality data for structure determinations. A single-crystal sample was mounted on a loop in a glove box filled with N₂ for each measurement. The Bruker-AXS D8 advanced Bragg-Bretano X-ray powder diffractometer is equipped with D8 goniometer and copper X-ray radiation. The powder diffraction data is collected via using reflection geometry. Polycrystalline (powder) samples were prepared in a glove box for the measurements. General information about Bruke-AXS equipment can be found at the Bruker AXS website: www.bruker-axs.de

2.1.3 Quantum Design MPMS-XL SQUID Magnetometer

The Quantum Design MPMS-XL SQUID magnetometer was used for collecting the data of magnetization and magnetic susceptibility with AC and DC magnetic measurements. The MPMS²⁷ system includes four different superconducting components. Firstly, a superconducting magnet is applied to generate large magnetic fields. Secondly, a superconducting detection coil is used to couples inductively to the sample. Thirdly, a Superconducting Quantum Interference Device (SQUID) is connected to the detection coil. Finally, a superconducting magnetic shield is surrounding the SQUID. The sample is located in the detection coil which is connected to the SQUID device via wires and the sample moves through a system of the detection coils; then,

change the current from the superconducting detection coil in order to couple inductively to the SQUID. All Air-sensitive samples were prepared in a N₂-filled glove box.

2.1.4 Energy-Dispersive and Wavelength-Dispersive Spectrometry Systems

An Energy-Dispersive spectrometry (EDS)²⁸ system was used to obtain semi-qualitative analysis of our samples. Even for samples that are poorly suitable to EDS analysis, qualitative elemental analyses can be obtained often. A 15-KeV electron beam is required for a sample which is mounted on biotite mica in the measurement of EDS. The purpose of using Wavelength-Dispersive Spectrometry (WDS)²⁸ system on an electron microprobe is to do quantitative analysis and determine the concentration of each element in the sample. If a sample has a nice crystal surface for the measurement, the percentage of the major element (which have the amount at least $\geq 10\%$ by weight) can be roughly determined and the error is within $\pm 2\%$ of the calculated amount. The quantitative analysis is based on the ratio of the X-ray intensity from an element in an unknown sample to the intensity of a standard compound which has known composition. The standard compounds are KBr, SiO₂ and GdPO₄ in my measurements.

2.2 Theoretical Method

In this section, I will briefly describe two calculation methods I used in this work. One is density functional methods. The other one is semiempirical method which I used in this work is extended Hückel/tight binding method. The semiempirical extended Hückel theory (EHT) ignores the core electrons and uses a restricted basis set in the calculation, so it can generate fast evaluation of some properties. EHT is suitable for the system which has known experimental geometries for the adjustment of parameters. In order to understand the idea of two methods, a basic background about how to solve the Schrödinger equation, how to write the Hamiltonian of many-electron system, how to write a secular equation and the concept of Born-Oppenheimer approximation are required. Those concepts can be found in the textbook of quantum chemistry.²⁹

2.2.1 Extended Hückel/Tight Binding Method

The extend Hückel theory is a very fundamental one-electron semi-empirical MO method for nonplanar molecules. It was used by Wolfsberg and Helmholz³⁰ to calculate the energy of tetrahedral ions. This theory was further developed by Hoffmann.³¹⁻³⁴ Before we talk about the extended Hückel theory, we need to know the Hückel theory.³⁵ ³⁶ Hückel theory espouses five conventions to set up a secular equation: (i) The basis set is consisted of $2p$ orbitals of parallel carbon on each atom. (ii) The overlap between any two p orbitals is zero and the overlap of the p orbital with itself is one. The overlap

matrix is defined by using the Kronecker delta ($\delta_{ij}=S_{ij}$) (iii) The matrix element H_{ii} is usually presented as the symbol α which is the negative value of the ionization potential. (iv) The matrix element H_{ij} between parallel neighboring p orbitals is termed β which value is actually derived from experimental data. (v) The matrix elements H_{ij} between non-neighboring p orbitals are set to zero.

On the other hand, extended Hückel theory (EHT) espouses two conventions to set up a secular equation. (i) EHT ignores all core electrons and uses the Slater-type orbital (STO) to express the basis function of valence orbital wave function. The form is the following:

$$\Psi(r, \theta, \phi, \zeta, n, l, m) = r^{n-1} e^{-\zeta r} Y_l^m(\theta, \phi) \quad (2.1)$$

The symbols of n , l , and m are the principal quantum number, and the angular momentum quantum numbers. ζ is an exponent which is a parameter of a basis set and it is developed by Slater.³⁷ $Y_l^m(\theta, \phi)$ is the spherical harmonic function.

(ii) About the off-diagonal matrix element H_{ij} , it is expressed as:

$$H_{ij} = \frac{1}{2} C_{ij} (H_{ii} + H_{jj}) S_{ij} \quad (2.2)$$

S_{ij} is the overlap integral between the atomic orbitals i and j . C_{ij} is a constant which is an empirical value and usually taken as 1.75. The diagonal value of H_{ii} is an adjustable parameter and relative to the valence-shell ionization potential (VSIP).

Comparing to the simple Hückel theory, the Kronecker delta is not applied to the overlap matrix elements in the extended Hückel theory. In addition, the valence molecular orbitals in the extended Hückel theory contain the contributions of the valence atomic orbitals on each atom.

Based on the rules above to figure out the overlap matrix S and Hamiltonian matrix H ; in order to solve the secular equation we can set up a secular determinant as:

$$\begin{bmatrix} H_{11} - ES_{11} & \cdots & H_{1N} - ES_{1N} \\ \vdots & \ddots & \vdots \\ H_{N1} - ES_{N1} & \cdots & H_{NN} - ES_{NN} \end{bmatrix} = 0 \quad (2.3)$$

Then, solve the secular equation to get the energy. The secular equation can be presented as:

$$HC = SCE \quad (2.4)$$

There are two free extended Hückel theory programs available on the web. One is CAESAR³⁸, and the other one is YAeHMOP³⁹ which was used in this work.

2.2.2 Density Functional Method

Early approximations of DFT models have no variational principles established and some errors were found in molecular calculation. Until Hohenberg and Kohn⁴⁰ who

developed approximation methods to treat the interacting electrons proved that electron density $\rho(x,y,z)$ can determine the ground-state molecular energy, wave function and other electronic properties in 1964. The ground-state energy was also defined as the function of electron density with the formation:

$$E_0 = E_0[\rho] \quad (2.5)$$

However, the Hohenberg-Kohn theorem is not clear about how to find the electron density without the information of wave function. This problem was solved by Kohn and Sham⁴¹ who used the ground-state electron density to clearly define the exact ground-state purely electronic energy E_0 of n-electron molecule as:

$$E_0 = -\frac{1}{2} \sum_{i=1}^n \langle \varphi_i(1) | \nabla^2 | \varphi_i(1) \rangle - \sum_{\alpha} \int \frac{Z_{\alpha}}{r_{1\alpha}} dv_1 + \frac{1}{2} \iint \frac{\rho^{(1)}\rho^{(2)}}{r_{12}} dv_1 dv_2 + E_{XC}[\rho] \quad (2.6)$$

The first term is kinetic energy which is integrated over the coordinates of electron 1. The $\varphi_i(1)$ is Kohn-Sham orbitals²⁹. The $\varphi_i(1)$ and $\rho(1)$ are treated as the function of the coordinates of electron(1). The notation $E_{XC}[\rho]$ indicates the exchange-correlation energy which is a function of ρ . The symbol “ ρ ” presents the exact ground-state electron density which can be found from Kohn-Sham orbitals according to the equation below:

$$\rho = \sum_{i=1}^n |\varphi_i|^2 \quad (2.7)$$

Via solving the one-electron equation below, the Kohn-Sham orbitals can be obtained.

$$\hat{F}_{ks}(1)\varphi_i(1) = \varepsilon_{iks}\varphi_i(1) \quad (2.8)$$

The notation \hat{F}_{ks} is the Kohn-Sham operator as:

$$\hat{F}_{ks} \equiv -\frac{1}{2}\nabla_1^2 - \sum_{\alpha} \frac{z_{\alpha}}{r_{1\alpha}} + \sum_{j=1}^n \hat{J}_j(1) + V_{XC}(1) \quad (2.9)$$

The symbol $\hat{J}_j(1)$ is Coulomb operator²⁹ and the notation $V_{XC}(1)$ is the exchange-correlation potential which can be found via taking a derivation of $E_{XC}[\rho]$.

Finally, we can substitute (2.9) into (2.8) to get the eigenfunctions which are the Kohn-Sham orbitals. One thing needs to be known that Kohn-Sham orbitals are used to calculate the exact electron density and there is no physical significance. The only problem of using the Kohn-Sham equations to get ρ and energy is how to get the correct functional exchange correlation energy $E_{XC}[\rho]$.for molecules. Therefore, the concept of local density approximation (LDA) and local spin-density approximation (LSDA)^{42, 43} were come up in order to get a closer approach.

The discussion above and the details about the density functional theory and extended Hückel theory can be found in the publications of Cramer⁴⁴ and Levine²⁹.

3. GADOLINIUM LAYER COMPOUNDS

3.1 Synthesis

I. $Gd_9Br_{16}O_4$ was first obtained as a minor by-product in a reaction intended to prepare the target compound, $Gd_6Br_7Ge_2$. The stoichiometric mixing of the starting materials $GdBr_3$ ⁴⁵, gadolinium, and germanium in a niobium tubes was designed to synthesize $Gd_6Br_7Ge_2$. Although the mixing procedure was carried out in a glove box under N_2 atmosphere, typical adventitious impurities, such as occur upon hydrolysis of $GdBr_3$, for example, may be inside the tube that caused $Gd_9Br_{16}O_4$ to be obtained. The reaction was heated at 1000 °C in a sealed niobium tube for 3 weeks. Black irregular crystals and shiny round black crystals are recognized as $Gd_9Br_{16}O_4$ and Gd_5Ge_3 ⁶(known). The major phase, black tiny unknown crystals, has not been identified successfully. All crystals are sensitive to moisture and air. Three reactions were tried in order to reproduce $Gd_9Br_{16}O_4$. (i) The stoichiometric mixing of Gd_2O_3 , $GdBr_3$, and Gd. (ii) Using impure $GdBr_3$ which contains $GdOBr$ (assumed the ratio is 1:1), as a starting material and stoichiometric mixing of Gd. (Oxyhalides is the source of impurity in the preparation of trihalides via the ammonium halide route⁴⁵) (iii) The stoichiometric mixing of $GdOBr$ ⁴⁶, $GdBr_3$, and Gd. Minor black crystals and major white or gray powder would be obtained from those three reactions (Black crystals may be attached on the wall of Nb tubes). After indexing and using CELL_NOW to analyze the cell constants of black crystals, the results match the cell constants of $Gd_9Br_{16}O_4$.

II. $\text{Gd}_6\text{Br}_7\text{Si}_2$ was obtained by the stoichiometric mixing of the starting materials GdBr_3 , gadolinium, and silicon in a niobium tubes. The reaction was heated at 1000 °C for 2 weeks. The mixing procedure was carried out in a glove box under N_2 atmosphere. Black rectangular crystals are obtained. The compound is sensitive to moisture and air.

3.2 Single-Crystal X-ray Diffraction

Black crystals of dimensions 0.115 x 0.045 x 0.060 mm³ for 1 and 0.019 x 0.038 x 0.076 mm³ for 2 were selected for indexing and data collecting on a Bruker APEX II diffractometer at low temperature (110 K). The program SADABS⁴⁷ and face indexing were applied for absorption correction. The structures were solved by direct methods and difference Fourier syntheses. The final cycles of least-squares refinement including atomic coordinates and anisotropic thermal parameters for all atoms were converged. There were residual electron densities in the final difference map which are close to heavy atoms Gd(1) in I and close to heavy atoms Gd(1), Gd(2) and Gd(3) in II. Use the SHELXTL⁴⁸ version 6.12 software package to perform all structure refinements. The selected bond length for $\text{Gd}_6\text{Br}_7\text{Si}_2$ is seen in Table 3.1. As seen in Table 3.2(a), Table 3.2(b) and Table 3.3 are the information of atomic coordinates, equivalent isotropic thermal displacement parameters and the crystallographic data of compound I and II.

Table 3.1. Selected bond lengths [\AA] for $\text{Gd}_6\text{Br}_7\text{Si}_2$

d (Si-Gd)	\AA	d(Si-Gd)	\AA	d(Br-Gd)	\AA
Si(1)-Gd(1)#5	2.881(2)	Si(2)#1-Gd(1)	2.886(8)	Br(4)-Gd(1)#6	2.886(8)
Si(1)-Gd(1)#6	2.881(2)	Si(2)#3-Gd(2)	2.875(8)	Br(4)-Gd(2)#3	2.875(8)
Si(1)-Gd(1)#2	2.881(2)	Si(2)#1-Gd(2)	2.885(6)	Br(4)-Gd(2)#6	2.885(6)
Si(1)-Gd(3)#5	2.880(2)	Si(2)#1Gd(3)	2.880(6)	Br(4)-Gd(3)#6	2.880(6)

Symmetry transformations are used to generate equivalent atoms:

#1 $x, y+1, z$

#2 $-x, -y, -z$

#3 $-x+1/2, -y-3/2, -z$

#4 $-x+1/2, -y-1/2, -z$

#5 $-x, -y-1, -z$

#6 $x, y-1, z$

Table 3.2(a). Atomic coordinates and equivalent isotropic displacement parameters ($\text{\AA}^2 \times 10^3$) for $\text{Gd}_6\text{Br}_7\text{Si}_2$. $U(\text{eq})$ is defined as one third of the trace of the orthogonalized U_{ij} tensor.

	x	y	z	$U(\text{eq})$
Gd(1)	0.0923(1)	0	0.1654(2)	13(1)
Gd(2)	0.2591(1)	-0.5000	0.1656(2)	14(1)
Gd(3)	0.0743(1)	-0.5000	-0.1655(3)	14(1)
Br(1)	0.0212(2)	0	0.3444(5)	13(1)
Br(2)	0.3544(2)	-1.0000	0.3446(5)	12(1)
Br(3)	0.1875(2)	-0.5000	0.3443(5)	12(1)
Si(1)	0	-0.5000	0	23(1)
Br(4)	0.1666(4)	-1.0000	-0.0007(9)	23(1)
Si(2)	0.1666(4)	-1.0000	-0.0007(9)	23(1)

Table 3.2(b). Atomic coordinates and equivalent isotropic displacement parameters ($\text{\AA}^2 \times 10^3$) for $\text{Gd}_9\text{Br}_{16}\text{O}_4$. $U(\text{eq})$ is defined as one third of the trace of the orthogonalized U_{ij} tensor.

	x	y	z	$U(\text{eq})$
Gd(1)	0.8222(1)	0.5951(1)	0.0195(1)	12(1)
Gd(2)	0.7830(1)	0.7707(1)	0.0417(1)	12(1)
Gd(3)	0.6250	0.6250	0.1250	13(1)
Br(1)	0.8376(2)	0.5984(1)	-0.0568(1)	14(1)
Br(2)	0.9111(2)	0.6681(1)	0.0855(1)	15(1)
Br(3)	0.10804(2)	0.7040(1)	0.0057(1)	14(1)
Br(4)	0.7526(2)	0.5145(1)	0.0842(1)	14(1)
O(1)	0.5634(19)	0.5621(7)	0.0116(4)	29(4)

Table 3.3. Crystal data and structure refinements for Gd₉Br₁₆O₄ (I) and Gd₆Br₇Si₂ (II)

Identification code	Gd ₉ Br ₁₆ O ₄	Gd ₆ Br ₇ Si ₂
Empirical formula	Gd ₉ Br ₁₆ O ₄	Gd ₆ Br ₇ Si ₂
Formula weight	2757.76	1558.96
Temperature	110(2) K	110(2) K
Wavelength	0.71073 Å	0.71073 Å
Crystal system	Orthorhombic	Monoclinic
Space group	<i>Fddd</i>	<i>C2/m</i>
Unit cell dimensions	a = 8.1902(4) Å b = 20.9843 (9) Å c = 38.840(2) Å	a = 21.415(5) Å b = 4.123 (1) Å c = 10.907(3) Å β=115.891(3)°.
Volume (Å ³)	6675(5)	866.5(4)
Z	8	2
Crystal size (mm ³)	0.0115 x 0.045 x 0.060	0.019 x 0.038 x 0.076
Refinement method	least-squares on F ²	least-squares on F ²
Goodness-of-fit on F ²	0.944	0.901
Final R indices [I>2σ(I)]	R1 = 0.0411, wR2 = 0.0930	R1 = 0.0353, wR2 = 0.0845
Absorption correction	0.367751/ 1.0000	0.3774/ 0.9621
Largest diff. peak and hole (e.Å ⁻³)	2.130 and -2.420	2.825 and -3.111

Weight = 1 / [$\sigma^2(F_o^2) + (0.0404 * P)^2 + 0.00 * P$] where $P = (\text{Max} (F_o^2, 0) + 2 * F_c^2) / 3$ for **(I)**

Weight = 1 / [$\sigma^2(F_o^2) + (0.0439 * P)^2 + 8.95 * P$], where $P = (\text{Max} (F_o^2, 0) + 2 * F_c^2) / 3$ for **(II)**

3.3 Powder X-ray Diffraction

Figure 3.1 is the result of characterizing $\text{Gd}_6\text{Br}_7\text{Si}_2$ phase via using TOPAS program. Since the crystal structure is refined by the data from single-crystal X-ray diffraction, the purpose of the using TOPAS is to verify the existence of target phase in the powder sample and do the quantitative phase analysis. The green peak is the calculated powder pattern of $\text{Gd}_6\text{Br}_7\text{Si}_2$ from the sing-crystal X-ray data. The read fitting curves include three calculated powder patterns of three phases: GdOBr , GdBr_3 and $\text{Gd}_6\text{Br}_7\text{Si}_2$. From the match between the experimental powder pattern (blue peaks) and green peaks, it shows the existence of $\text{Gd}_6\text{Br}_7\text{Si}_2$. This experimental powder pattern here can only provide the information of qualitative analysis to verify the phase of $\text{Gd}_6\text{Br}_7\text{Si}_2$, and it can not be used as a quantitative analysis due to containing some unclassified peaks.

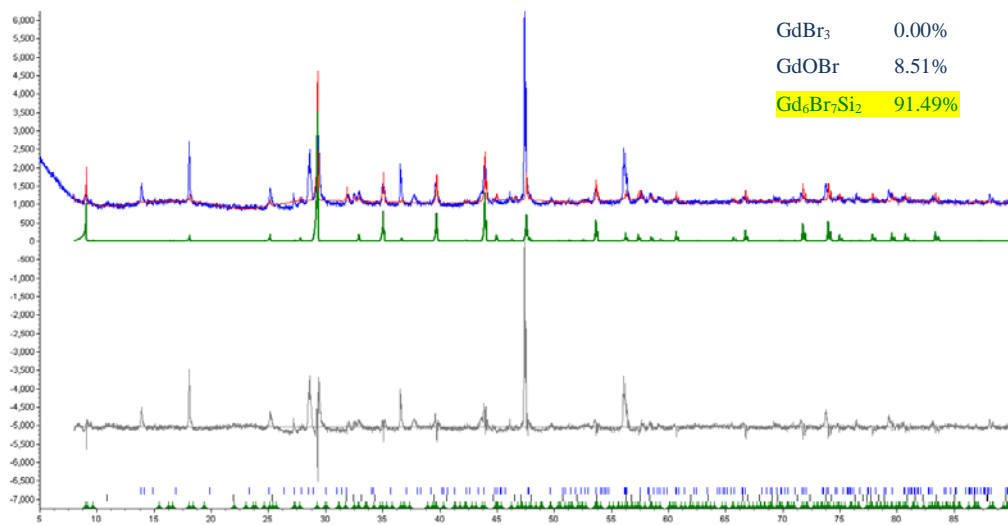


Figure 3.1. The result of characterizing $\text{Gd}_6\text{Br}_7\text{Si}_2$ phase from TOPAS

3.4 Microprobe Analyses

Energy-dispersive spectrometry (EDS)⁴⁹ systems and wavelength-dispersive spectrometry (WDS)⁴⁹ were used in the qualitative and quantitative analysis for $\text{Gd}_9\text{Br}_{16}\text{O}_4$ and $\text{Gd}_6\text{Br}_7\text{Si}_2$. Figure 3.2 and Figure 3.3 are the results of EDS measurements. The result confirms the existence of Gd, Si, and Br elements in $\text{Gd}_6\text{Br}_7\text{Si}_2$. Also, it confirms the components of Gd, Br and oxygen in $\text{Gd}_9\text{Br}_{16}\text{O}_4$. However, the samples were transferred into the instrument under air, so the peak which indicates the component of oxygen in the figures is of questionable value. Figure 3.4 (a) Right and (b) left are the secondary electron (SE) image and backscattered electron (BSE) images of $\text{Gd}_9\text{Br}_{16}\text{O}_4$. BSE and SE images can provide the topographic information of surface, and different surface details are usually more visible in BSE images. Because of extreme air sensitivity and poor sample surface, the results of WDS measurements did not exhibit reportable precision for both samples in the quantitative analysis. Samples were prepared in a glove box, but exposure to air could not be prevented during the process of transferring sample holders into the instrument.

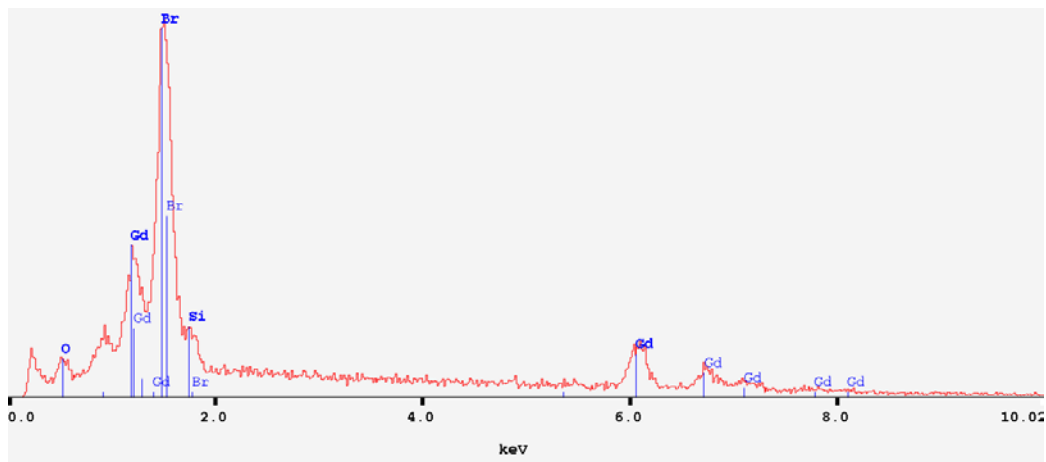


Figure 3.2. Energy-dispersive spectrometry of $Gd_6Br_7Si_2$

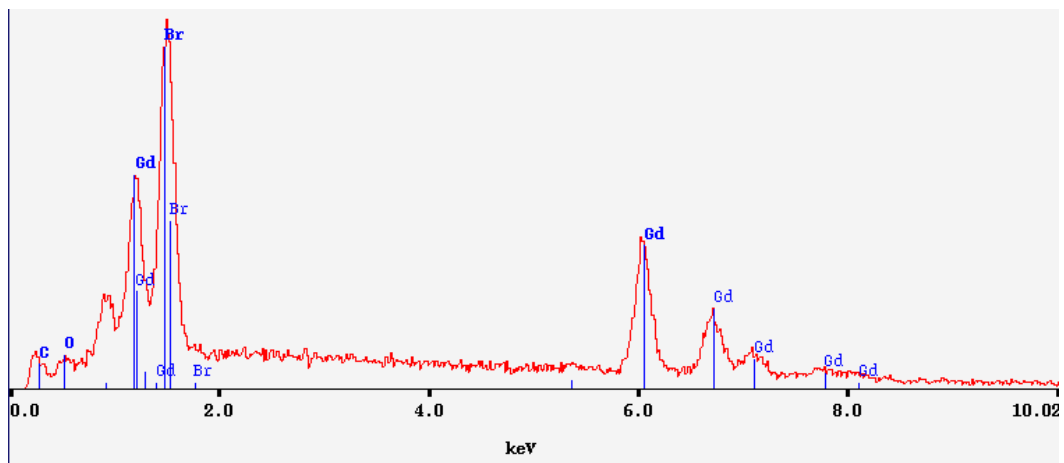


Figure 3.3. Energy-dispersive spectrometry of $Gd_9Br_{16}O_4$

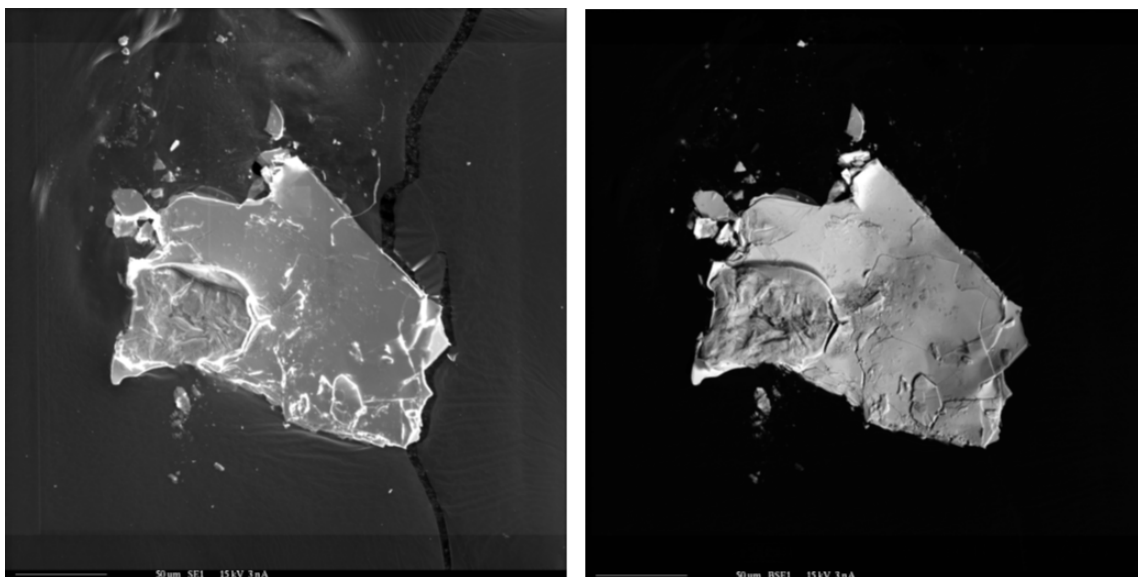


Figure 3.4(a). Left and (b) Right are the SE image and BSE images of $\text{Gd}_9\text{Br}_{16}\text{O}_4$

3.5 Magnetic Measurements

Magnetic measurements were performed with a Quantum Design SQUID magnetometer MPMSXL on polycrystalline samples of $\text{Gd}_6\text{Br}_7\text{Si}_2$ and $\text{Gd}_9\text{Br}_{16}\text{O}_4$. Temperature-dependent magnetization⁵⁰ data were collected at 2-5 K intervals from 2 to 300 K in applied fields of 0.01, 0.1, and 1 T. All data were corrected for the sample holder contribution and for the intrinsic diamagnetic contributions.⁵¹ The magnetic property of $\text{Gd}_6\text{Br}_7\text{Si}_2$ at an applied field (0.1T) is shown in Figure 3.5(a). This compound exhibits distinct magnetic properties at different temperature range. From 300 to 70 K, the data show paramagnetic behavior and the presence of ferromagnetic coupling. At around 70 Kelvin, it appears the first phase transition. After the first phase transition, the effect of antiferromagnetic coupling between 70 and 27 K becomes

obvious; then, the second phase transition occurs at about 27 K. Below 27 K, it may be a magnetically canted phase.

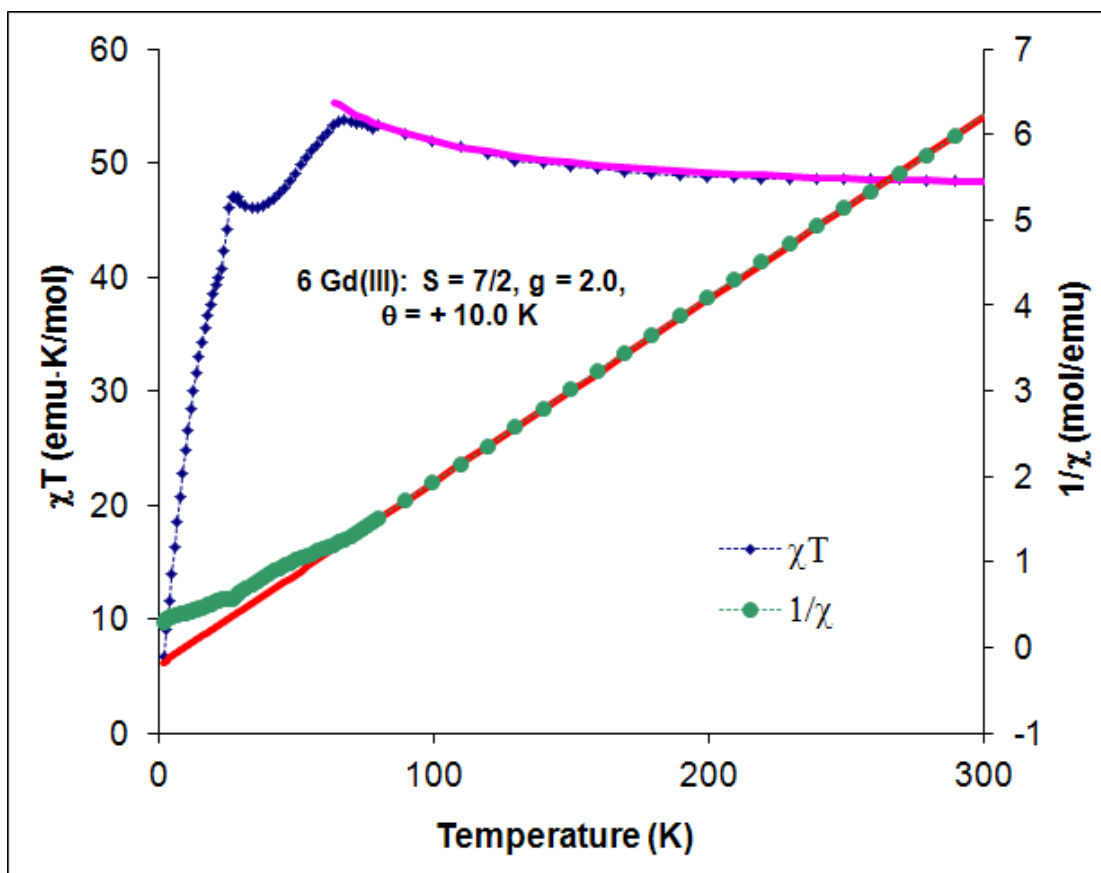


Figure 3.5(a). (Left Axis): The plot of χT vs T for $\text{Gd}_6\text{Br}_7\text{Si}_2$ at an applied field (0.1T) is labeled by blue dotted-line. The Curie constant for an “ideal” cluster with six uncoupled Gd^{III} centers ($S=7/2$; $g=2$) is $47.25 \text{ emu K mol}^{-1}$. The Curie-Weiss fit to $\text{Gd}_6\text{Br}_7\text{Si}_2$ is shown as the pink line and T_c is at 10K. (Right Axis): The plot of $1/\chi$ vs T for $\text{Gd}_6\text{Br}_7\text{Si}_2$ is the green dotted-line. The Curie-Weiss fit to $\text{Gd}_6\text{Br}_7\text{Si}_2$ is shown as the red line

A canted phase is caused by a physical phenomenon, a canting of the spins; originally, this substance should be antiferromagnetic primarily, but there exists a weak ferromagnetism⁵². In this sample, a canted phase is possible because $\text{Gd}_6\text{Br}_7\text{Si}_2$ presents ferromagnetic coupling at higher temperature region (> 70 K); then it turns antiferromagnetic coupling below 70. K, but weak ferromagnetic coupling is reproduced again at 27 K due to a canting of the spins. Therefore, the overall effect described above may generate the canted phase. Some Gd ternary systems^{53, 54} which contain two nonmagnetic elements, exhibit the phenomenon of crossover from a ferromagnetic phase to antiferromagnetic phases, such as $\text{GdPt}_{0.5}\text{Al}_{0.5}$ which also has the canted configuration.

At higher temperature (> 70 K), normally, spin orientations on Gd metal should be random. However, when we apply an external magnetic field (0.1 T) to $\text{Gd}_6\text{Br}_7\text{Si}_2$, the moments are all aligned in the same direction in this sample and it shows ferromagnetic coupling. At low temperature, exchange energy can compete with the thermal energy. A short-range correlation within the moments of exchange interaction may start to accumulate. When the effects is observed in a long-range scale, a transition from ferromagnetic moment to another magnetic moment with long range correlations between the moments is called a phase transition, which happens at 70 K and 27 K in this compound. The magnetic properties of $\text{Gd}_6\text{Br}_7\text{Si}_2$ should be caused by the moment of Gd atoms at the octahedra sites. They may have different coupling between the adjacent chains and layers.

In rare-earth intermetallic compounds, usually the magnetic ordering is due to an indirect pathway involving the localized $4f$ electrons and the conduction band. The

exchange coupling to the conduction electrons can be very important. For examples, $\text{Nd}_2\text{Fe}_{14}\text{B}$ and SmCo_5 ⁷ are permanent magnets. Elemental gadolinium is a metallic ferromagnet at 294 K. Many studies have been proposed to understand the ferromagnetic or antiferromagnetic order, such as the satisfactory model of Ruderman-Kittel-Kasuya-Yosida (RKKY)⁵⁵ which is described with oscillatory terms and a periodic magnetic order is depend on $K_f R_{ij}$, where R_{ij} presents the distance between the magnetic ions.

Although the Curie-Weiss fit to $\text{Gd}_6\text{Br}_7\text{Si}_2$ is well, all data needs to be re-confirmed again by measuring highly pure samples. If a result of neutron diffraction experiments on single crystals of $\text{Gd}_6\text{Br}_7\text{Si}_2$ is available, it will provide more detail information concerning the phase transitions.

The sample of $\text{Gd}_9\text{Br}_{16}\text{O}_4$ is hand-picked crystals. The magnetic measurement of $\text{Gd}_9\text{Br}_{16}\text{O}_4$ is unable to show good results due to insufficient samples. Besides, the sample is highly air-sensitive and it is easily oxidized.

The result of magnetic hysteresis measurement at 2 Kelvin for $\text{Gd}_6\text{Br}_7\text{Si}_2$ is seen in Figure 3.5(b). The hysteresis loop⁵⁶ is completed after applying a cyclic magnetic field. The magnetization starts from zero magnetic fields and reaches the max valued of magnetization (saturation magnetization). The hysteresis loop is narrow and a small value of coercive field (H_c) that means $\text{Gd}_6\text{Br}_7\text{Si}_2$ is a soft magnet which only requires a small amount of dissipated energy in order to recurrently reverse the magnetization. There is a “residual magnetization (M_r)” observed at $H=0$, and the residual magnetization correspond to the real spontaneous magnetization which can be seen in Figure 3.5(c) as well.

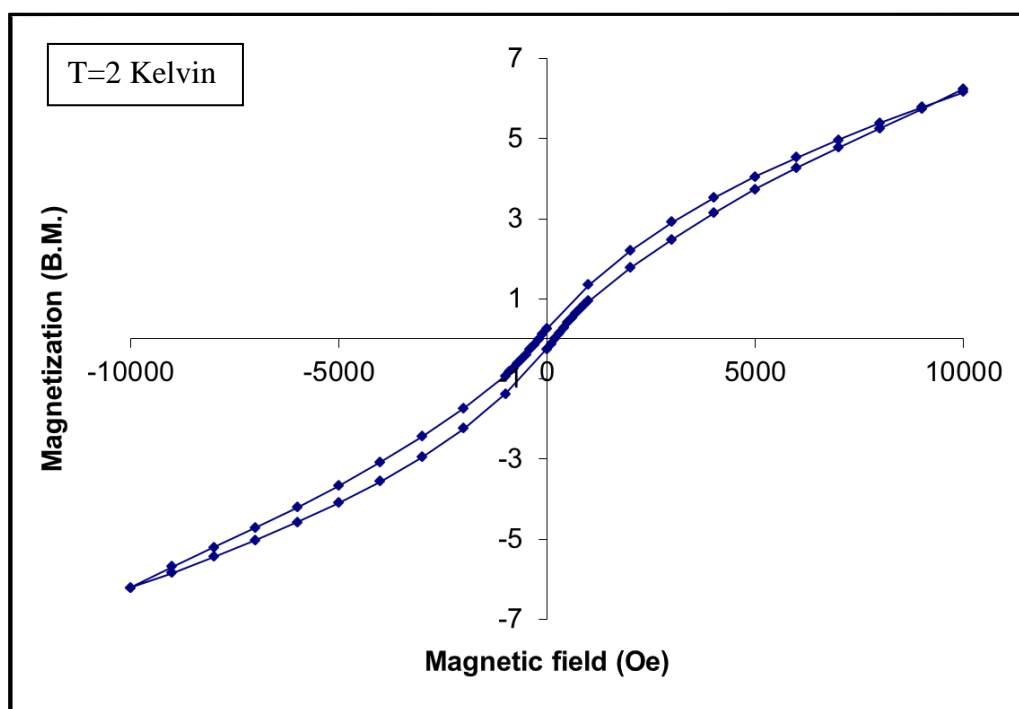


Figure 3.5(b). The result of magnetic hysteresis measurement at 2 Kelvin for $\text{Gd}_6\text{Br}_7\text{Si}_2$

The pink curve shows the remanent magnetization (RM) in Figure 3.5(c). The “remanent magnetization” is an equal term of “residual magnetization (M_r)” which is usually used in engineering applications. A small residual magnetization is preferred in the application of transformer. The property of remanent magnetization is relative to the application of magnetic memory which can be used in the magnetic storage devices.

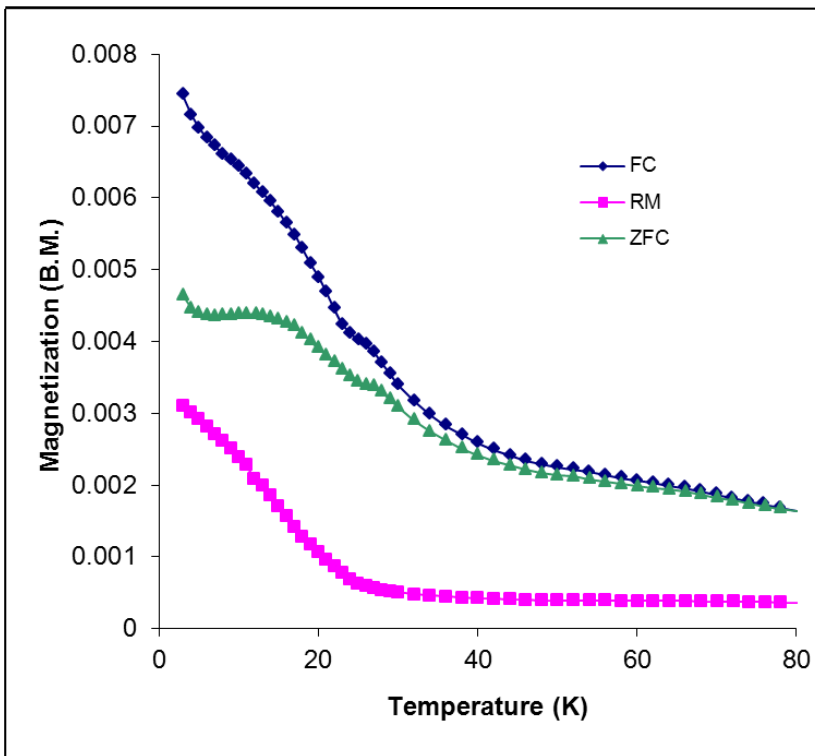


Figure 3.5(c). A plot shows the result of zero field cooling and field cooling measurements. The pink curve is the remanent magnetization of $Gd_6Br_7Si_2$.

3.6 Crystal Structures

3.6.1. $Gd_9Br_{16}O_4$: A 3-D Structure with a Reduced Metal Layer

A black crystal of a new compound $Gd(Gd_8Br_{16}O_4)$ was synthesized in a solid state reaction. Figure 3.6 shows that the structure has 2D metal layers and it can be described in the term of oxo-centered OGd_4 tetrahedra. Oxo-centered tetrahedra form one-dimensional ${}^1_{\infty}[Gd_2O]$ zigzag chains by edge sharing. The cationic ${}^1_{\infty}[Gd_2O]$ chains are connected together via Br3 atom to construct a 2-D network.

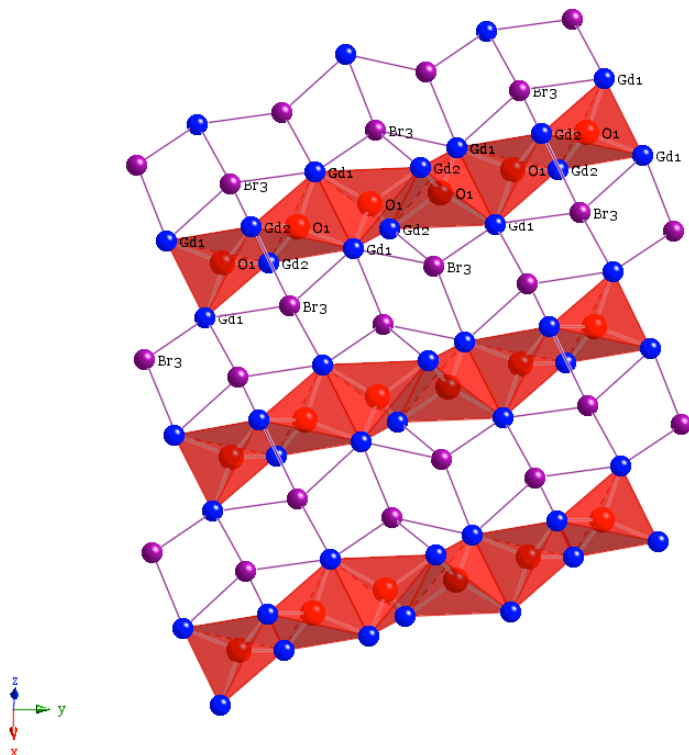


Figure 3.6. The 2-D metal layer of $Gd_9Br_{16}O_4$. The color of each atom is the following: blue (Gd), purple (Br3), red (Oxygen), and red oxy-centered tetrahedron (OGd_4 tetrahedra).

Layers are interleaved by 8-coordinated gadolinium intra form of GdBr_8 square antiprisms polyhedra which are like pillars that separate layers (Figure 3.7).

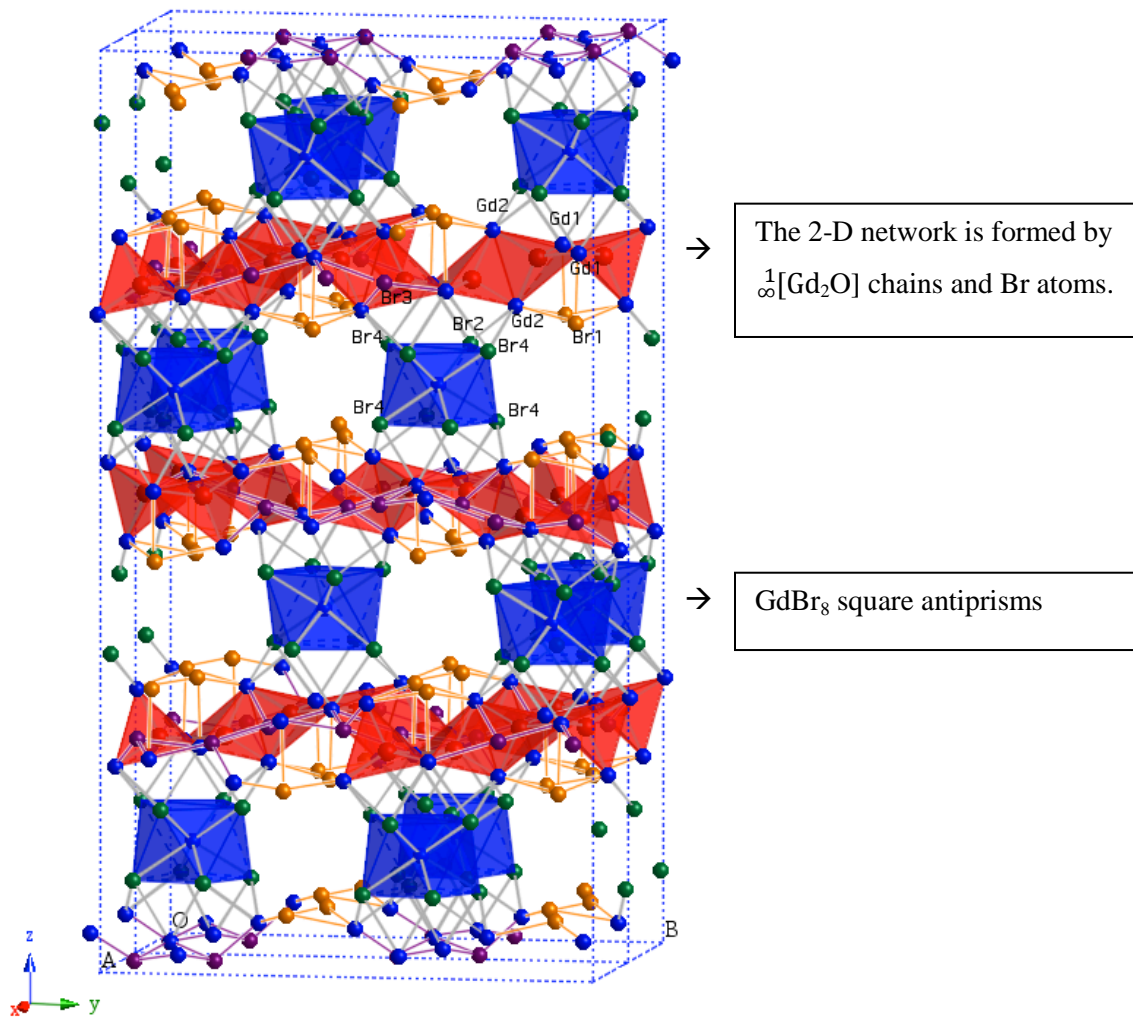


Figure 3.7. The structure of $\text{Gd}_9\text{Br}_{16}\text{O}_4$. The color of each atom is the following: blue (Gd), orange (Br1), green (Br2& Br4), purple (Br3), red (Oxygen), and red oxy-centered tetrahedron (OGd_4 tetrahedra).

This compound has interesting and variable coordination environments. In the structure, there are three types of Br atoms. Firstly, Br2 and Br4 atoms form square antiprisms that surround Gd3 atoms. The coordination numbers (CN) of Br2 and Br4 atoms have of three. Secondly, Br3 atoms sit among layers and connect to Gd1 and Gd2 atoms constructing a zigzag network; the CN of Br3 atoms is four. Thirdly, Br1 atoms sit either on the top or at the bottom of Gd1 atoms just like a decoration within the interval of the tetrahedra-zigzag chains.

Gd1 and Gd2 atoms are connected to each other to form tetrahedra that are centered by an oxygen atom. Within the edge sharing tetrahedral chains, the interatomic distance of shared edges, Gd2-Gd2, is 3.950 Å which is longer than the other sharing edges, Gd1-Gd1 (3.465 Å) and Gd1-Gd2 (3.785 Å), as seen in Figure 3.8. The CN of Gd1, Gd2 and Gd3 are 13, 12 and 8 respectively. Counting the charges of the formula $(\text{Gd}^{+3})_9(\text{Br}^{-1})_{16}(\text{O}^{2-})_4(\text{e}^-)_3$, there are three electrons left. Additional electrons are attractive to positive layers ${}_{\infty}^2[\text{Gd}_2\text{O}_1\text{Br}_2]$, so the metal layers are reduced.

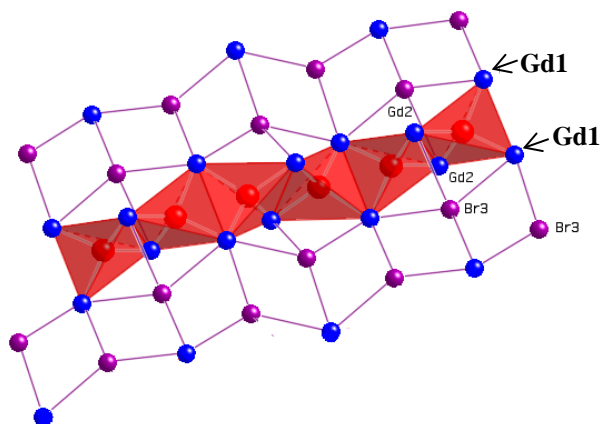


Figure 3.8. A single chain structure within the layer of $\text{Gd}_9\text{Br}_{16}\text{O}_4$.

3.6.2 $Gd_6Br_7Si_2$: Two Types of Interstitial Atoms with a Layer Structure

The structure of $Gd_6Br_7Si_2$ exhibits two dimensional layers, as seen in Figure 3.9(a). Each layer consists of two different interstitially chains of edge-sharing Gd_6Z octahedra ($Z=Si, Si/Br$), as shown in Figure 3.9(b).

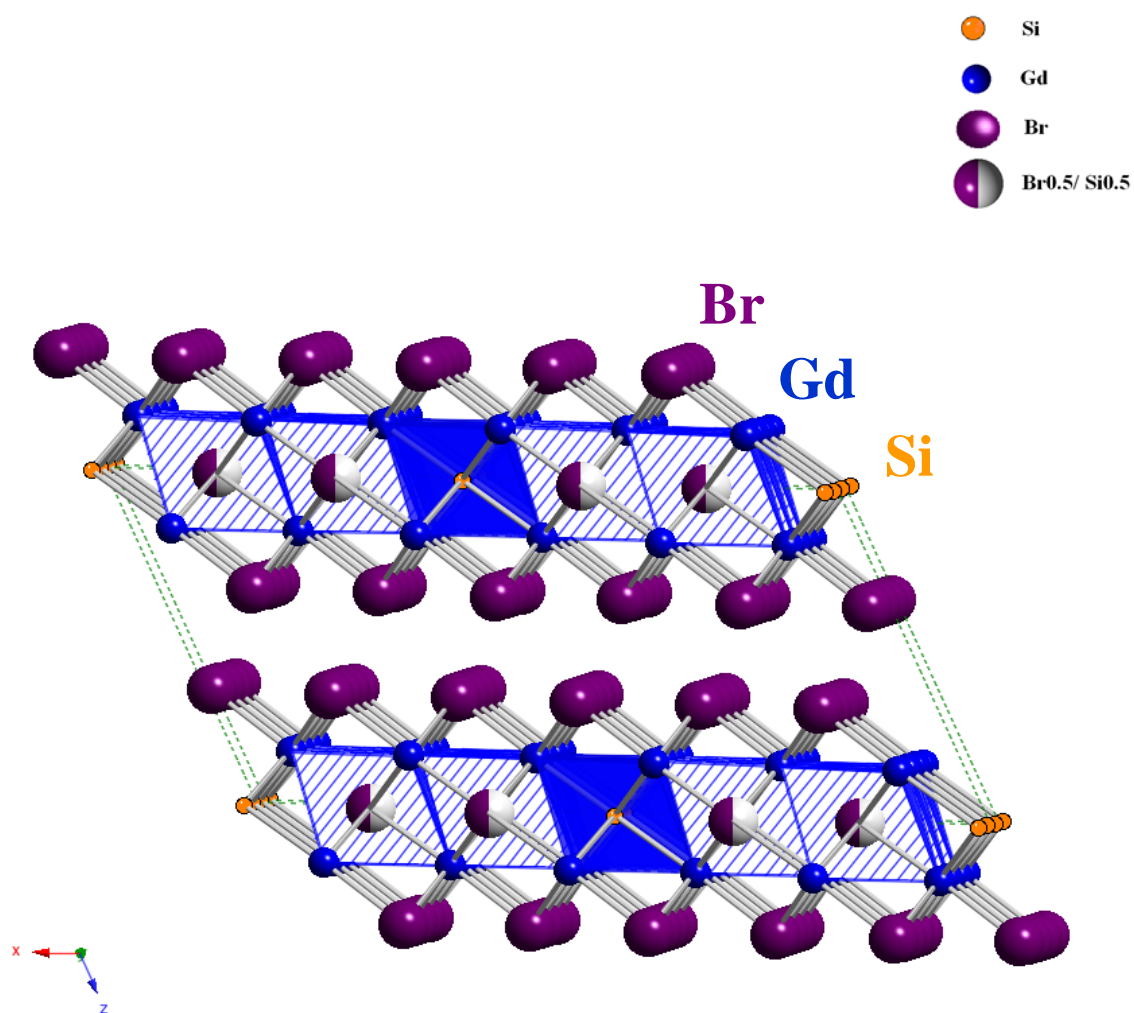


Figure 3.9(a). The structure of $Gd_6Br_7Si_2$ is a layer. Green dashed line is drawn to show a unit.

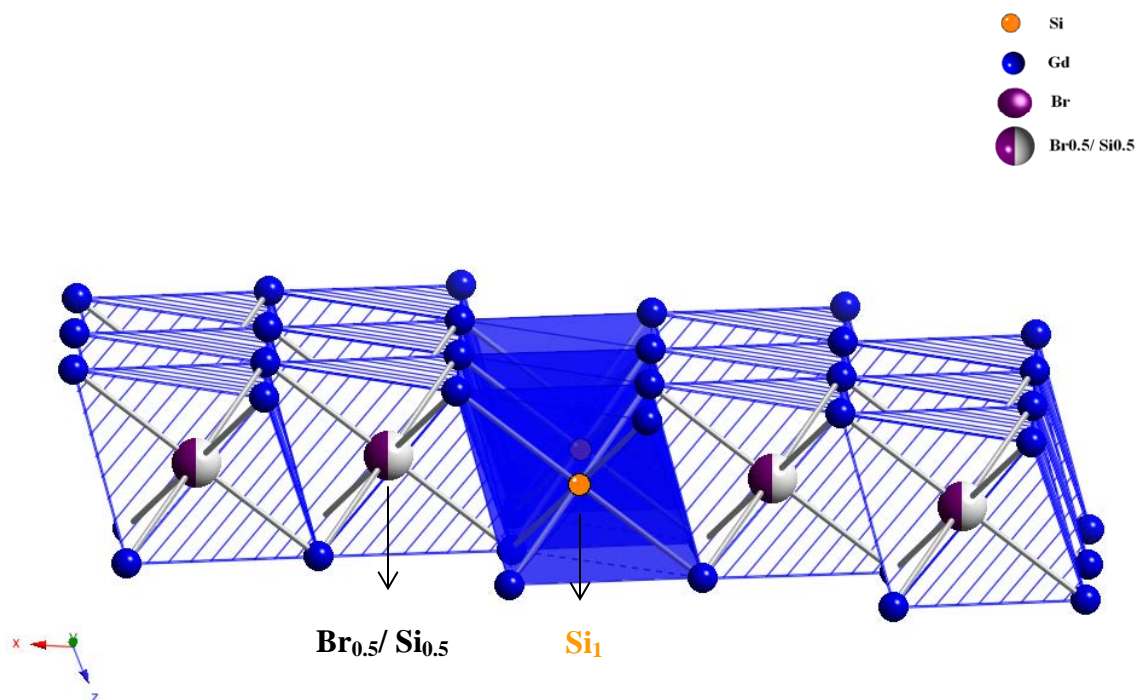


Figure 3.9(b). There are two types of interstitial chains in every layer. The interstitial atoms centered in the blue octahedra are Si(1) atoms. The centers of grid octahedra are half occupied by Si(2) and Br(4). Blue atoms are gadolinium.

For each octahedron, the Gd-Gd bond length of sharing edge is 4.026 Å and 4.028 Å. The bond length without sharing edge is 4.123 Å. The interstitial atoms centered in the oblique octahedra are not shown in order to get a clear view on the connection between each octahedron in Figure 3.10.

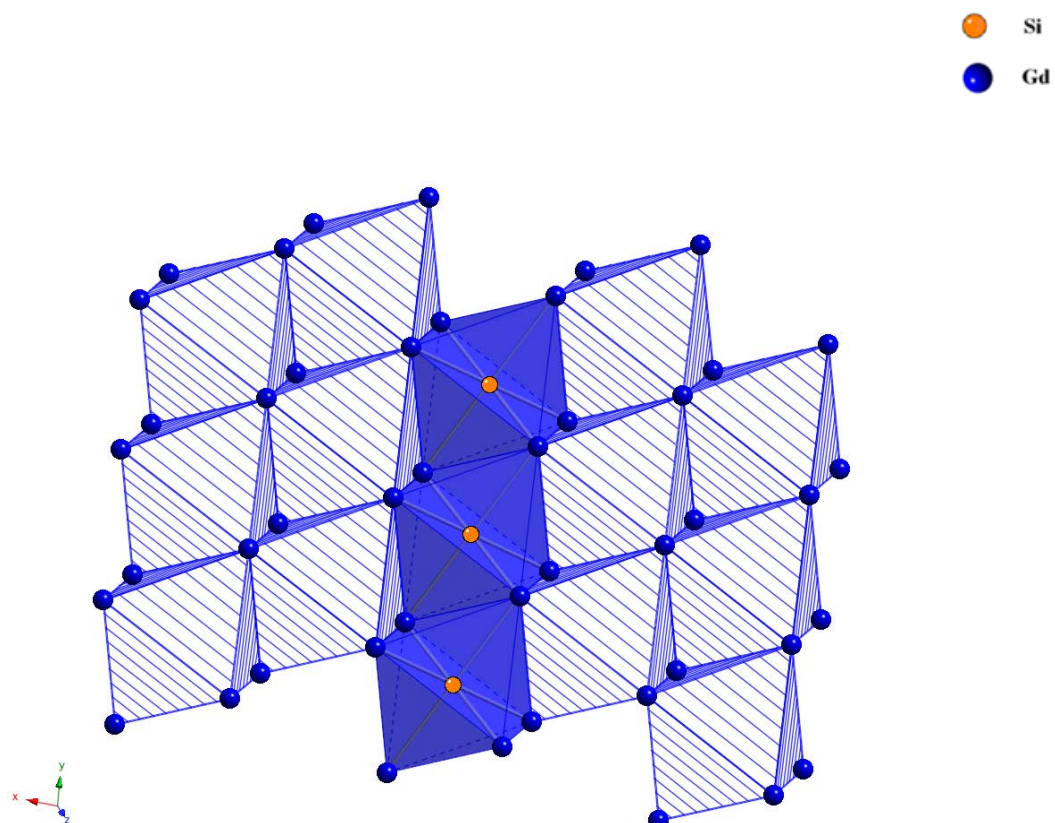


Figure 3.10. Different interstitially stabilized chains are labeled distinctly. Two edges are sharing with neighboring chain for each octahedron.

The interstitial atoms centered in the blue octahedral are Si (1) atoms which occupy the special positions: (0, 1/2, 0) (see Table 3.2.). The other interstitial atoms sit in the center of oblique octahedra are Si(2) and Br(4). This position is a substitutionally disordered; in our structure model, the site is half occupied with both Si(2) and Br(4) atoms. During the process of refinement, Si(1), Si(2) and Br(4) are position-related because all of them are centered in the Gd₆ octahedra. As seen in Table 3.1, the bond lengths between Gd and interstitial Br(4), d(Gd(1)-Br(4))=2.886(8) Å, d(Gd(2)-Br(4))=2.885(6) Å, are shorter than the terminal Gd-Br bonds, d(Gd-Br)= 2.956(4) ~ 2.959(5) Å. The bond lengths between Gd and interstitial Si(2) or Si(1), d(Gd(1)-Si(2))=2.886(8) Å, d(Gd(2)-Si(2))=2.875 and 2.885(8) Å, are slightly different from the Gd(2)-Si(1) bonds, d(Gd(1)-Si(1))=2.881(2) Å. Comparing to Gd₄Br₆Si₂¹⁸ which has the bond length of Gd-Si from 2.741(1) ~ 2.807(1) Å, the Gd-Si distances of Gd₆Br₇Si₂ are from 2.875(8) ~ 2.886(8) Å.

Numerous interesting structures exist amongst rare earth metal halide compounds, and most of them are built up with condensed of M₆X₈ or M₆X₁₂ clusters⁵⁷ building blocks. This Gd₆Br₇Si₂ layer structure contains M₆X₁₂ type building units. Comparing to Gd₂Br₂C₂⁵⁸, both of them have similar layer which are derived from Gd₆Br₁₂ cluster, but they have different cell constants. (Gd₂Br₂C₂, C2/m, a = 7.025 Å, b = 3.836 Å, c = 9.868 Å, β= 94.47). The d(Gd-Gd) of Gd₂Br₂C₂ are from 3.45 to 4.00 Å and the d(Gd-Gd) of Gd₆Br₇Si₂ are from 4.024(5) to 4.027(4) Å. Besides, Gd₆Br₇Si₂ can be considered as (Gd⁺³)₆(Br⁻)₇(Si⁻⁴)₂(e⁻)₃, so there are an excess of electrons. However, for Gd₂Br₂C₂, the ionic framework (Gd⁺³)₂(Br⁻¹)₂ is assumed to provide 4 electrons per C₂ unit.

3.7 Calculated Electronic Structure

3.7.1 The Electronic Structure of $Gd_9Br_{16}O_4$

The electronic structure of $Gd_9Br_{16}O_4$ was investigated by use of density functional theory (DFT) with the Becke exchange functional and the Lee-Yang-Parr correlation functional (BLYP)^{59, 60} and extended Hückel tight binding theory (EHTB). The DFT calculations presented here were performed using the DMol³ program from the Materials Studio suite of programs using the double numerical basis including d-polarization functions (DND).⁶¹⁻⁶³ A small frozen-core (1s2s2p3s3p3d), (1s2s2p) and (1s2s2p3s3p) effective potential were used for Gd and Br respectively. All calculations included scalar relativistic effects and open shell configurations. At the beginning, a nonmagnetic analogue, $Y_9Br_{16}O_4$, was used as a model to run the DFT and EHTB calculations in order to consider an *f*-orbital free analog. (The electron configuration of the Gd atom is “[Xe]4*f*⁷6s²5d¹” and the electron configuration of Y is “[Kr]5s²4d¹”.) The lattice parameter and coordinates of $Y_9Br_{16}O_4$ were used from the crystallographic data of $Gd_9Br_{16}O_4$ and the scaling of the lattice parameters due to different metal radius were considered via calculating the ratio of volumes between the real compounds: GdB_2C_2 and YB_2C_2 . After applying the cube root of the ratio to the lattice constants of $Gd_9Br_{16}O_4$, the cell constants of hypothetical compound, $Y_9Br_{16}O_4$, were obtained. EHTB calculations of $Y_9Br_{16}O_4$ and $Gd_9Br_{16}O_4$ were carried out on the program “YAeHMOP”³⁹.

The valence ionization potentials H_{ii} in eV of different shells⁶⁴ and exponent (ξ)⁶⁵ are listed in Table 3.4.

Table 3.4. Extended Hückel Exponents(ξ), valence shell ionization potential (H_{ii} in eV) and coefficients are listed.

<i>Atom</i>	<i>Orbitals</i>	H_{ii} (eV)	ξ_1^a	ξ_2^a	c_1^b	c_2^b
O	2s	-32.3	2.750			
	2p	-14.8	2.750			
Br	4s	-28.0	2.64			
	4p	-13.9	2.26			
Y	5s	-7.02	1.74			
	5p	-4.40	1.70			
	4d	-6.8	1.40	3.60	0.8316	0.3041
“Gd ⁺⁺⁺ ” ^c	5s	-7.12	1.74			
	5p	-4.40	1.70			
	4d	-7.03884	1.40	3.60	0.8316	0.3041
“Gd ⁺⁺⁺ ” ^c	5s	-6.91	1.74			
	5p	-4.40	1.70			
	4d	-6.56116	1.40	3.60	0.8316	0.3041

^a Slater-type orbital exponents. ^b Coefficients used in double- ξ expansion on Gd⁺ and Gd⁻ are used to model the spin-dependent energies of valence s and d electrons of Gd centers which have the spins that are aligned parallel and antiparallel respecting to the local spin direction of $4f$ electrons.

The plot of density of states (DOS) from the EHTB calculation is shown in Figure 3.11(a). According to the DOS in Figure 3.11(a), the crystal orbital in the region near the Fermi level have mainly Y d orbital character; the green filled area indicates the

contributions of Y 4*d* orbitals. The energy of Fermi level is -6.248065 eV which is indicated with a red dashed line. The two lowest-lying bands (at ~-33 eV and -28eV) are from *s* orbitals of Br and O atoms. At ~ -15 eV, Br 4*p* and O 2*p* bands are overlapping.

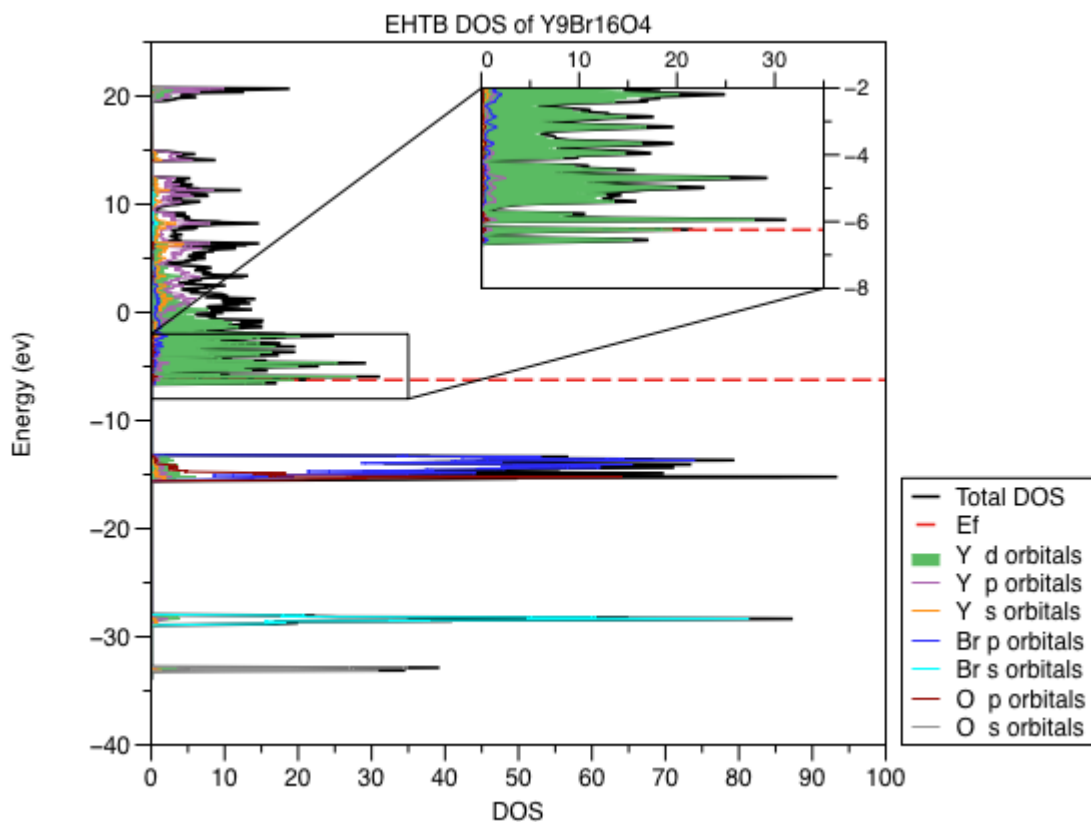


Figure 3.11(a). The partial density of states (PDOS) of $Y_9Br_{16}O_4$ from EHTB calculation. The contributions from different orbitals are labeled with distinct colors. The details near the Fermi level is zoomed in and shown in the box.

About the DOS of EHTB calculation, there were 621 k-points used throughout the Brillouin zone in order to provide a nice mesh. Those 621 k-points were obtained via programming in MATLAB⁶⁶ and evenly dividing the first Brillouin zone^{67, 68} which is shown in Figure 3.11(b). (Γ -Y-T-Z- Γ -X-A₁-Y|T-X₁|X-A-Z|L- Γ). An explicit examination was done for checking the symmetry of 621 k-points in the direct space. The spatial coordinates of each k point need to be converted from the conventional lattice to the primitive lattice via applying a transfer matrix. The weighting values of each k-point are determined through the symmetry operation of the points group.⁶⁷ In the Figure 3.11(b), we can see there are four low-lying, overlapping *d* bands near the Fermi level. The very bottom two *d* band (< -6.5 eV) are fully filled by four electrons. However, the other two *d* bands (> -6.5eV) are half filled by two electrons; the Fermi level cut through the two *d* bands. Therefore, there are total 6 e⁻ available for metal-metal bonding per unit cell (e.g., Y₁₈Br₃₂O₈= (Y⁺³)₁₈(Br⁻)₃₂(O⁻²)₈(e⁻)₆)

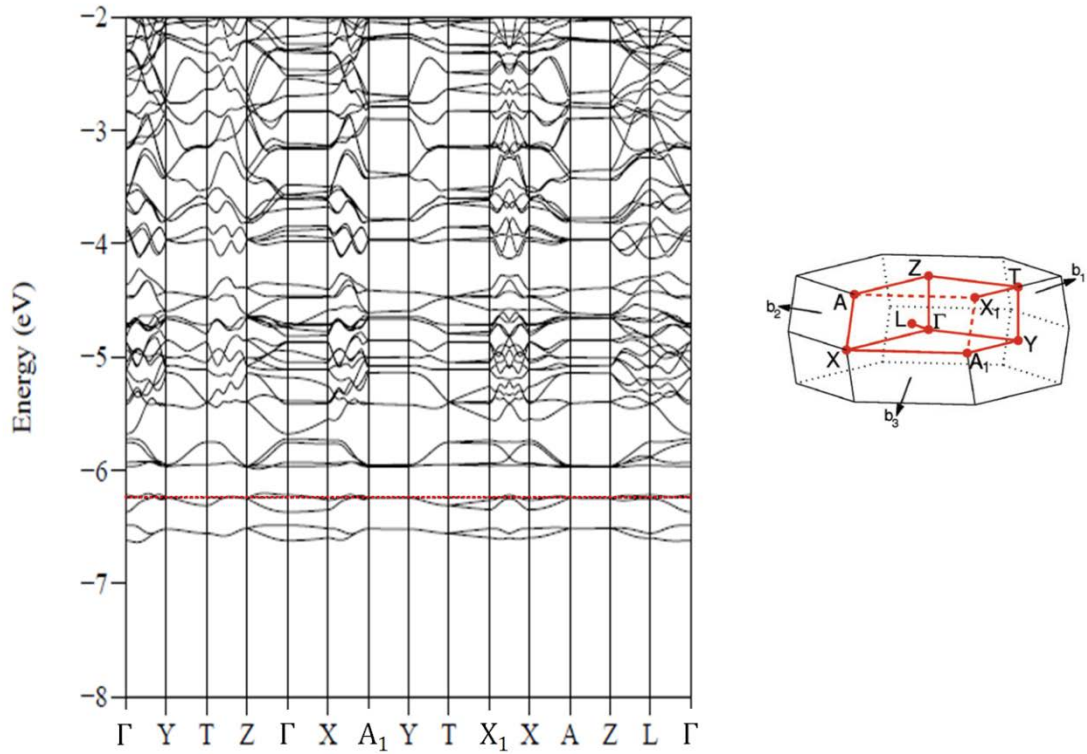


Figure 3.11(b). EHTB calculation. The band structure of $Y_9Br_{16}O_4$ from -2 eV to -8 eV is displayed. The red dashed line indicates the Fermi level (-6.248065 eV). The big polyhedron is shown as the Brillouin zone of face centered orthorhombic lattice and the red polyhedron indicates the first Brillouin zone. The b_1 , b_2 , and b_3 are expressed as the axes in the reciprocal space (Brillouin zone).

The comparisons between the band structure and the DOS of $Y_9Br_{16}O_4$ at the same energy range are seen in Figure 3.11(c). About the band structure of EHTB calculation, fifteen special k points in the Brillouin zone⁶⁸ of face centered Orthorhombic⁶⁹ lattice were chosen as the path (Γ -Y-T-Z- Γ -X-A₁-Y|T-X₁|X-A-Z|L- Γ). Therefore, the bands went through those special points as: Γ -Y-T-Z- Γ -X-A₁-Y|T-X₁|X-A-Z|L- Γ . Usually high symmetric properties were observed at those special points. The formula of the structure in a conventional cell is $Y_{72}Br_{128}O_{32}$, according to the international tables for crystallography⁷⁰. A primitive cell, $Y_{18}Br_{32}O_8$, was used in the calculation in order to save the computational time. Therefore, there are 6 e⁻ available for metal-metal bonding per unit cell (e.g., $Y_{18}Br_{32}O_8 = (Y^{+3})_{18}(Br^-)_{32}(O^{2-})_8(e^-)_6$). At the left in Figure 3.11(c), we can see the Fermi level (red dashed line) cuts through the two *d* bands (< -6.5 eV). At the right in Figure 3.11(c), the zoomed in box indicates the two *d* bands are half filled by two electrons and the Fermi level cuts through the peak of density of states. Of special interest to us is the electronic properties of Gd_2Cl_3 .^{71, 72} The resistivity measurements on Gd_2Cl_3 indicates that it is a semiconductor and the band gap is about 0.85 eV. The results of photoelectron spectrum of Gd_2Cl_3 and band electronic structural calculation are consistent with the resistivity measurements.⁷³ Interestingly, the resistivity measurement on Y_2Cl_3 ⁷⁴ shows essentially the same band gap as Gd_2Cl_3 .

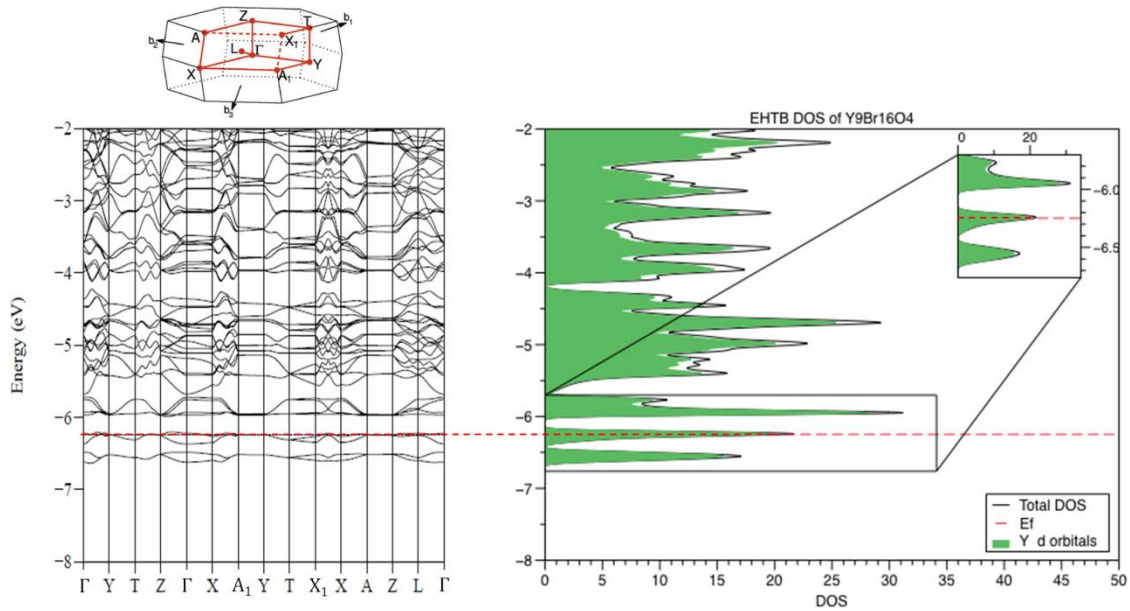


Figure 3.11(c). The band structure from -2 eV to -8 eV and the DOS of $Y_9Br_{16}O_4$ are presented. The red dashed line is Fermi level (-6.248065 eV). The top polyhedron shows the Brillouin zone of face centered orthorhombic lattice.

Based on the similarity between Y_2Cl_3 and Gd_2Cl_3 , the estimated band gap from the EHTB band calculations of $Y_9Br_{16}O_4$ should present a similar result of the real compound $Gd_9Br_{16}O_4$ as seen in Figure 3.12 and Figure 3.13. The difference between two figures is the spins direction which are aligned respectively parallel and antiparallel with the local spin of the seven electrons from $4f$ orbitals.⁷⁵ The d bands from parallel spin-calculations have lower energy than the antiparallel one because orbital energy of a given spin in $5d$ and $6s$ orbitals on a Gd atom with a like-spin $4f^7$ moment are stabilized by $\frac{1}{2}[E(^7D)-E(^9D)]$ ⁶⁵. The parameters of calculations are listed in the front Table 3.4.

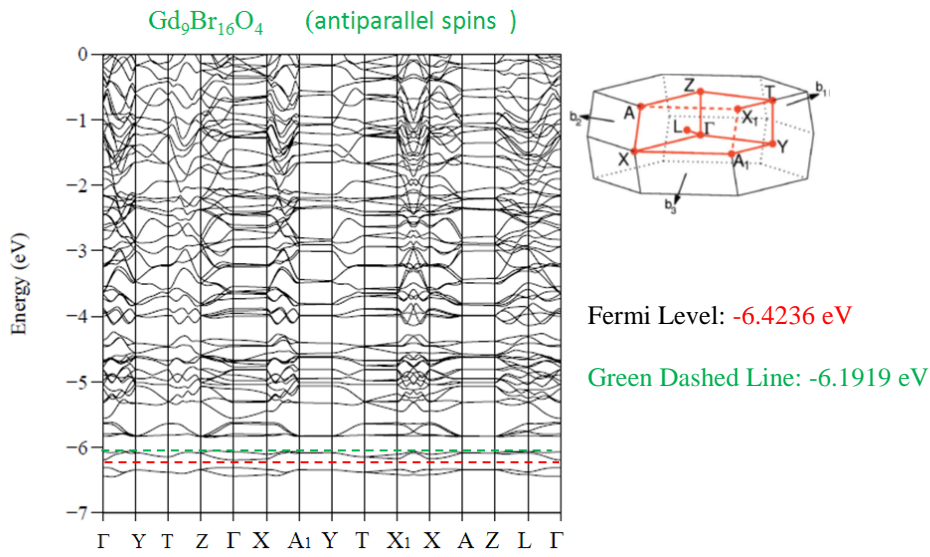


Figure 3.12. The EHTB band calculations of $Gd_9Br_{16}O_4$ with spins that are aligned antiparallel with the local spin direction of the $4f$ electrons. The red dashed line indicates the Fermi level.

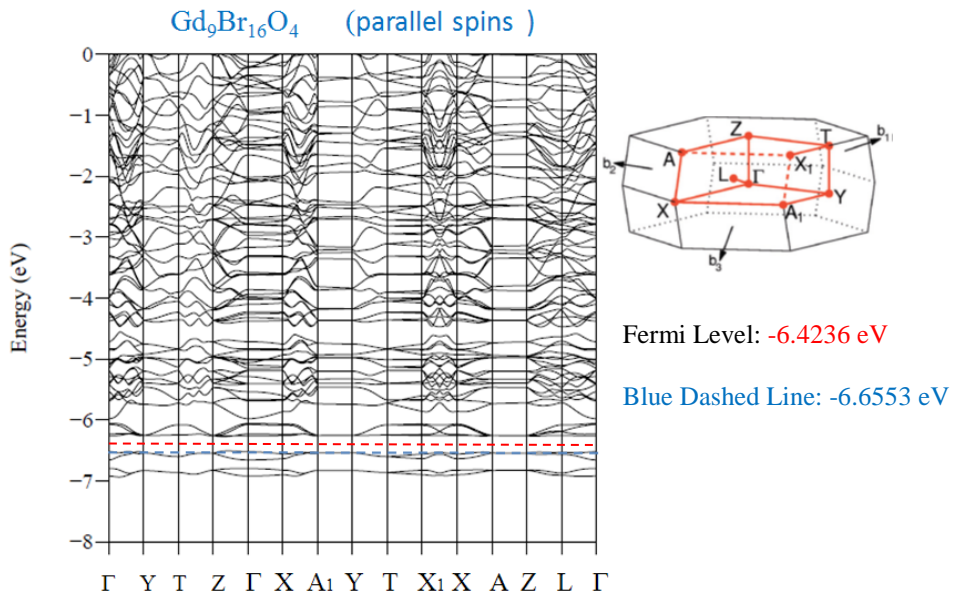


Figure 3.13. The EHTB band calculations of $Gd_9Br_{16}O_4$ with spins that are aligned parallel with the local spin direction of the $4f$ electrons. The red dashed line indicates the Fermi level.

Using the other method, DFT, to calculate the band structure of $Y_9Br_{16}O_4$ is also performed in order to compare the results from both methods. For the DFT calculation, the band calculation was carried out with a mesh of 216 k-points throughout the Brillouin zone in order to get plots of high resolution. The band structure and density of state (DOS) from DFT calculation are shown in Figure 3.14. The black dashed line indicates the scale of zero. The Fermi level is -0.0099459 Ha and equal to -2.706 eV. The unit of energy in the program DMol³ is Hartree. In order to compare the result of EHTB calculations, we need to convert the unit of energy.

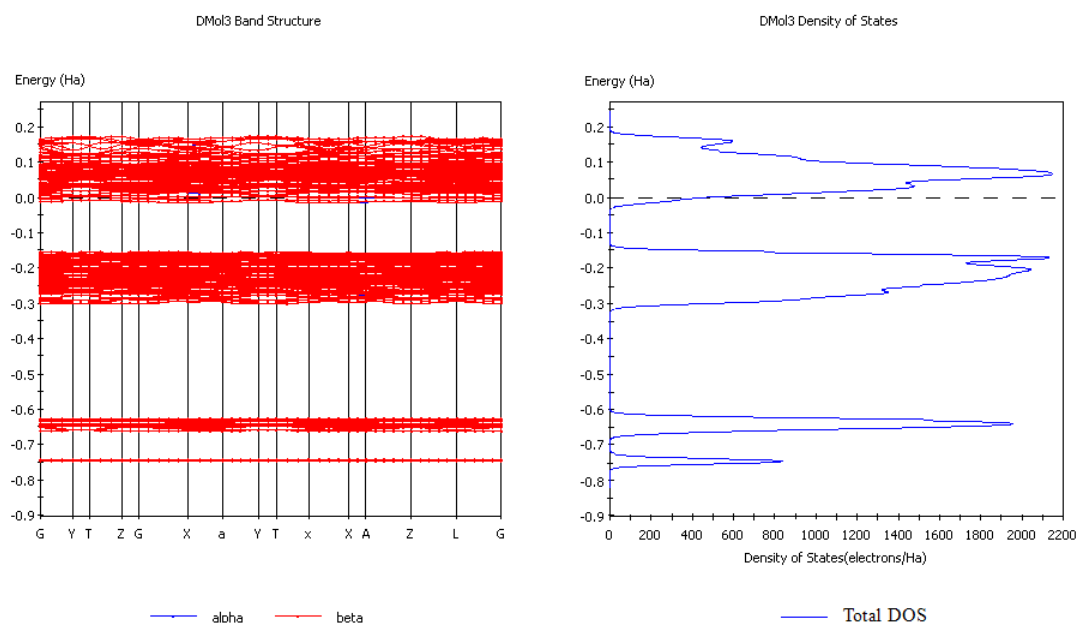


Figure 3.14. The band structure and density of state (DOS) of $Y_9Br_{16}O_4$ from DFT calculation are shown.

DFT and EHTB band structures of $\text{Y}_9\text{Br}_{16}\text{O}_4$ plotted along several symmetry lines in the same Brillouin zone (BZ) are shown in Figure 3.15(a), (b) and (c). The results from DFT and EHTB, the bands near the Fermi level “run” in a similar way. i.e., the consistency between DFT and EHTB treatments is fairly good, at least for the occupied and lowest unoccupied bands. The red dashed lines are indicated the normalized Fermi levels of both methods in order to compare both band structures in the same energy range. Based on the results of both methods, an EHTB scheme where the effects of $4f$ - $5d$ and $4f$ - $6s$ exchange interaction are effectively simulated. The details of the scheme are as following. (i) Using DFT to calculate the electronic structure of a nonmagnetic yttrium analogue of the Gd-containing compound. (ii) Carrying out a calculation on the same yttrium system via using extend Hückel theory, and adjusting the EHTB parameter(H_{ii} and exponents, ξ_s) (iii) Introducing the $4f$ - $5d$ and $4f$ - $6s$ exchanging splitting in the EHTB parameters for the Gd $5d$ and $6s$ orbitals by splitting the H_{ii} parameter of Gd atom as indicated in Table. 3.4. Comparing the EHTB band structure of $\text{Yd}_9\text{Br}_{16}\text{O}_4$ with the band structures of $\text{Gd}_9\text{Br}_{16}\text{O}_4$, EHTB band structures of $\text{Gd}_9\text{Br}_{16}\text{O}_4$ show that the Fermi level shifts from the top of d band into the band gap (Figure 3.13 and Figure 3.12.) which indicates that $\text{Gd}_9\text{Br}_{16}\text{O}_4$ is possible to be a semiconductor. However, a measurement of resistivity is required in order to support this assumption based on the result of the band structure calculation.

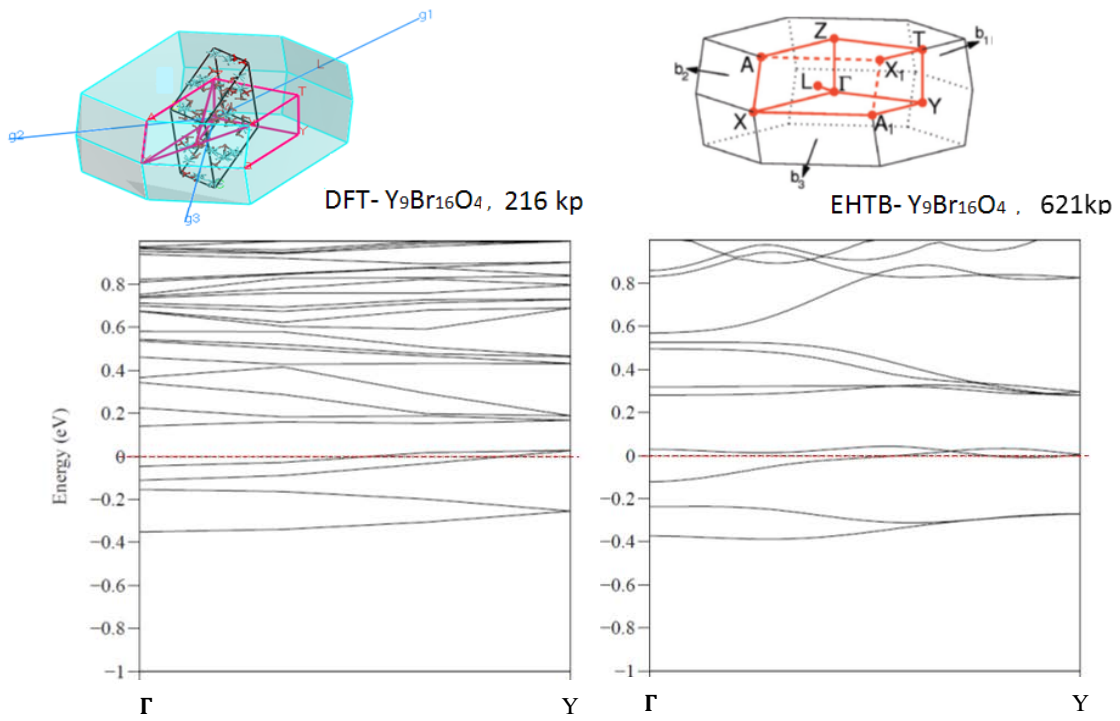


Figure 3.15(a). The calculated dispersion curves for the bands along Γ -Y of the BZ are shown. The left plot is the result from DFT method. The right plot is the result from EHTB method.

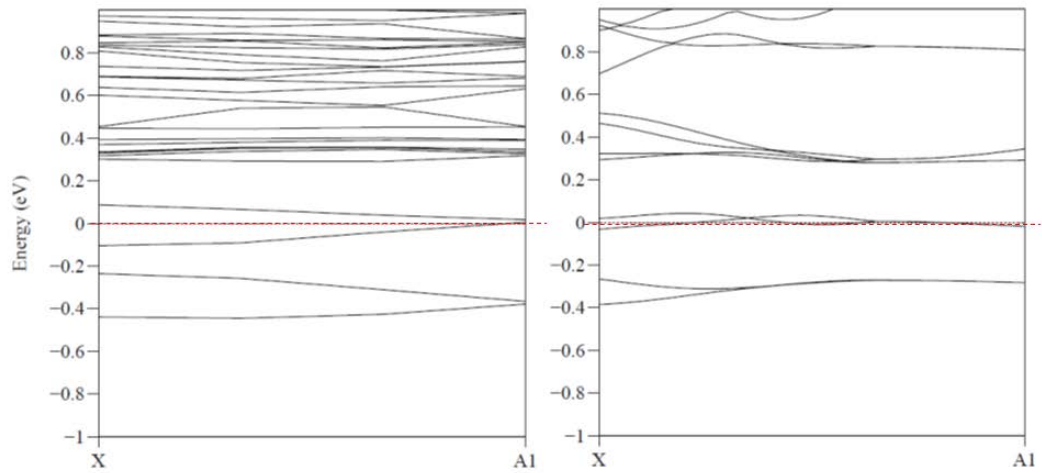


Figure 3.15(b). The calculated dispersion curves for the bands along X-A₁ of the BZ are shown. The left plot is the result from DFT method. The right plot is the result from EHTB method.

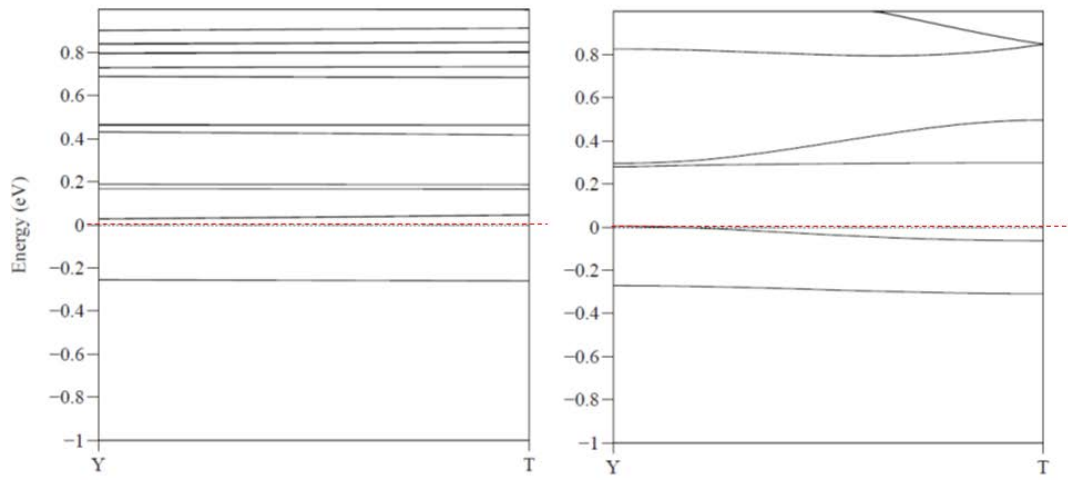
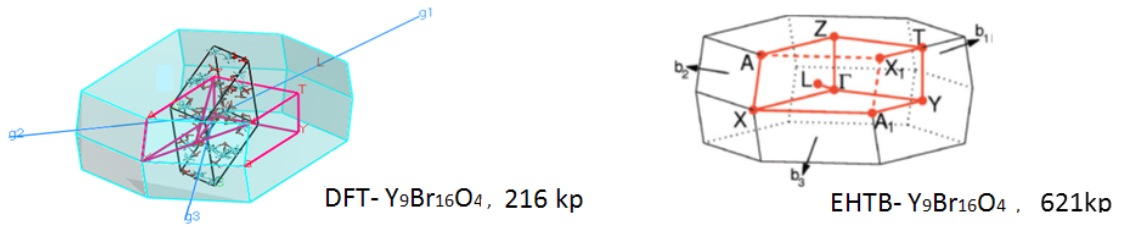


Figure 3.15(c). The calculated dispersion curves for the bands along Y-T of the BZ are shown. The left plot is the result from DFT method. The right plot is the result from EHTB method.

3.7.2. The Electronic Structure of $Gd_6Br_7Si_2$

The electronic structure of model for $Gd_6Br_7Si_2$ was investigated by use of density functional theory (DFT) with the Becke exchange functional and the Lee-Yang-Parr correlation functional (BLYP).^{59, 60} All calculations presented here were performed using the DMol³ program from the Materials Studio suite of programs using the double numerical basis including *d*-polarization functions (DND).⁶¹⁻⁶³ A small frozen-core (1s2s2p3s3p3d), (1s2s2p) and (1s2s2p3s3p) effective potential were used for Gd, Si, and Br respectively. All calculations included scalar relativistic effects and open shell configurations. $Gd_6Br_7Si_2$ can be considered as $(Gd^{+3})_6(Br^-)_7(Si^{-4})_2(e^-)_3$, so there are excess of electrons which fill into Gd *f*, *d*, *s*- based bands. As seen in Figure 3.16, the left plot is the partial density of state (PDOS) of the $Gd_6Br_7Si_2$ and the right one is the PDOS of $Y_6Br_7Si_2$ which serves as a comparison. The difference of two plots is the contribution of *f* orbitals from Gd.

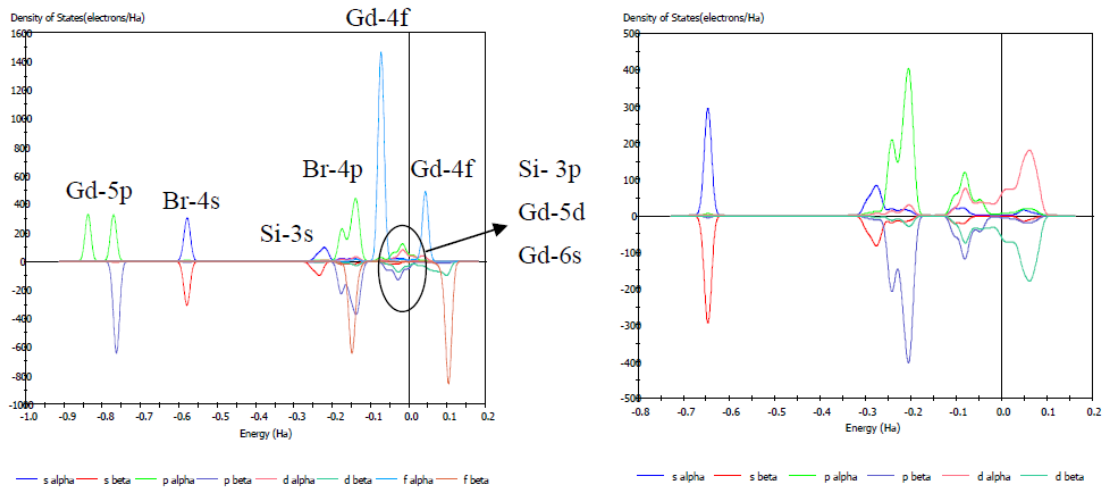


Figure 3.16. (Left) The plot of partial density of state of $Gd_6Br_7Si_2$. (Right) The PDOS of $Y_6Br_7Si_2$.

The electronic band calculations for the nonmagnetic congener, $Y_6Br_7Si_2$, were carried out using a mesh of 9 k-points throughout the Brillouin zone (BZ)⁶⁸ As seen in Figure 3.17, the dashed line indicates the position of Fermi level. The convergence criterion of the energy was set at 10^{-6} a.u. The bottom band of the band structure is from the *s* orbitals of Br. In the middle of the band structure (-0.15 ~ -0.35 Hartree), the contributions are from the *s* orbital of Si and the *p* orbitals of Br. Near the Fermi level, the band is mainly made up by the *5d* orbitals of Gd and *3p* orbitals of Si. The band formed by the *4f* orbitals of Gd is around -0.075 ~ 0.1 Ha. The energy of Fermi level is -0.136353 Ha equal to -3.710 eV.

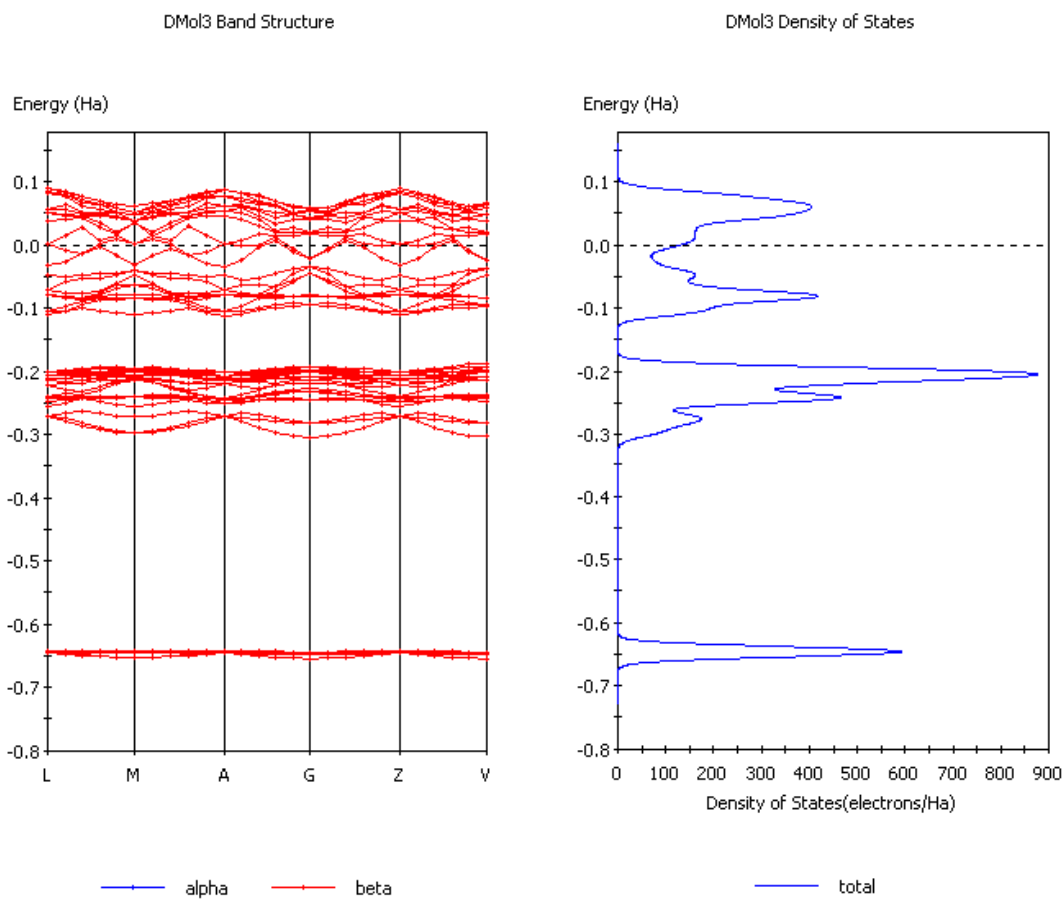


Figure 3.17. (Left) The band structure of $Y_6Br_7Si_2$. (Right) The total DOS of $Y_6Br_7Si_2$.

3.8 Result and Discussion

3.8.1 Compound I: $Gd_9Br_{16}O_4$

Solid state materials can be categorized into four groups: insulators, semiconductors, conductors and superconductors. They are classified based on the conductivity and their energy band gap. The conductivity of insulators is smaller than $10^{-8} S/cm$ and the energy band gap of insulators is larger than 9 eV. The conductivity of semiconductors is at the range from $10^{-8} S/cm$ to $10^3 S/cm$ and the energy gap of semiconductors is about 1 eV. (The energy band gap of silicon is 1.1 eV which is a mid-range value⁷⁶). The conductivity of conductor is larger than $10^3 S/cm$. According to the literature; Gd_2Cl_3 ⁷² and Y_2Cl_3 ⁷⁴ have similar band gaps about 0.85 eV which are consistent with the resistivity measurements. Hence, we infer that using a hypothetical nonmagnetic yttrium analogous ($Y_9Br_{16}O_4$) to run calculations should have similar result as $Gd_9Br_{16}O_4$. The EHTB band structure calculations on real compound, $Gd_9Br_{16}O_4$, and $Y_9Br_{16}O_4$ show that there are four low-lying, overlapping d bands near the Fermi level on both band structures. The very bottom two d bands are fully filled by four electrons. The other two d bands are half filled by two electrons; the Fermi level cut through the two d bands. The models of d electrons of Gd centers with spins that are aligned antiparallel or parallel with the local spin direction of the $4f$ electrons respectively demonstrate that orbital energies of a given spin in $5d$ and $6s$ orbitals on a Gd atom with a like-spin $4f^7$ moment are more stable.

3.8.2 Compound II: $Gd_6Br_7Si_2$

The first examples of reduced rare earth halides containing second-row non-metal interstitial atoms were Gd_4I_5Si and Gd_3I_3Si ⁷⁷ having iso-structures with Y_4I_5C ¹⁹ and Gd_3Cl_3C ¹². Both structures are built by edge-sharing gadolinium octahedra with centered silicon to form one-dimensional chains and a three-dimensional network. Similarly, Gd_4Br_6S ^{17, 18} has chains structure and is isotopic with Tb_4SiBr_6 , Gd_4CBr_6 and Sc_4CCl_6 .⁷⁸ A lot of metal rich halides MX_nA ($n \leq 2$, $A = H, C, N, O$, $X = \text{Halogen}$) have been published.^{78, 79} However, Gd_4I_5Si , Gd_3I_3Si and Gd_4Br_6Si are the only known compounds with silicon as interstitial atom until now. The other metal halide compounds containing Si so far are $MISi$ ($M = La, Ce, Pr$) and $La_4I_3Si_4$ ⁸⁰ which involve Si-Si bonding and are different from the isolated Si atom sitting at the center of Gd_6 octahedra. $Gd_6Br_7Si_2$ is a special compound which has a two dimensional structure and contains two types of interstitial atoms (Si, Br). We believe that there is a stacking fault within the layers which may explain the problem of Si/Br disorder problem. Attempting to find a direct evidence from the arrangement of crystal diffraction reflections and find an appropriate enlarge unit cell to explain the possible permutation of the layers has not been completed.

4. PRASEODYMIUM LAYER COMPOUNDS

4.1. Synthesis

III. Pr_3Si was obtained as a minor by-product in a reaction intended to prepare the target compound, $\text{Pr}_6\text{I}_7\text{Si}_2$. The stoichiometric mixing of the starting materials PrI_3 ⁸¹ (prepared from HgI_2 and Pr, purified by three subsequent sublimations), praseodymium (small pieces), and silicon (Aldrich; powder; -60 mesh; purity 99.999%; handled under argon) in a niobium tube was designed to synthesize $\text{Pr}_6\text{I}_7\text{Si}_2$. The reaction was heated at 995~1000 °C in a sealed niobium tube for 2 weeks. Black tiny rectangular crystals are recognized as Pr_3Si . All crystals are sensitive to moisture and air.

IV. $\text{Pr}_2\text{I}_2\text{Ge}$ was obtained in a reaction intended to prepare the target compound, $\text{Pr}_6\text{I}_7\text{Ge}_2$. It was synthesized by the stoichiometric mixing of the starting materials PrI_3 (prepared from HgI_2 and Pr), praseodymium (small pieces), and germanium in a niobium tube. The reaction was heated at 1000 °C for 2 weeks. The mixing procedure was carried out in a glove box under N_2 atmosphere. Black tiny rectangular crystals are obtained. The compound is sensitive to moisture and air.

4.2. Single-Crystal X-ray Diffraction

Black crystals of dimensions $0.036 \times 0.020 \times 0.030 \text{ mm}^3$ for 1 and $0.025 \times 0.050 \times 0.020 \text{ mm}^3$ for 2 were selected for indexing and data collecting on a Bruker APEX II diffractometer at low temperature (110 K). The program TWINABS⁸² and CELL_NOW⁸³ were applied for doing absorption correction and analyzing twinned domains. The structures were solved by the procedure⁸⁴ of treating non-merohedrally twinned crystal data plus the direct methods and difference Fourier syntheses. The final cycles of least-squares refinement including atomic coordinates and anisotropic thermal parameters for all atoms were converged. There were residual electron densities in the final difference map which are close to heavy atoms Pr(1) in III and close to heavy atoms Pr(1) in IV. Use the SHELXTL version 6.12 software package⁴⁸ to perform all structure refinements. The selected bond lengths of d(Si-Pr) and d(Ge-Pr) in Pr₃Si and Pr₂I₂Ge are listed in Table 4.1. Atomic coordinates and displacement parameters are presented in Table 4.2(a) and (b). The crystallographic data for III and IV are shown in Table 4.3.

Table 4.1. Selected bond lengths [\AA] for Pr_3Si and $\text{Pr}_2\text{I}_2\text{Ge}$

d (Si-Pr)	\AA	d(Ge-Pr)	\AA	d(Ge-Pr)	\AA
Si(2)-Pr(1)#1	2.930(1)	Ge(1)#1-Pr(1)	3.0110(6)	Ge(1)-Pr(1)#5	3.0110(6)
Si(1)-Gd(1)#9	2.930(1)	Ge(1)#2-Pr(1)	3.0110(6)	Ge(1)-Pr(1)#6	3.0110(6)
Si(1)-Gd(1)#8	2.930(1))	Ge(1)-Pr(1)#3	3.0110(6)	Ge(1)-Pr(1)#7	3.0110(6)
Si(1)-Gd(3)#6,7	2.930(1)	Ge(1)-Pr(1)#4	3.0110(6)		

The Symmetry transformations used to generate equivalent atoms for Pr_3Si :

#1 $x+0, -y+1, -z+3/2$ #2 $-z+1, x, y+1/2$ #3 $-y+1/2, z-1/2, x+1$
#4 $y, z-1/2, -x+1$ #5 $z-1, -x+1/2, y+1/2$ #6 $-z+1, x+1/2, -y+3/2$
#7 $z-1/2, x+1/2, y+1/2$ #8 $y-1/2, -z+3/2, -x+1$ #9 $-y+1/2, z+0, -x+1$

The Symmetry transformations used to generate equivalent atoms for $\text{Pr}_2\text{I}_2\text{Ge}$:

#1 $x-1, y, z$ #2 $x-1, y-1, z$ #3 $x+1, y+1, z$ #4 $x+1, y, z$
#5 $-x+1, -y+2, -z$ #6 $-x+1, -y+1, -z$ #7 $-x+2, -y+2, -z$

Table 4.2(a). Atomic coordinates and equivalent isotropic displacement parameters ($\text{\AA}^2 \times 10^3$) for Pr_3Si . $U(\text{eq})$ is defined as one third of the trace of the orthogonalized U^{ij} tensor.

	x	y	z	$U(\text{eq})$
Pr(1)	0.1250	0.3877(1)	0.8623(1)	9(1)
Si(2)	0.1250	0.6250	0.8750	46(6)

Table 4.2(b). Atomic coordinates and equivalent isotropic displacement parameters ($\text{\AA}^2 \times 10^3$) for $\text{Pr}_2\text{I}_2\text{Ge}$. $U(\text{eq})$ is defined as one third of the trace of the orthogonalized U^{ij} tensor.

	x	y	z	$U(\text{eq})$
Pr(1)	0.3333	0.6667	0.515(1)	10(1)
I(1)	-0.3333	0.3333	0.1149(1)	10(1)
Ge(1)	1.0000	1.0000	0	7(1)

Table 4.3. Crystal data and structure refinement for Pr₃Si (III) and Pr₂I₂Ge (IV)

Identification code	Pr ₃ Si	Pr ₂ I ₂ Ge
Empirical formula	Pr ₃ Si	Pr ₂ I ₂ Ge
Formula weight	450.82	608.21
Temperature	110(2) K	110(2) K
Wavelength	0.71073 Å	0.71073 Å
Crystal system	Cubic	Trigonal
Space group	<i>Ia</i> $\bar{3}$ <i>d</i>	<i>R</i> $\bar{3}$ <i>m</i>
Unit cell dimensions	a = 12.328(1) Å b = 12.328(1) Å c = 12.328(1) Å	a = 4.3603(5) Å b = 4.3603(5) Å c = 32.063(5) Å $\alpha=\beta=90^\circ$ $\gamma=120^\circ$.
Volume (Å ³)	1873.6(3)	527.9(1)
Z	16	3
Crystal size (mm ³)	0.036 x 0.020 x 0.030	0.025 x 0.050 x 0.020
Refinement method	least-squares on F ²	least-squares on F ²
Goodness-of-fit on F ²	1.411	1.232
Final R indices [I>2sigma(I)]	R1 = 0.0421 wR2 = 0.0755	R1 = 0.0664, wR2 = 0.01984
Absorption correction	SADABS	TWINABS
Min. and max. transmission	0.7991/0.9631	0.351560/ 0.748661
Largest diff. peak and hole (e.Å ⁻³)	2.641 and -2.233	5.004 and -5.007

Weight = 1 / [sigma²(Fo²) + (0.0000 * P)² + 652.84 * P], where P = (Max (Fo², 0) + 2 * Fc²) / 3 for **(III)**

Weight = 1 / [sigma²(Fo²) + (0.0526 * P)² + 298.14 * P] where P = (Max (Fo², 0) + 2 * Fc²) / 3 for **(IV)**

4.3. Powder X-ray Diffraction

4.3.1. The X-ray Powder Pattern of Pr_3Si

Figure 4.1(a) is the result of characterizing Pr_3Si phase from TOPAS program. Since the crystal structure is refined by the data of single-crystal X-ray diffraction, the purpose of using TOPAS program on Pr_3Si is to verify the existence of target phase in the powder sample and do the quantitative phase analysis. The green peak is the calculated powder pattern of Pr_3Si from the single-crystal X-ray data. The read fitting curves include three calculated powder patterns of three phases: Pr_3Si , PrOI and Silicon as a standard. From the match between the experimental powder pattern (blue peaks) and green peaks, it shows the existence of Pr_3Si . This experimental powder pattern can only provide the qualitative analysis to verify the phase of Pr_3Si , and it can not apply to quantitative analysis due to containing some unclassified peaks. The sample was handled in a glove box filled with N_2 . The sample container for PXRD measurement is specially designed, and a thin film is covered on the top of sample in order to prevent the sample from exposing in air. However, the thin film would cause the background at low angle, as seen a little hill at the beginning of the powder pattern.

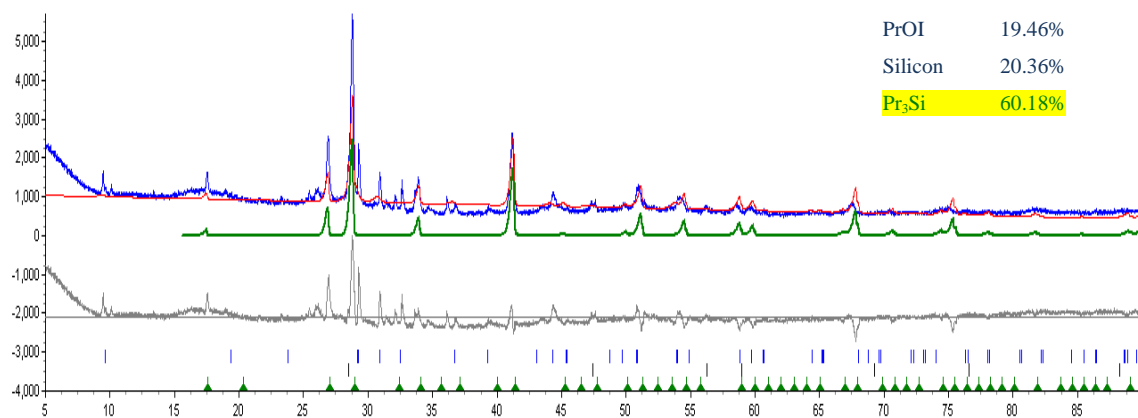


Figure 4.1(a) The result of characterizing Pr_3Si phase from TOPAS program. The blue curves are the experimental PXRD pattern. The green peaks are the cal. PXRD pattern of Pr_3Si . The red pattern is the fitting curves of three phases.

4.3.2. The X-ray Powder Pattern of Pr₂I₂Ge

Figure 4.1(b) is the result of characterizing Pr₂I₂Ge phase via using TOPAS program. Since the crystal structure is refined by the data of single-crystal X-ray diffraction, the purpose of the using TOPAS program is to verify the existence of target phase in the powder sample and do the quantitative phase analysis. The green peak is the calculated powder pattern of Pr₂I₂Ge from the sing-crystal X-ray data. The read fitting curves include three calculated powder patterns of three phases: Pr₂I₂Ge, PrOI and Silicon as a standard. From the match between the experimental powder pattern (blue peaks) and green peaks, it shows the existence of Pr₂I₂Ge. This experimental powder pattern can only provide the qualitative analysis to verify the phase of Pr₂I₂Ge, and it can not apply to quantitative analysis due to containing some unclassified peaks and bad profile of peaks at the 2θ equal to 27°. The sample was handled in a glove box filled with N₂ atmosphere. The sample container for PXRD measurement is specially designed, and a thin film is covered on the top of sample in order to prevent the sample from exposing in air. However, the thin film would cause the background at low angle, as seen a little hill at the begging of the powder pattern.

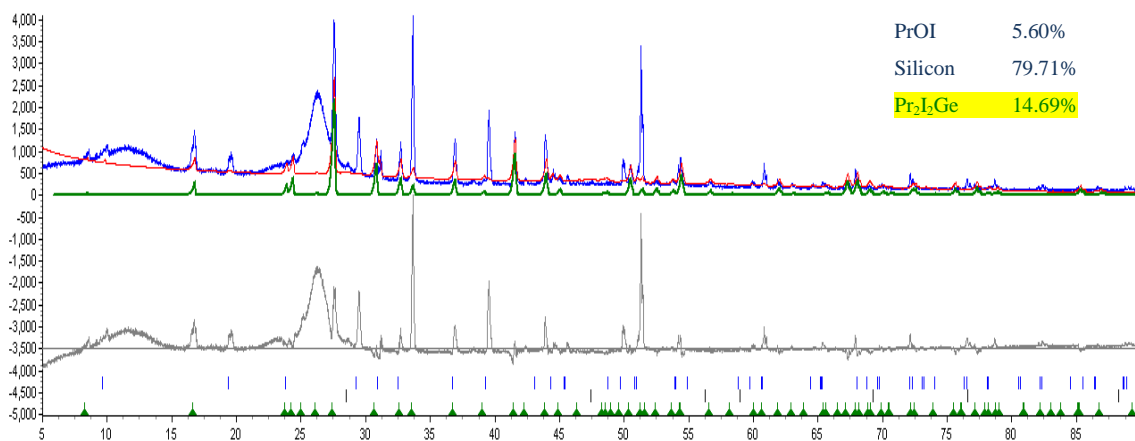


Figure 4.1(b). The result of characterizing Pr₂I₂Ge phase from TOPAS program. The blue curves are the experimental PXRD pattern. The green peaks are the cal. PXRD pattern of Pr₂I₂Ge. The red pattern is the fitting curves of three phases.

4.4 Crystal Structures

4.4.1. The Structure of Pr_3Si

The binary phase diagram of Pr-Si has been reported by Eremenko⁸⁵ et al in 1986. Not included among the ten known binary phases in Pr-Si system⁸⁶⁻⁹⁴, is the new binary Pr_3Si reported in this work. The space group of Pr_3Si is $Ia\bar{3}d$ and the structure is, of course, highly symmetric. One depiction of the structure is shown in a [111] projection in Figure 4.2.

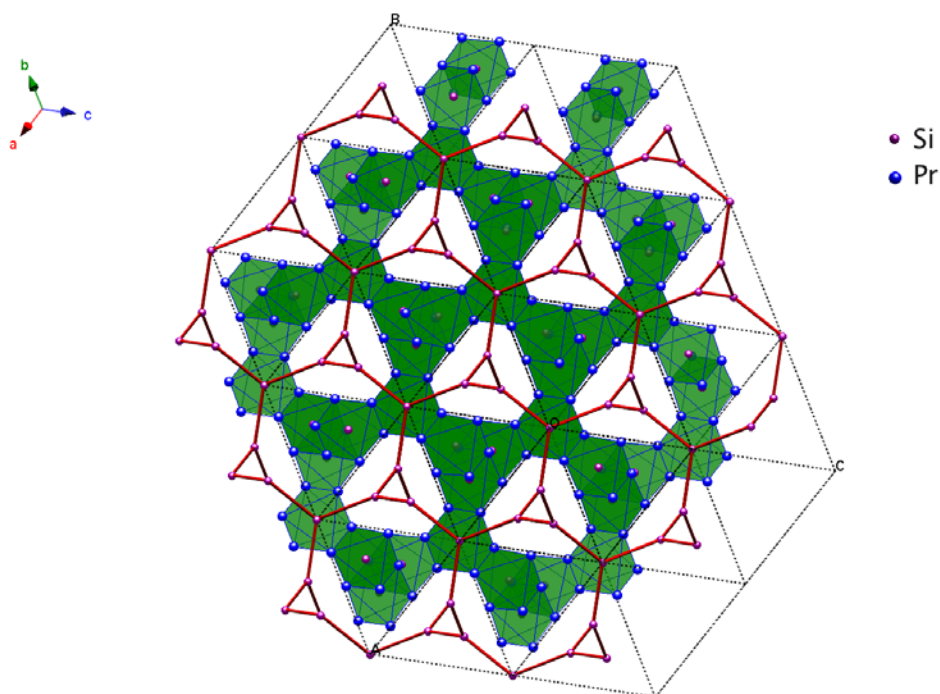


Figure 4.2. View a 3-D structure of Pr_3Si along [111]. The red net is a (10, 3)-a silicon network.

The structure is constructed by Pr-Pr edge-sharing Pr_6Si building units as seen in Figure 4.3(a). In Figure 4.3(a), the structure is slightly tilted a little bit in order to illustrate the stacking in the network. Also, the green polyhedral present Pr_6Si octahedra and the blue/purple circles are Pr/Si atoms.

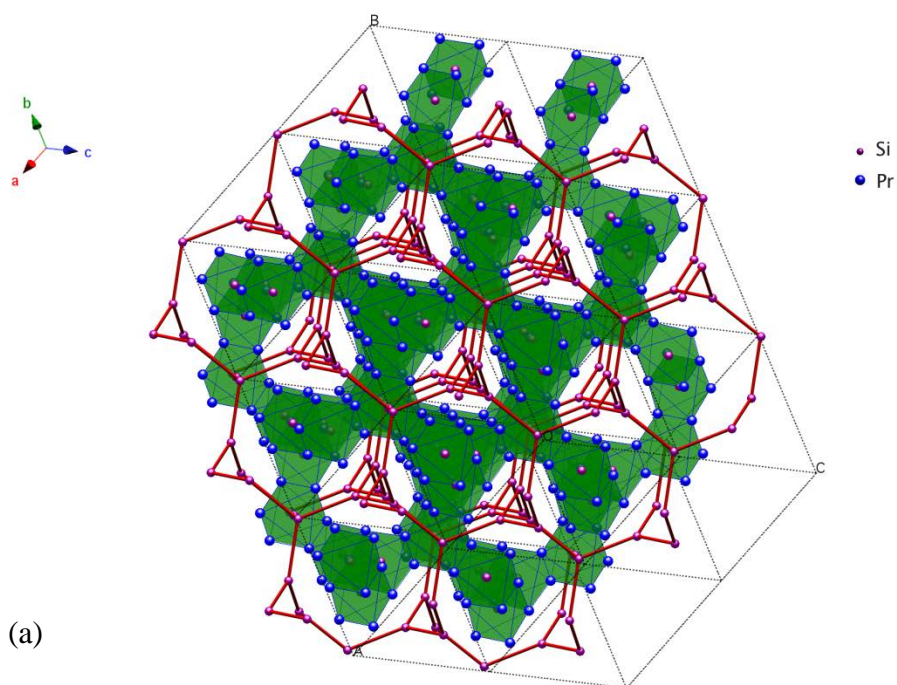


Figure 4.3(a). Tilt the structure to view the stacking of polyhedra and the helix chains of red silicon networks.

Selecting one of the octahedra from the structure displays a silicon atom sitting at the centre of Pr_6 octahedron as seen in Figure 4.3(b). There are four different bond lengths within the octahedra. In Figure 4.3(c), the symbol ‘d1’ presents Si-Pr bonds and

the bond length is 2.923 Å. The other three types of bonds, ‘d2’, ‘d3’ and ‘d4’ are Pr-Pr metal bonds. The bond lengths of metal bonds are distinct from the positions of connection in the structure. The shortest metal bonds, d2(Pr-Pr) equal to 3.907 Å, share bonding with neighboring octahedron. Longer bonds, d3(Pr-Pr) equal to 4.140 Å, are the metal bonds at the edges of octahedron without sharing bonds. The longest bonds are d4(Pr-Pr) equal to 4.243 Å which are the bonds to form the top and bottom trigon faces of an anti-trigonal prism within a octahedron.

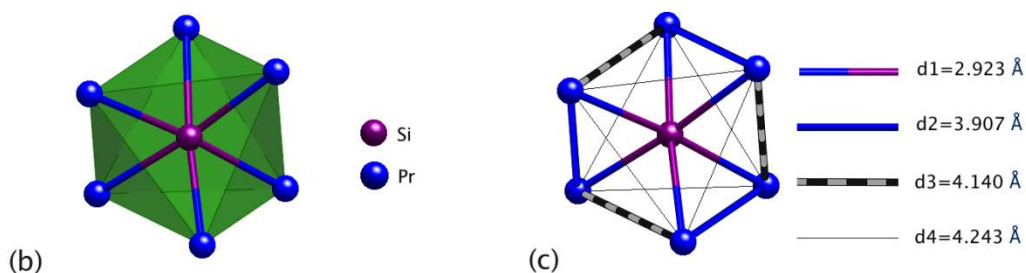


Figure 4.3(b). A single octahedron shows the connections between the interstitial silicon atom and Pr atoms. **(c)** There are four distinct bond lengths labeled with different bond symbols in a single octahedron.

The interstitial Si atoms can artificially compose (10, 3)-a-nets topology via connecting the silicon atoms that helps us understanding the structure of Pr₃Si, because each silicon atom presents a unit of octahedra. The (10, 3)-a net is a typical and frequent net of two 3-connecting nodes and it is described as a SrSi₂ (SrS) net, which is also

observed in the solid state compounds.⁹⁵⁻⁹⁷ In SrSi_2 , of course, Si-Si contacts are indicative of Si-Si single bonds. In what follows, we show Si-based nets for the purpose of explaining the Pr_3Si structural topology; there is no significant Si-Si bonding.

There are two symmetry-related (10, 3)-a nets are revealed in Pr_3Si . As Figure 4.4(a) shows, the green and red nets present the interpenetration of two symmetry-related silicon nets. Through viewing the three-membered net in a unit cell in Figure 4.4(b), the three-membered helices in the green net are right-handed (D) and those in the red net are left-handed (L). Select two different single three-membered helices to get a clear view in Figure 4.4(c). (10, 3)-a nets in a [010] projection is shown in Figure 4.4(d).

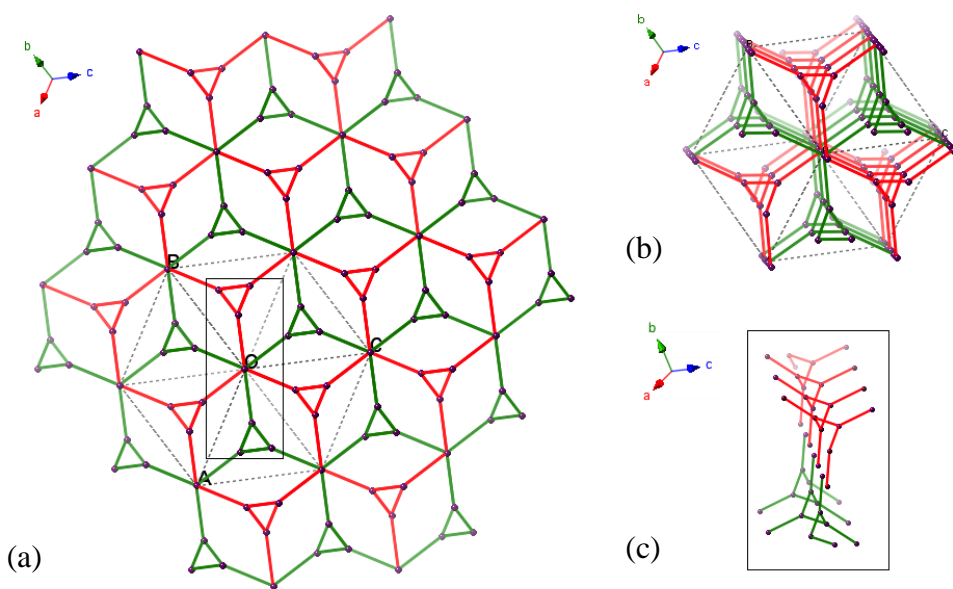


Figure 4.4(a). Two symmetry relative (10, 3)-a nets are labelled red and green. **(b)** Select the unit cell to see the directions of two helices. **(c)** Zoom in the rectangular box to recognize that the red net is the right-handed helix chain and the green net is the left-handed helix chain.

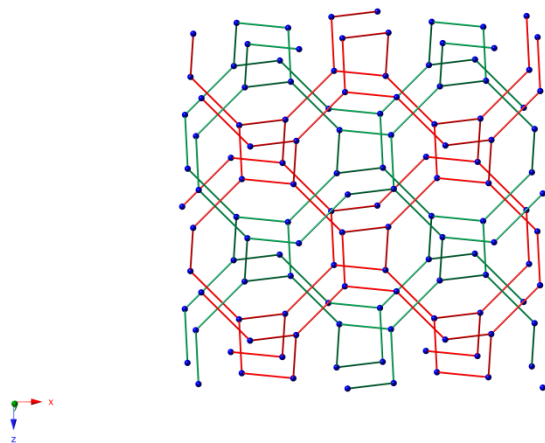


Figure 4.4 (d). (10, 3)-a nets are shown in a [010] projection.

The combination of two (10, 3)-a nets makes Pr_3Si a racemic binary. According to the summary of Wells⁹⁸, there are seven known uniform (10, 3) nets. In the configuration of (10, 3)-a net, all Si-Si interatomic distances are equal and all interbond angles are 120° and there is one 3_1 , three-fold screw axis, in each three-membered helices; in other word, a 3_2 axis is centred by the three-membered helices. Wells also predicted two possible interpenetrating nets which are formed by two identical (10, 3)-a nets: (i) two D-(10, 3)-a nets and (ii) D and L forms of (10, 3)-a nets. The second type of interpenetrating nets had been unknown until a molecule-based material of formula with D and L forms of interpenetrating nets is reported by Janiak and Sanchiz groups in 2010.⁹⁹ The second type of interpenetrating polyhedra nets was in this compound. It is not common in the solid state compounds to have two (10, 3)-a net and two nets have interpenetrating relationship. Pr_3Si is a rare compound with a high symmetric geometry.

4.4.2. The Structure of $\text{Pr}_2\text{I}_2\text{Ge}$

The structure of $\text{Pr}_2\text{I}_2\text{Ge}$ is a closed-packing layer structure, as seen in Figure 4.5. Each layer is constructed by Pr_6 octahedra and separated by iodine atoms. The interstitial atoms centered in the green Pr_6 octahedral are Ge (1) atoms which occupy the special positions: (0, 0, 0) (see Table 4.2.). The bond lengths between Pr atom and interstitial Ge(1) atom is 3.0116 Å.

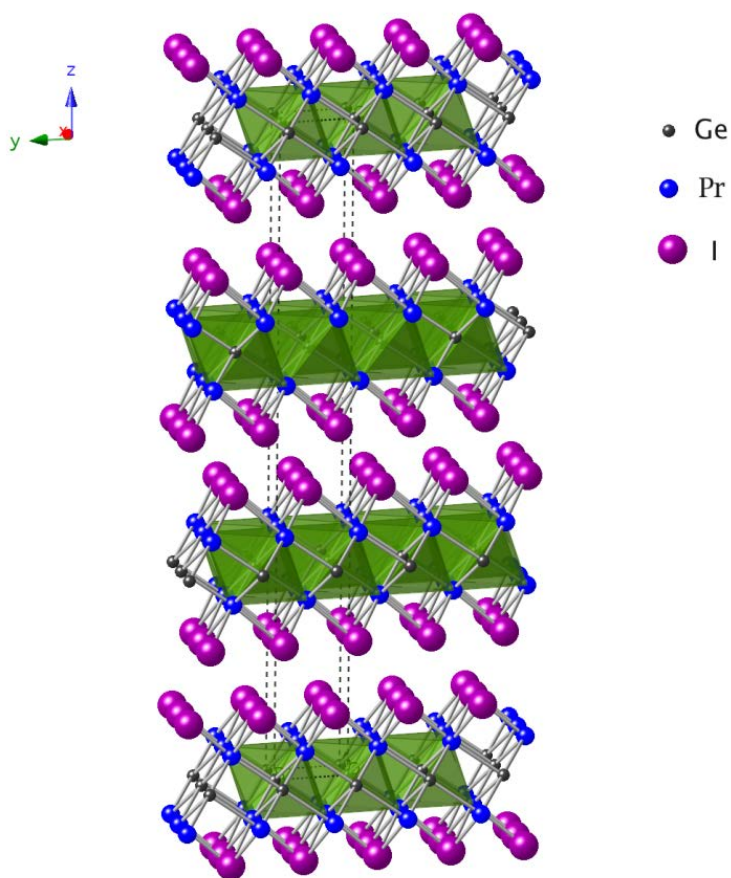


Figure 4.5. The closed packed layers are separated by iodine atoms. Black dash line is presented a unit cell.

Select one layer and delete iodine atoms to get a close look on the connections of each octahedron in Figure 4.6. For each octahedron, there are six edges are sharing with neighboring octahedron to form a layer and the connection of each octahedra is extend along the 'x' and 'y' axis.

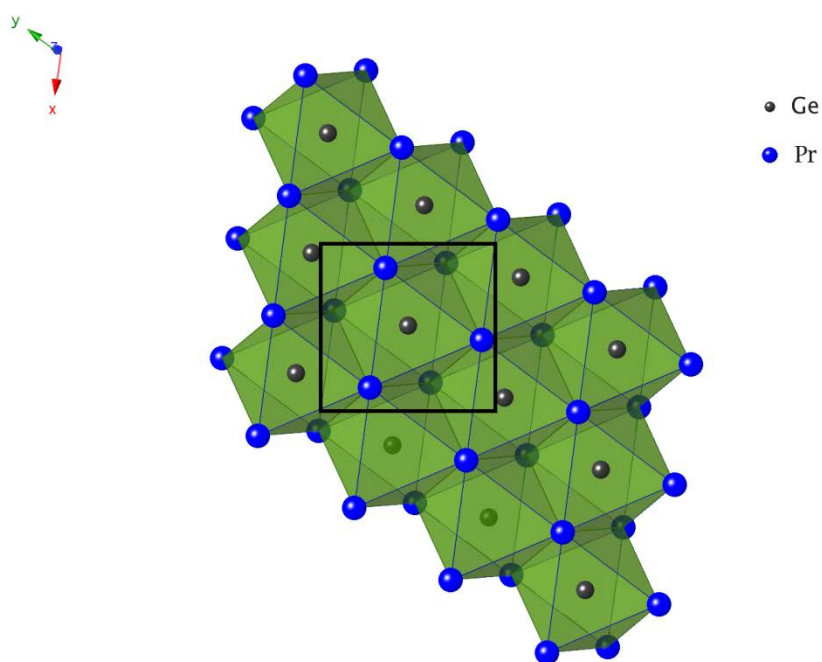


Figure 4.6. The layer of $\text{Pr}_2\text{I}_2\text{Ge}$ without showing iodine atoms. The black box specifies one octahedron which is connected to the neighboring octahedra via sharing six edges. The honeycomb closed packing of octahedra is seen in this Figure as well.

Then, put iodine atoms back to the structure and each iodine atom is filled in the tetrahedral sites above and below each layer as seen in Figure 4.7. Each iodine atom forms three bonds to connect with praseodymium atoms.

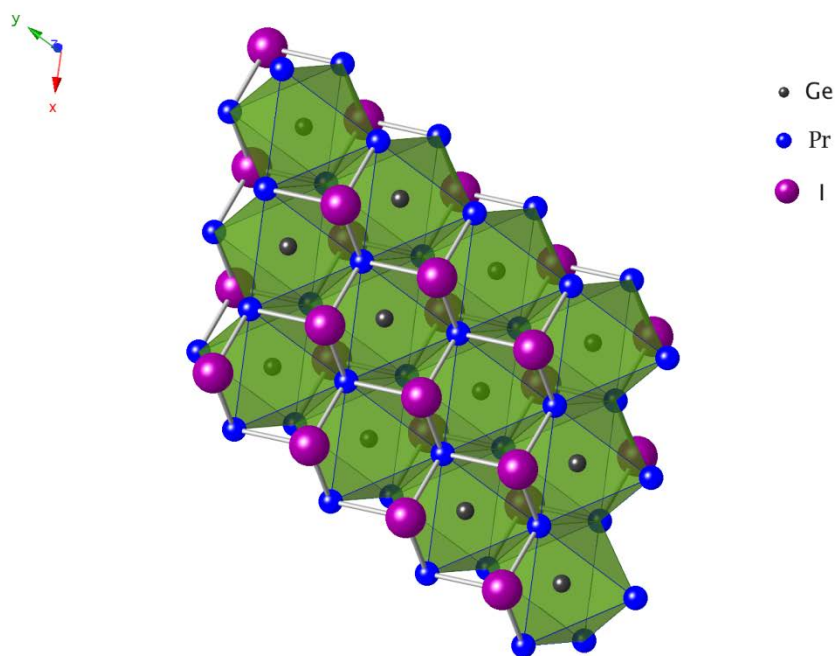


Figure 4.7. The layer of $\text{Pr}_2\text{I}_2\text{Ge}$ is shown. Each tetrahedral site is filled by an iodine atom.

If select one octahedron from the layer (Figure 4.6.) and zoom in as seen in Figure 4.8. There are two distinct metal-metal bond lengths in each octahedron. The shorter bonds are edge-sharing bonds equal to 4.155 Å. The longer bonds are the bonds without sharing edge equal to 4.360 Å.

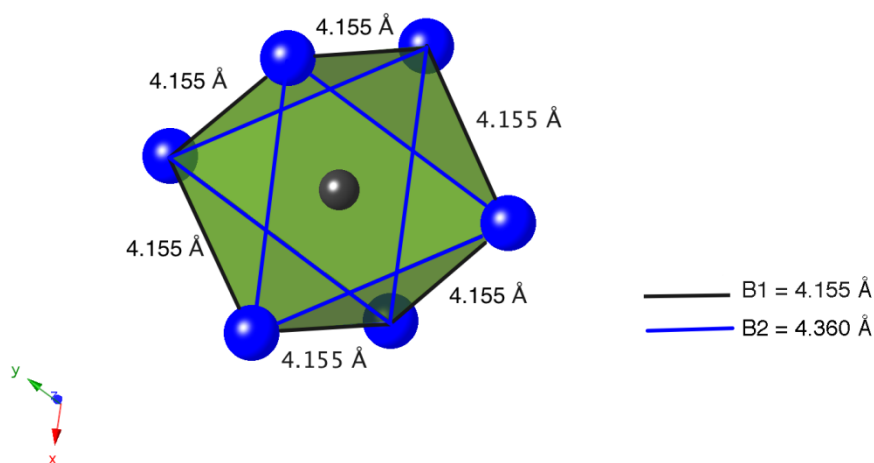


Figure 4.8. The building block of $\text{Pr}_2\text{I}_2\text{Ge}$ is shown. Two distinct bond lengths in each octahedron are indicated in this Figure.

4.5 Calculated Electronic Structure of Pr_3Si

The electronic structure of model for Pr_3Si was investigated by use of extended Hückle tight bonding theory (EHTB). The plot of density of state (DOS) is shown in Figure 4.9(a) and the band structure of Pr_3Si is in Figure 4.9(b). As expected, Pr_3Si turns out to be metallic based on the result of band structure. According to the DOS in Figure

4.9(a), it points out that the region around the Fermi level is made up mainly from the d orbital of Pr atoms. The energy of Fermi level is -9.308356 eV.

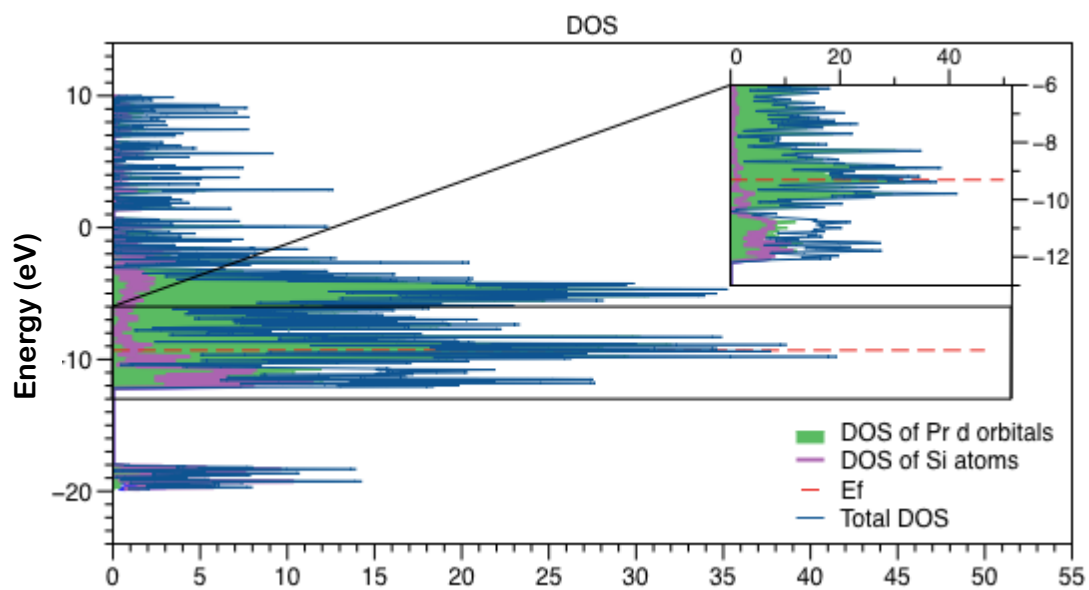


Figure 4.9(a). DOS of Pr₃Si. The selected area from -6 eV to -13 eV near the Fermi level is zoomed in to see the DOS contribution from each components

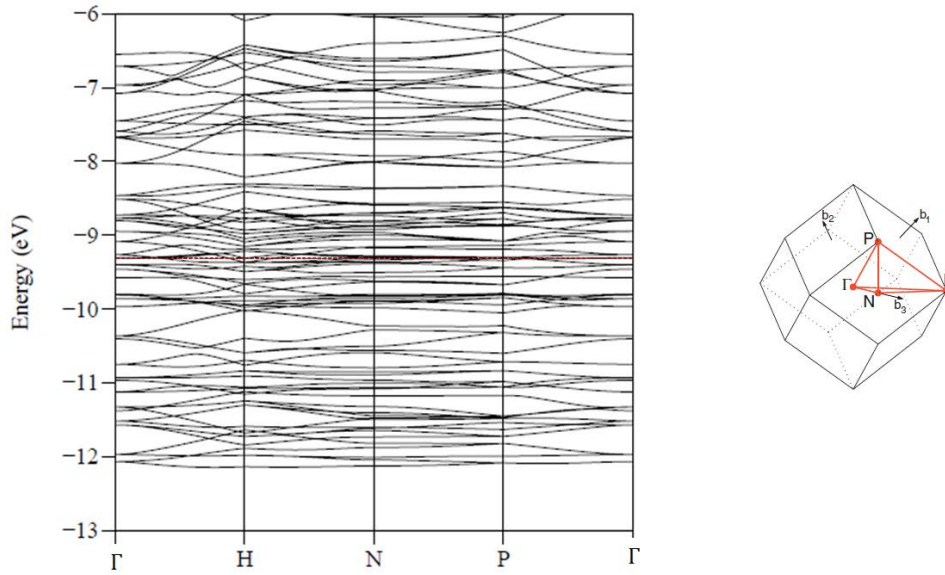


Figure 4.9(b). The band structure of Pr_3Si . The red dashed line indicates the Fermi level (-9.308356 eV.). The dodecahedron describes the Brillouin zone of body center cubic lattice. The path of special points: Γ -H-N-P- Γ is used in the band structure calculation.

The comparisons between the band structure and the DOS of Pr_3Si at the same energy range are seen in Figure 4.9(c). For the calculation of band structure, four special k points in the Brillouin zone⁶⁸ of body center cubic lattice were chosen as the path. Therefore, the bands went through the special points as: Γ -H-N-P- Γ . Usually high symmetric properties were observed at those special points. The formula of the structure in a conventional cell is $\text{Pr}_{48}\text{Si}_{16}$, according to the international table for crystallography.⁷⁰ A primitive cell, $\text{Pr}_{24}\text{Si}_8$, was used in the calculation in order to save the computational cost.

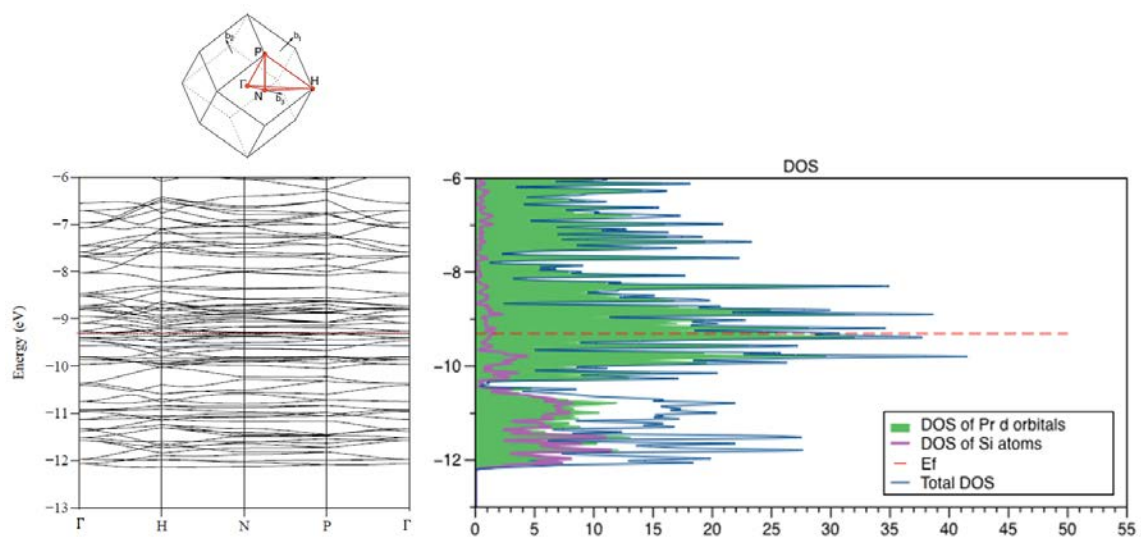


Figure 4.9(c). The band structure with the plot of DOS of Pr₃Si at the same energy range are presented. The red dashed line is Fermi level (-9.308356 eV.).

In the DOS calculation, 285 k-points were used throughout the irreducible edge of the Brillouin zone in order to provide a nice mesh. Those 285 k-points were obtained via programming in MATLAB⁶⁶ and evenly dividing the first Brillouin zone⁶⁷ (a tetrahedron, Γ -H-N-P). An explicit examination was done for checking the symmetry of 285 k-points in the direct space, as seen in Figure 4.10. The spatial coordinates of each k point need to be converted from the conventional lattice to the primitive lattice via applying a transfer matrix. The weighting values of each k-point are determined through the symmetry operation of the points group and the values are listed in Table 4.4. The band calculation and DOS of Pr₃Si were carried out on the program “YAeHMOP”³⁹. The valence ionization potentials (H_{ii} in ev)of different shells⁶⁴ and exponent (ξ)⁶⁵ are listed in Table 4.5.

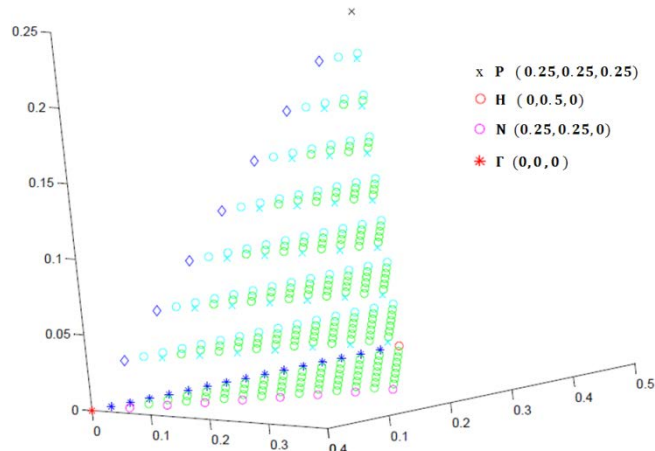


Figure 4.10. A mesh of 285 k-points throughout the first Brillouin zone (A tetrahedron, Γ -H-N-P)

Table 4.4. The weighting values of each K point in the first Brillouin zone of body center cubic.

K points	Coordinates	Weighting Value	Point Group (International notation)	Point Group	Calculation
Gamma	(0,0,0)	1	<i>m3m</i>	Oh	48/48=1
Σ	($\alpha, \alpha, 0$)	12	<i>mm2</i>	C_{2v}	48/4=12
N	(1/4,1/4,0)	6	<i>mmm</i>	D_{2h}	48/8=6
G	($\alpha, 1/2 - \alpha, 0$)	6	<i>mm2</i>	C_{2v}	48/8=6
H	(0,1/2,0)	1	<i>m3m</i>	Oh	48/48=1
Δ	(0, α , 0)	6	<i>4mm</i>	C_{4v}	48/8=6
Λ	(α, α, α)	8	<i>3m</i>	C_{3v}	48/6=8
D	(1/4,1/4, α)	12	<i>mm2</i>	C_{2v}	48/4=12
F	($\alpha, 1/2 - \alpha, \alpha$)	8	<i>3m</i>	C_{3v}	48/6=8
P	(1/4,1/4, 1/4)	24	<i>-43m</i>	Td	48/24=2

Table 4.5. Extended Hückel Exponents(ξ), valence shell ionization potential (H_{ii} in eV) and coefficients are listed.

Atom	Orbitals	H_{ii} (eV)	ξ_1^a	ξ_2^a	c_1^b	c_2^b
Si	<i>3s</i>	-17.3	1.383			
	<i>3p</i>	-9.2	1.383			
Pr	<i>6s</i>	-7.42	1.40			
	<i>6p</i>	-4.65	1.40			
	<i>5d</i>	-8.08	2.75	1.267	0.7187	0.4449

^a Slater-type orbital exponents. ^b Coefficients used in double- ξ exponent.

We wished to go in insight into the nature and relative importance of Pr-Pr and Pr-Si bonding in Pr_3Si , so we focussed our attention especially on the overlap population calculations.¹⁰⁰ As seen in Figure 4.11 COOP (Crystal Orbital Overlap Population) shows, the bottom of the s band is primarily metal-silicon bonding and the top is metal-silicon antibonding. Up to the Fermi level, the integral of the COOP curves is the total overlap population of the given electron count. In this compound, Pr-Si bonding is the most important contributor to the stability of this compound, though Pr-Pr contributions are also significant. The result of COOP responds to the order of bond lengths in the structure which indicates that Pr-Si bonds have shorter bond length than Pr-Pr bonds. The electron concentration considered “optimal” in that there remain some Pr-Pr and Pr-Si bonding levels above the Fermi level. The antibonding “crossover” is about 1 eV above the E_f for both kinds of bonds. Nevertheless, the extent of such bonding character is much less than that of the occupied levels.

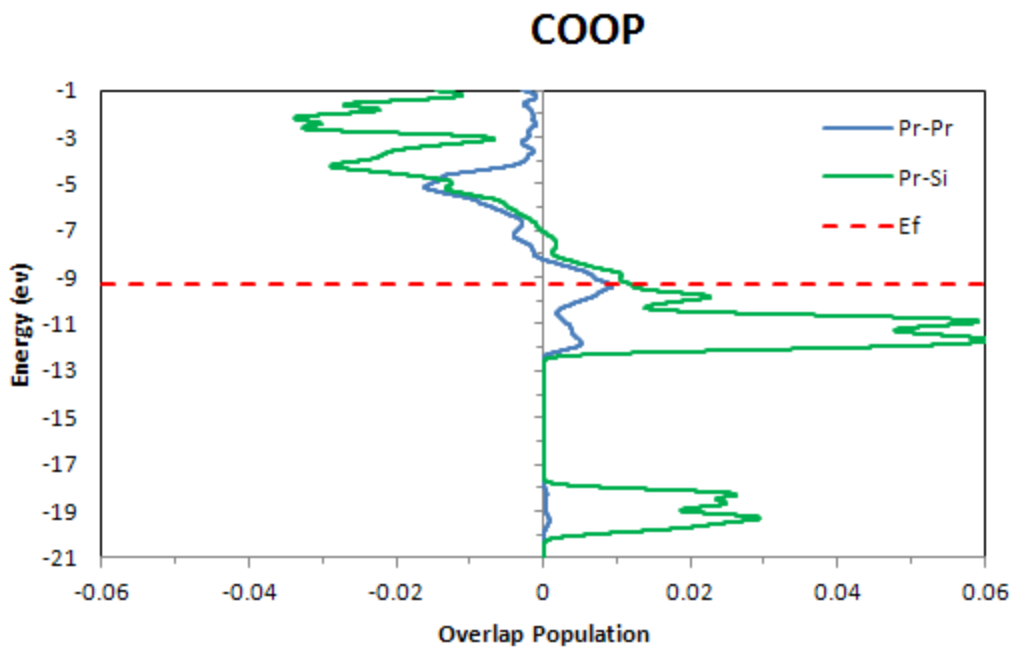


Figure 4.11. COOP (Crystal Orbital Overlap Population) of Pr_3Si . Positive population indicates bonding.

4.5 Result and Discussion

4.5.1 Compound III: Pr_3Si

The structure types and lattice parameters of ten known binary phases in Pr-Si system are listed in Table 4.6. Comparing to the new binary phase Pr_3Si , most of them belong to tetragonal and orthorhombic system, but Pr_3Si is classified to cubic system.

Table 4.6. Crystal structures and lattice parameters of intermediate phases in Pr-Si system.

Formula	Structures	Cell Constants (Å)	Type	Reference	Note
$\alpha\text{-Pr}_5\text{Si}_3$ ⁸⁷	Tetragonal <i>I4/mcm</i>	a=7.814 / 7.812(5) c=13.74 / 13.75(1)	Cr_5B_3	Journal of the Less Common Metals, 1972, 29, 25-31. / Acta Crystallographica, 1967, 22, 940-943	$T_c=330$ K (Gd_5Si_4)
Pr_5Si_4 ⁸⁸	Tetragonal <i>P4₁2₁2</i>	a=7.90 / 7.9092(0) c=14.91/ 14.9437(1)	Zr_5Si_4	Acta Crystallographica, 1967, 22, 940-943. / Journal of Alloys and Compounds (2002), 339(1-2), 189-194.	
$PrSi$ ⁸⁹	Orthorhombic <i>Pnma</i>	a=8.243(2) b=3.941(1) c=5.918(2)	FeB	Solid State Communications, 1977, 23, 821-823.	
$\alpha\text{-PrSi}_2$ ⁹⁰	Orthorhombic <i>Imma</i>	a= 4.23 b= 4.20 c= 13.68	$GdSi_2$	Journal of physical chemistry, 1959, 63, 2073-2074.	

Table 4.6. continued

Formula	Structures	Cell Constants (Å)	Type	Reference	Note
<u>β-PrSi₂</u> ⁹¹	Tetragonal <i>I4₁/amd</i>	a=4.165 c=13.766	ThSi ₂	Inorganic chemistry, 1968, 7, 1904-1908.	
PrSi _{1.96} ⁹³	Tetragonal <i>I4₁/amd</i>	a=4.205(5) c=13.73(2)	ThSi ₂	Journal of Physics: Condensed Matter (1991) 3, 3113-3124	
Pr ₂ Si ₃ ¹⁰¹	Tetragonal <i>Imma</i>	a=4.12 b=4.16 c=13.81	NdSi _{2-x}	Applied Surface Science (1989) 38, 156-161	
PrSi _{1.36} ⁹² (Pr ₂ Si _{3-x} , x=0.28)	Orthorhombic <i>Cmcm</i>	a=4.369(5) b=24.726(4) c=3.928(5)	PrSi _{1.36}	Journal of Magnetism and Magnetic Materials 1992, 114, (1-2), 131-7. Form Si ₆ Rings	d(Pr-Pr)= 3.78~4.38 Å d(Pr-Si)= 3.03~3.33 Å d(Si-Si)= 2.18~2.45 Å CN(Pr)= 6pr+7si CN(Si)= 3si+2pr
Pr ₃ Si ₂	Tetragonal <i>P4/mbm</i>	a=7.75(2) c=4.38(1)	Si ₂ U ₃	Inorganic Materials (1965) 1, (5) p648-p651	PDF unavailable
Pr ₂ Si _{3.6} ⁹⁴	Orthorhombic <i>Imma</i>	a=4.17 b=4.15 c=13.75	NdSi _{2-x}	Journal of Alloys and Compounds (1994) 204, 251-260	
Pr₃Si₁ (New)	Cubic <i>Ia-3d</i>	a=12.308(1)	Pr₃Si₁	Manuscript in preparation.	d(Pr-Pr)= 3.25~4.27 Å d(Pr-Si)= 2.93 Å CN(Pr)=7 CN(Si)=6

*Underline compounds are indicated in Pr-Si phase diagram.

4.5.2 Compound IV: Pr_2I_2Ge

The structure of Pr_2I_2Ge is isostructural with Y_2I_2Ge and Gd_2I_2Ge .¹⁰² They all have two-dimensional closed-packed bilayers which are constructed by RE_6 octahedra. The rare-earth metal layers are sandwiched by the layers of halogen atoms. Pr_2I_2Ge was synthesized at 1273 K for two weeks in a niobium tube. Y_2I_2Ge and Gd_2I_2Ge were synthesized at 1070 K in a Mo boat for 24 hours. According to the literature, it reported that Y_2I_2Ge and Gd_2I_2Ge display semiconductor behavior based on the result of the electrical resistivity measurements. The products of Pr_2I_2Ge are black crystals. However, it was failed to get highly pure sample to do electrical resistivity measurements. The space group of Pr_2I_2Ge is $R-3m$. The bond length of Pr-Ge is 3.0116 Å. Comparing to Gd_2I_2Ge , the Gd-Ge distance of 2.90 Å is shorter. The charge distribution of RE_2X_2Ge (RE=Rare earth, X=halides) can be expressed as $(RE^{+3})_2(X^{-1})_2(Ge^{-4})$ with no valence electrons left on the metal framework.

5. CONCLUSIONS

Four new compounds were synthesized in this work via solid state synthesis method (I $\text{Gd}_9\text{Br}_{16}\text{O}_4$, II. $\text{Gd}_6\text{Br}_7\text{Si}_2$, III. Pr_3Si , and IV. $\text{Pr}_2\text{I}_2\text{Ge}$). The first three compounds have new structures and compound IV is iso-structural with $\text{Gd}_2\text{I}_2\text{Ge}$ and $\text{Y}_2\text{I}_2\text{Ge}$.¹⁰² The electronic structures of compound I, II, and III were analyzed via theoretical density functional theory (DFT) calculations or extended Hückel/tight binding (EHTB) calculations. The results of EHTB band structure calculations indicate that the bottom the $\text{Gd}_9\text{Br}_{16}\text{O}_4$ d bands and those of a hypothetical analogous yttrium compound ($\text{Y}_9\text{Br}_{16}\text{O}_4$) are half filled; the Fermi levels of those two compounds cut through two d bands. $\text{Gd}_6\text{Br}_7\text{Si}_2$ and Pr_3Si are predicted to be metallic, as expected. The magnetic measurements on $\text{Gd}_9\text{Br}_{16}\text{O}_4$ and $\text{Gd}_6\text{Br}_7\text{Si}_2$ are done. The results show that $\text{Gd}_6\text{Br}_7\text{Si}_2$ has the property of soft magnets according to the plot of the hysteresis loop and it also appears two phase transitions at 27 K and 70 K based on the measurement of magnetic susceptibility vs temperature. The result of magnetic measurements on $\text{Gd}_9\text{Br}_{16}\text{O}_4$ is not reportable due to insufficient sample and the property of easily oxidized. All the compounds are highly air-sensitive and moisture-sensitive. Espousing those compounds in the air would cause them decomposed.

The measurements of energy-dispersive and wavelength-dispersive spectrometry systems (EDS and WDS) were applied to compound I and II to confirm the existence of the component elements. The crystal structures of fours compounds were obtained from a single-crystal X-ray data. Crystal twinning problems are common for compounds

synthesized via solid state synthesis and are required different process to collect or deal with the X-ray data. The Rietveld refinement is also applied to the X-ray powder patterns of compound II, III and IV in order to confirm the phase of each compound.

The structure of $Gd_9Br_{16}O_4$ is constructed by two different polyhedrons: tetrahedron (Gd_4O) and square antiprisms ($GdBr_8$). The tetrahedron (Gd_4O) connects to each other via edge sharing to form a chain and Br atoms connect those chains to build up a slab. Square antiprisms ($GdBr_8$) serve as pillars to connect the tetrahedral layers via point sharing. The building units of $Gd_6Br_7Si_2$ are Pr_3Si are RE_6 octahedrons. ($RE = Gd, Pr$) However, they perform different geometries. The structure of II. $Gd_6Br_7Si_2$ is a double-chains layer consisted of Gd_6Si and $Gd_6Si_{0.5}(Br)_{0.5}$ octahedra. II. Pr_2I_2Ge forms closed-packed bilayers and the metal layers are sandwiched by the layers of iodine atoms. The structure of III. Pr_3Si is very unique because the building units, octahedra Pr_6Si , build up an interpenetrating (10, 3)-a¹⁰³ type topology of network.

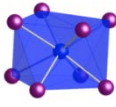
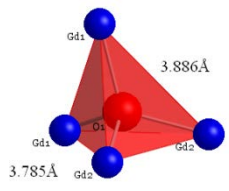
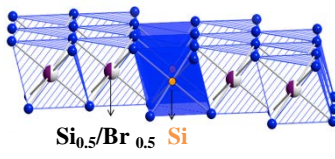
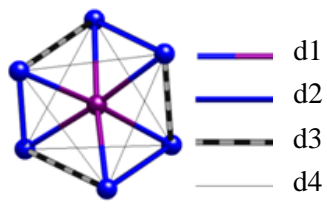
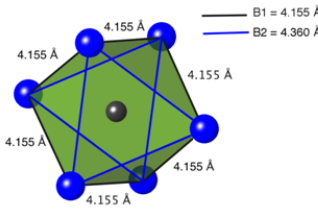
The comparisons of four crystal structures in this work are listed in Table 5.1. The common properties of those structures are that they all have interstitial atoms sitting in the center of polyhedra. There are three different types of polyhedra seen in four structures. They are square antiprisms, tetrahedra and octahedra. Those polyhedra become building units to construct the two dimensional or three dimensional structures via edge sharing or point sharing.

Table 5.1. The comparisons of four crystal structures in this work.

Formula	Crystal System Space Group	Cell Constants	Structure	Building Units
I. Gd ₉ Br ₁₆ O ₄	Orthorhombic <i>Fddd</i>	a=8.1902(4) b=20.9843(9) c=38.840(2) $\alpha=\beta=\gamma=90^\circ$	2-D Gd metal layer plus square antiprisms to form a 3-D structure	1. Square antiprisms: GdBr ₈ 2. Interstitial Tetrahedra: Gd ₄ O
II. Gd ₆ Br ₇ Si ₂	Monoclinic <i>C2/m</i>	a=21.415(5) b=4.123(1) c=10.907(3) $\beta=115.891(3)$	2-D Gd metal layer	1. Interstitial Octahedra: Gd ₆ Si or Gd ₆ Br
III. Pr ₃ Si	Cubic <i>Ia-3d</i>	a=12.328(1) $\alpha=\beta=\gamma=90^\circ$	3-D inter-penetrating octahedra (10,3)-a network	1. Interstitial Octahedra: Pr ₆ Si
IV. Pr ₂ I ₂ Ge	Trigonal <i>R-3m</i>	a=4.3603(5) c=32.063(5) $\alpha=\beta=90^\circ$ $\gamma=120^\circ$	2-D Pr metal layer	1. Interstitial Octahedra: Pr ₆ Ge

Because the common properties of those structures are the interstitial atoms of polyhedra, the comparisons of the bond lengths in different interstitial polyhedra are listed in Table 5.2. There is one interesting phenomenon is observed, after comparing the bond lengths of each polyhedron. The shorter metal-metal bonds are labeled with blue color in Table 5.2. Those shorter M-M bonds are all located at the edges which are sharing with the neighboring polyhedron to construct a chain or a layer. This characteristic is also observed in the chains built by M_6X_{12} and M_6X_8 cluster.^{19, 104} A reference from Yee and Hughbanks⁷² reported a picture of semilocalized bonding via calculating the bonding orbitals of a semiconductor (Y_2Cl_3), and a hypothetical interstitial compound ($Y_4Cl_6H_2^{+2}$) which provide us a clarification on the relationship between the structure-property and trends in interstitial chemistry. Although the question about where and whether, interstitial atoms will be bound is difficult to answer usually, viewing interstitial atoms as filled-shell donor and the RE_6 metal octahedron as an acceptor we can expect that orbital overlapping interaction between the donor and acceptor should be stronger for extended systems. In other words, the interstitial atoms may stabilize the structure.

Table 5.2. The comparisons of bond lengths in different interstitial polyhedra.

Formula	Building Units	Bond Length between metal and interstitial atom (Å)	Bond Length between metal and metal (Å)
I. $Gd_9Br_{16}O_4$	$GdBr_8$ 	$d(Gd-Br)=2.943$	None
	Gd_4O 	$d(Gd1-O1)=2.251$ $d(Gd1-O1)=2.263$ $d(Gd2-O2)=2.237$ $d(Gd2-O2)=2.258$	$d(Gd1-Gd1)=3.465$ $d1(Gd1-Gd2)=3.886$ $d2(Gd1-Gd2)=3.785$ $d(Gd2-Gd2)=3.950$
II. $Gd_6Br_7Si_2$	Gd_6Si and $Gd_6Si_{0.5}(Br)_{0.5}$ 	$d(Gd-Si)=2.881$ $d(Gd-Br_{0.5}/Si_{0.5})=2.879$ $d(Gd-Br)=2.97$	$d(Gd-Gd)=4.026$ $d(Gd-Gd)=4.121$
III. Pr_3Si	Pr_6Si 	$d1(Pr-Si)=2.9301$	$d2(Pr-Pr)=3.907$ $d3(Pr-Pr)=4.140$ $d4(Pr-Pr)=4.243$
IV. Pr_2I_2Ge	Pr_6Ge 	$d(Pr-Ge)=3.0110$	$d(Pr-Pr)=4.155$ $d(Pr-Pr)=4.360$

The first examples of reduced rare earth halides containing second-row non-metal interstitial atoms were known as $\text{Gd}_4\text{I}_5\text{Si}$ and $\text{Gd}_3\text{I}_3\text{Si}$ ²² which have iso-structures with $\text{Y}_4\text{I}_5\text{C}$ ²³ and $\text{Gd}_3\text{Cl}_3\text{C}$ ²⁴. Their structures are built by edge-sharing Gd_6 octahedra with centered silicon to form one-dimensional chains and a three-dimensional network. Similarly, $\text{Gd}_4\text{Br}_6\text{Si}$ ²⁵ has chains structure and is isotopic with Tb_4SiBr_6 , Gd_4CBr_6 and Sc_4CCl_6 ²⁶⁻²⁷. Although a lot of metal rich halides MX_nA ($n \leq 2$, $\text{A} = \text{H}, \text{C}, \text{N}, \text{O}$, $\text{X} = \text{Halogen}$) have been published.²⁷⁻²⁹ However, compound I. $\text{Gd}_9\text{Br}_{16}\text{O}_4$, II. $\text{Gd}_6\text{Br}_7\text{Si}_2$, and III. Pr_3Si , still have unknown new structures and show interesting magnetic or electric properties according to the magnetic measurements and band structure calculations. If the challenges of synthesizing high yield and high purity can be broken through, the potential applications of lanthanide-metal-halides compounds will be optimistic.

REFERENCES

1. J. J. Croat, J. F. Herbst, R. W. Lee and F. E. Pinkerton, *Appl. Phys. Lett.*, 1984, 44, 148-149.
2. V. Provenzano, A. J. Shapiro and R. D. Shull, *Nature*, 2004, 429, 853-857.
3. V. K. Pecharsky and K. A. Gschneidner, Jr., *Phys. Rev. Lett.*, 1997, 78, 4494-4497.
4. M. Guloy Arnold, R. Ramlau, Z. Tang, W. Schnelle, M. Baitinger and Y. Grin, *Nature*, 2006, 443, 320-323.
5. G. J. Miller, *Chem. Soc. Rev.*, 2006, 35, 799-813.
6. D. Haskel, Y. B. Lee, B. N. Harmon, Z. Islam, J. C. Lang, G. Srajer, Y. Mudryk, K. A. Gschneidner, Jr. and V. K. Pecharsky, *Phys. Rev. Lett.*, 2007, 98, 247205/247201-247205/247204.
7. W. E. Wallace, *Prog. Solid State Chem.*, 1985, 16, 127-162.
8. R. J. Elliot, *Magnetic Properties of Rare Earth Metals*, Plenum, New York, 1972.
9. L. E. Roy and T. Hughbanks, *Journal of the American Chemical Society*, 2006, 128, 568-575.
10. G. Meyer, *Chem. Rev.*, 1988, 88, 93-107.
11. H. Mattausch, O. Oeckler, C. Hoch and A. Simon, *Z. Anorg. Allg. Chem.*, 2006, 632, 1233-1238.
12. A. Simon, *Journal of Solid State Chemistry*, 1985, 57, 2-16.
13. H. Mattausch, O. Oeckler and A. Simon, *Inorg. Chim. Acta*, 1999, 289, 174-190.
14. H. Mattausch, O. Oeckler and A. Simon, *Z. Anorg. Allg. Chem.*, 2008, 634, 503-506.
15. H. Mattausch, M. C. Schaloske, C. Hoch and A. Simon, *Z. Anorg. Allg. Chem.*, 2008, 634, 498-502.

16. H. Mattausch, M. C. Schaloske, C. Hoch, C. Zheng and A. Simon, *Z. Anorg. Allg. Chem.*, 2008, 634, 491-497.
17. H. Mattausch, O. Oeckler and A. Simon, *Z. Kristallogr. New Cryst. Struct.*, 2003, 218, 282.
18. H. Mattausch and A. Simon, *Z. Kristallogr. New Cryst. Struct.*, 2005, 220, 313.
19. S. M. Kauzlarich, T. Hughbanks, J. D. Corbett, P. Klavins and R. N. Shelton, *Inorganic Chemistry.*, 1988, 27, 1791-1797.
20. A. S. Hj.Mattausch, *Z. Kristallogr. New Cryst. Struct.*, 1997, 212, 99.
21. M. Ryazanov, H. Mattausch and A. Simon, *Journal of Solid State Chemistry*, 2007, 180, 1372-1380.
22. C. J. Zimm, A.; Sternberg, A.; Pecharsky, V. K.; Gschneidner, K. A. Jr; and M. a. A. Osborne, I., *Adv. Cryog. Eng.*, 1998, 1759–1766.
23. D. Paudyal, V. K. Pecharsky, K. A. Gschneidner and B. N. Harmon, *Phys. Rev. B: Condens. Matter Mater. Phys.*, 2006, 73, 144406/144401-144406/144412.
24. A. R. West, *Basic Solid State Chemistry*, Wiley, New York, 1999.
25. J. Daintith, *Oxford Dictionary of Chemistry*, Oxford, New York, 2008.
26. R. Merkle and J. Maier, *Zeitschrift für anorganische und allgemeine Chemie*, 2005, 631, 1163-1166.
27. M. McElfresh, *Quantum Design*, 1994, 1-38.
28. R. N. Guillemette, *Electron Microprobe Techniques*, 2008, 5, 335-365.
29. I. N. Levine, *Quantum Chemistry*, Prentice-Hall, New Jersey, 1991.
30. M. Wolfsberg and L. Helmholz, *The Journal of Chemical Physics*, 1952, 20, 837-843.
31. R. Hoffmann, *The Journal of Chemical Physics*, 1963, 39, 1397-1412.
32. R. Hoffmann, *The Journal of Chemical Physics*, 1964, 40, 2474-2480.
33. R. Hoffmann, *The Journal of Chemical Physics*, 1964, 40, 2480-2488.

34. R. Hoffmann, *The Journal of Chemical Physics*, 1964, 40, 2745-2745.
35. E. Hückel, *Z. Phys.*, 1931, 70, 204.
36. J. A. Berson, *Angew. Chem., Int. Ed.*, 1996, 35, 2750.
37. J. C. Slater, *Physical Review*, 1930, 35, 210.
38. W. L. J. Ren, and M.-H. Whangbo, *CAESAR*, Prime Color Software, North Carolina, 1998.
39. G. Landrum. and W. Glassey, *YAEHMOP*, University of Cornell, Ithaca, 2001.
40. P. Hohenberg and W. Kohn, *Physical Review*, 1964, 136, B864-B871.
41. W. Kohn and L. J. Sham, *Physical Review*, 1965, 140, A1133-A1138.
42. R. G. Parr, *Quantum Theory of Molecular Electronic Structure*, Benjamin, New York, 1963.
43. W. Yang, *Density-Functional Theory of Atoms and Molecules*, Oxford, New York, 1989.
44. C. J. Cramer, *Essentials of Computational Chemistry: Theories and Models*, Wiley, New York, 2004.
45. G. Meyer, S. Doetsch and T. Staffel, *Journal of the Less-Common Metals*, 1987, 127, 155-160.
46. G. Meyer and T. Staffel, *Zeitschrift für anorganische und allgemeine Chemie*, 1986, 532, 31-36.
47. G. M. Sheldrick, *SADABS*, Bruker AXS, Madison, 2001.
48. G. M. Sheldrick, *SHELXTL*, Bruker AXS, Madison, 2000.
49. R. N. Guillemette, *Methods of Soil Analysis. Part 5: Mineralogical Methods*, Soil Science Society of America, Madison, 2008.
50. G. S. Smith, A. G. Tharp and Q. Johnson, *Nature*, 1966, 210, 1148-1149.
51. O. Kahn, *Molecular Magnetism*, VCH, New York, 1993.
52. R. L. Carlin, *Magnetochemistry*, Springer, New York, 1985.

53. D. Rubio Temprano, J. Rodríguez Fernández, J. C. Gómez Sal, A. Hernando and J. M. Rojo, *J. Magn. Magn. Mater.*, 1999, 196–197, 770-772.
54. J. C. M. van Dongen, T. T. M. Palstra, A. F. J. Morgownik, J. A. Mydosh, B. M. Geerken and K. H. J. Buschow, *Physical Review B*, 1983, 27, 1887-1902.
55. B. Coqblin, *The Electronic Structure of Rare Earth Metals and Alloys*, Academic, New York, 1977.
56. S. Blundell, *Magnetism in Condensed Matter*, Oxford, New York, 2001.
57. A. Simon, *Chem. Unserer Zeit*, 1976, 10, 1-9.
58. H. Mattausch, R. K. Kremer, R. Eger and A. Simon, *Z. Anorg. Allg. Chem.*, 1992, 609, 7-11.
59. A. D. Becke, *Physical Review A*, 1988, 38, 3098-3100.
60. C. Lee, W. Yang and R. G. Parr, *Physical Review B*, 1988, 37, 785-789.
61. B. Delley, *The Journal of Chemical Physics*, 2000, 113, 7756-7764.
62. B. Delley, *The Journal of Chemical Physics*, 1990, 92, 508-517.
63. B. Delley, *International Journal of Quantum Chemistry*, 1998, 69, 423-433.
64. Y. Tian and T. Hughbanks, *Inorganic Chemistry*, 1993, 32, 400-405.
65. L. E. Roy and T. Hughbanks, *The Journal of Physical Chemistry B*, 2006, 110, 20290-20296.
66. S. Nakamura, *Numerical Analysis and Graphic Visualization with MATLAB*, Prentice Hall, New Jersey, 1996.
67. M. Tinkham, *Group Theory and Quantum Mechanics*, Dover, New York, 2003.
68. W. Setyawan and S. Curtarolo, *Computational Materials Science*, 2010, 49, 299-312.
69. M. Lax, *Symmetry Principles in Solid State and Molecular Physics*, Dover, New York, 2001.
70. Th. Hahn, *International Tables for Crystallography*, Wiley online library, 2006.

71. D. W. Bullett, *Inorganic Chemistry*, 1985, 24, 3319-3323.
72. K. A. Yee and T. Hughbanks, *Inorganic Chemistry*, 1992, 31, 1620-1625.
73. G. S. Ebbinghaus, and A. Griffith, *Z. Naturforsch.*, 1982, A37, 564.
74. R. K. Kremer, H. J. Mattausch, A. Simon, S. Steuernagel and M. E. Smith, *Journal of Solid State Chemistry*, 1992, 96, 237-242.
75. L. Roy and T. Hughbanks, *Journal of Solid State Chemistry*, 2003, 176, 294-305.
76. K. Takahashi, A. Yoshikawa and A. Sandhu, *Wide Bandgap Semiconductors: Fundamental Properties and Modern Photonic and Electronic Devices*, Springer, New York, 2007.
77. D. Nagaki, A. Simon and H. Borrmann, *Journal of the Less-Common Metals*, 1989, 156, 193-205.
78. S. J. Hwu and J. D. Corbett, *J. Solid State Chem.*, 1986, 64, 331-346.
79. H. Mattausch, A. Simon, G. J. Miller, W. Bauhofer, and R. K. Kremer, *Handbook on the Physics and Chemistry of Rare Earth*, Elsevier, Amsterdam, 1991.
80. H. Mattausch and A. Simon, *Angew. Chem., Int. Ed.*, 1998, 37, 499-502.
81. J. D. Corbett, *Inorganic Syntheses*, Wiley, New York, 1983.
82. G. M. Sheldrick, *TWINABS*, Bruker AXS, University of Göttingen, 2008.
83. G. M. Sheldrick, *CELL_NOW*, Bruker AXS, University of Göttingen, 2008.
84. J. Tanski. and T. Shalumova, *Treating Non-Merohedrally Twinned Crystal Data*, Bruker AXS, Madison, 2008.
85. V. N. Eremenko, K.A. Meleshevich, and Yu. I. Buyanov, *Izv. VUZ Tsvetn. Metall.*, 1986, 3, 82.
86. E. Houssay, A. Rouault, O. Thomas, R. Madar and J. P. Senateur, *Applied Surface Science*, 1989, 38, 156-161.
87. I. Mayer and I. Felner, *Journal of the Less Common Metals*, 1972, 29, 25-31.

88. G. S. Smith, A. G. Tharp and W. Johnson, *Acta Crystallographica*, 1967, 22, 940-943.
89. V. N. Nguyen, F. Tch  ou and J. Rossat-Mignod, *Solid State Communications*, 1977, 23, 821-823.
90. J. A. Perri, E. Banks and B. Post, *Journal of Physical Chemistry*, 1959, 63, 2073-2074.
91. I. Mayer, and Y. Eshdat, *Inorganic Chemistry*, 1968, 7, 1904-1908.
92. P. Schobinger-Papamantellos, K. H. J. Buschow and P. Fischer, *J. Magn. Magn. Mater.*, 1992, 114, 131-137.
93. B. Lambert-Andron, F. Sayetat, S. Auffret, J. Pierre and R. Madar, *Journal of Physics: Condensed Matter*, 1991, 3, 3113.
94. N. Boutarck, J. Pierre, B. Lambert-Andron, P. L'Heritier and R. Madar, *J. Alloys Compd.*, 1994, 204, 251-260.
95. J. Evers, G. Oehlinger, K. Polborn and B. Sendlinger, *Journal of Solid State Chemistry*, 1993, 103, 45-56.
96. J. Evers, G. Oehlinger, K. Polborn and B. Sendlinger, *Journal of Solid State Chemistry*, 1991, 91, 250-263.
97. J. Evers, *Journal of Solid State Chemistry*, 1978, 24, 199-207.
98. A. F. Wells, *Three-Dimensional Nets and Polyhedra*, Wiley, New York, 1977.
99. B. Gil-Hernandez, P. Gili, J. K. Vieth, C. Janiak and J. Sanchiz, *Inorganic Chemistry*, 49, 7478-7490.
100. J. Y. Saillard and R. Hoffmann, *Journal of the American Chemical Society*, 1984, 106, 2006-2026.
101. A. R. E. Houssay, O. Thomas, R. Madar and J. P. Senateur, *Appl. Surf. Sci.*, 1989, 38, 156-161.
102. M. y. Lukachuk, R. Lukachuk, H. Kremer, A. Mattausch and A. Simon, *Inorganic Chemistry*, 2007, 46, 3231-3235.
103. H. Yang, T.-h. Li, F. Wang and J. Zhang, *Inorganic Chemistry Communications*, 2012, 16, 86-88.

104. D. A. Lokken and J. D. Corbett, *Journal of the American Chemical Society*, 1970, 92, 1799-1800.

APPENDIX

Appendix A-1. Extended Hückel Exponents (ξ), valence shell ionization potential (H_{ii} in eV) and coefficients are listed.

<i>Atom</i>	<i>Orbitals</i>	H_{ii} (eV)	ξ_1^a	ξ_2^a	c_1^b	c_2^b
O	2s	-32.3	2.750			
	2p	-14.8	2.750			
Si	3s	-17.3	1.383			
	3p	-9.2	1.383			
Br	4s	-28.0	2.64			
	4p	-13.9	2.26			
Y	5s	-7.02	1.74			
	5p	-4.40	1.70			
	4d	-6.8	1.40	3.60	0.8316	0.3041
Pr	6s	-7.42	1.40			
	6p	-4.65	1.40			
	5d	-8.08	2.75	1.267	0.7187	0.4449
“Gd ⁺ ” ^c	6s	-7.12	1.74			
	6p	-4.40	1.70			
	5d	-7.03884	1.40	3.60	0.8316	0.3041
“Gd ⁻ ” ^c	6s	-6.91	1.74			
	6p	-4.40	1.70			
	5d	-6.56116	1.40	3.60	0.8316	0.3041

^a Slater-type orbital exponents. ^b Coefficients used in double- ξ exponent. Gd⁺ and Gd⁻ are used to model the spin-dependent energies of valence *s* and *d* electrons of Gd centers which have the spins that are aligned parallel and antiparallel respecting to the local spin direction of 4*f* electrons.